



**UNIVERSITÀ DEGLI STUDI DI PADOVA**  
**DIPARTIMENTO DI SCIENZE CHIMICHE**  
**CORSO DI LAUREA MAGISTRALE IN SCIENZA DEI MATERIALI**

**TESI DI LAUREA MAGISTRALE**

Fabrication and characterization of FET devices for the study of the electrical properties of MoS<sub>2</sub> films deposited via ALD

Relatore: Prof. Enrico Napolitani

Correlatori: Dr. Enrico Di Russo, Dr. Alessandro Tonon

Controrelatore: Prof.ssa Elisabetta Collini

Laureando:  
Daniele Demeneghi  
2085642

ANNO ACCADEMICO 2023/2024



# ABSTRACT

Interest in TMDs (e.g., MoS<sub>2</sub>, WS<sub>2</sub>, MoSe<sub>2</sub>, WSe<sub>2</sub>) has been steadily growing over the past decade due to their outstanding physical, electronic, optical, and chemical properties, that could pave the way for new applications. Specifically, the possibility to grow large area 2D crystals of TMDs with direct bandgap suggest their application in photonics and nano-electronics. The medium-long term goals are to employ TMDs in the fabrication of ultra-scaled CMOS transistors, photodetectors, and emitting devices with yields comparable to that of OLED lighting that make up modern screens. In addition, the structural properties of TMDs make them suitable to develop a new generation of flexible and transparent “wearable” electronic devices and might also advance research in the biomedical field (nano-toxicology, bio-analysis, antibacterial and wound healing, bio-imaging, drug delivery and cancer therapy) due to the large exposure surface, versatile surface chemistry and good biocompatibility.

However, several challenges need to be addressed for TMD implementation in technology, such as to obtain their synthesis with good electronic properties on a wafer scale, to find processes to tune their properties (e.g., doping) and, of key relevance, to develop technological processes to integrate these materials into novel electronic devices. This includes finding a suitable device fabrication technique and reducing the high contact resistance between the metal and the TMD. In particular, much research has been devoted to fabricating test devices with single crystal MoS<sub>2</sub> using Electron Beam Lithography (EBL). This approach is useful for research goals, however it is not scalable due to low throughput, so it is not possible to employ it on an industrial scale. Instead, it is necessary to fabricate devices with a technique that allows large scale production of devices with large area TMD films. In this regard, a higher throughput can be achieved via photolithography, that is the standard industry technique used to fabricate semiconductor devices.

The principal aim of this thesis is to study the photolithography processes necessary to fabricate Field Effect Transistors (FET) by depositing patterned Au/Ti contacts on MoS<sub>2</sub> samples grown via Atomic Layer Deposition (ALD) supplied by CEA-LETI. Finally, an exploratory study was conducted regarding the use of Pulsed Laser Annealing (PLA) on the contact, to improve the quality of the Ti/MoS<sub>2</sub> interface and therefore the contact resistance.

Indeed, PLA induces an ultra-rapid and localized thermal treatment thanks to the use of a KrF excimer laser with a wavelength of 248 nm and a pulse duration of 22 ns.

To assess the quality of the MoS<sub>2</sub> after each photolithography step Raman spectroscopy was employed along with images taken with Optical Microscopy allowing to adjust the relevant parameters of each fabrication step. Then, FET devices were fabricated, and the transistor transfer curves were measured to obtain information regarding the mobility of the material, however no relevant current was observed. Following this attempt, PLA was used on a continuous film of Ti/MoS<sub>2</sub>. Atomic Force Microscopy (AFM) was used to examine the morphology of Ti and determine the PLA conditions that leave the Ti over the MoS<sub>2</sub> unaltered and Raman spectroscopy allowed to obtain information on the chemistry of the interface between Ti and MoS<sub>2</sub>, namely the presence of a Ti<sub>x</sub>S<sub>y</sub> compound. Finally, to verify the feasibility of PLA patterned metal electrodes of Ti on MoS<sub>2</sub> were laser processed. This led to the ablation of the Ti contacts which was explained with the damage of the MoS<sub>2</sub> introduced during the metal sputtering phase.

In summary, this thesis work focus was the study of the fundamental steps involved in the fabrication of FET devices. The aim has been to address critical issues reported in the literature, such as avoiding film delamination during lithography phase and improving the device performances by optimizing the contact deposition. Photolithography parameters optimization allowed to reach good reproducibility in device fabrication. PLA was applied to MoS<sub>2</sub> film highlighting an ED window in which no modification occurs. This result opens up the possibility to process Ti/MoS<sub>2</sub> contacts to decrease the contact resistance without damaging the semiconductor film. .

The research activity of this thesis has been done in the framework of the European Union's Horizon 2020 project ASCENT+ GA No 871130 and the University of Padova grant UNIPD-ISR 2017 'SENSITISE' and within international collaborations with CEA-LETI (France) and Tyndall National Institute - University College Cork (Ireland). The starting samples were provided by CEA-LETI. I personally executed all the experimental steps, from the photolithographic processes to the electrical characterization of the fabricated devices with the exception of the metal sputtering step.

## Summary

CHAPTER 1: STATE OF THE ART .....	1
1.1 A SHORT OVERVIEW OF 2D MATERIALS .....	1
1.2 TRANSITION METAL DICHALCOGENIDES .....	3
1.1.1 Overview of TMD properties and applications .....	4
1.1.2 MoS <sub>2</sub> structure and Raman spectra .....	9
1.3 TMD SYNTHESIS TECHNIQUE .....	14
1.3.1 Mechanical exfoliation .....	15
1.3.1 Chemical vapor deposition.....	15
1.3.3 Radio frequency magnetron sputtering-based techniques .....	19
1.4 FIELD EFFECT TRANSISTOR (FET).....	20
1.4.1 FET working principles and model.....	20
1.4.2 Limitations of modern devices and rationale for TMD based FETs .....	22
1.4.3 Mobility.....	24
1.4.4 Doping.....	26
1.4.5 FET fabrication technique.....	27
CHAPTER 2: EXPERIMENTAL .....	30
WORKPLAN .....	30
RESIST SPIN COATING .....	32
OPTICAL LITHOGRAPHY .....	33
METAL SPUTTERING .....	34
LASER PROCESSING .....	37
RAMAN SPECTROSCOPY .....	38
AFM .....	39
ELECTRICAL CHARACTERIZATION.....	41
CHAPTER 3: RESULTS .....	44
3.1 INTRODUCTION.....	44
3.2 FET DESIGN .....	44

3.4 STUDY OF THE PHOTOLITHOGRAPHY PROCESS .....	45
3.4.1 Substrate preparation .....	45
3.4.2 Overview of the main photolithography steps.....	47
3.4.3 LOR baking and liftoff temperature optimization .....	50
3.4.4 Dose and developing time optimization .....	52
3.5 FET FABRICATION AND ELECTRICAL MEASUREMENTS .....	55
3.5.1 FET fabrication.....	55
3.5.2 Electrical measurements .....	56
3.6 LASER AND THERMAL PROCESSING OF Ti/MoS <sub>2</sub> CONTACT.....	60
3.6.1 MoS <sub>2</sub> film stability to PLA .....	60
3.6.2 Laser processing of the contacts .....	68
3.6.2 Laser processing of the pads .....	71
CHAPTER 4: CONCLUSIONS AND PERSPECTIVES .....	74
BIBLIOGRAPHY .....	76



# CHAPTER 1: STATE OF THE ART

## 1.1 A SHORT OVERVIEW OF 2D MATERIALS

Interest in 2D materials has grown exponentially over the past decade beginning with the discovery of graphene to the development of materials such as hexagonal boron nitride (h-BN) and transition metal dichalcogenides (TMDs).

The milestones in the study of the properties of 2D materials and their applications in devices are highlighted in Fig.1.1 The event that sparked research into 2D materials occurred in 2004, when Novoselov and Geim prepared via mechanical exfoliation various 2D crystals, including graphite, BN, and several TMDs [Novoselov et al., 2005]. They produced single-layer samples, observing their 2D structure by using transmission electron microscopy (TEM). Thanks to this work they obtained the Nobel Prize in Physics in 2010. In 2005, Geim and Kim independently discovered the band structure of graphene, a zero-bandgap semiconductor. This discovery reignited interest in 2D materials, including TMDs, graphitic carbon nitrides (g-C<sub>3</sub>N<sub>4</sub>), hexagonal boron nitride (h-BN), black phosphorus (BP), MXenes, and silicene. The remarkable physical, electronic, optical, and chemical properties of 2D materials, along with their potential for new applications, have captivated researchers across various fields, including condensed matter physics, materials science, chemistry, and nanotechnology. The confinement of electrons in two dimensions imparts unique electronic properties to 2D materials, due to their highly anisotropic electronic structure. Moreover, the large specific surface area of 2D materials makes them suitable for applications like catalysis and chemical detection. Their atomic thickness contributes to excellent mechanical flexibility and optical transparency, presenting significant opportunities for developing wearable optoelectronic devices.

In 2010, TMDs experienced a resurgence of interest following the discovery that a single MoS<sub>2</sub> flake exhibits a direct bandgap at room temperature when its thickness is reduced to a monolayer [Splendiani et al., 2010]. The potential of using a single layer MoS<sub>2</sub> flake to create field-effect transistors (FETs) was demonstrated for the first time in 2011 [Radisavljevic et al., 2011]. The following year saw the development of the first photodetector based on MoS<sub>2</sub>. It was also noted that the material's light absorption spectrum could shift



from red to green by adjusting the number of MoS<sub>2</sub> layers, a unique property not observed in any other material at the time. In 2015, graphene was incorporated into a solar cell for the first time. Six years later, in 2021, a flexible solar cell (6 μm thick) entirely based on a graphene/WSe<sub>2</sub> heterostructure was developed, achieving an efficiency of 5.1% [Nazif et al., 2021].

Another breakthrough occurred in 2015 when single-photon emission was first observed in WSe<sub>2</sub> flakes. This phenomenon was attributed to structural defects and stress homogeneities, which serve as trapping sites for excitons [Tonndorf et al., 2015]. This discovery opened up numerous possibilities for applications in quantum optics technologies, a key area of strategic research for the coming years.

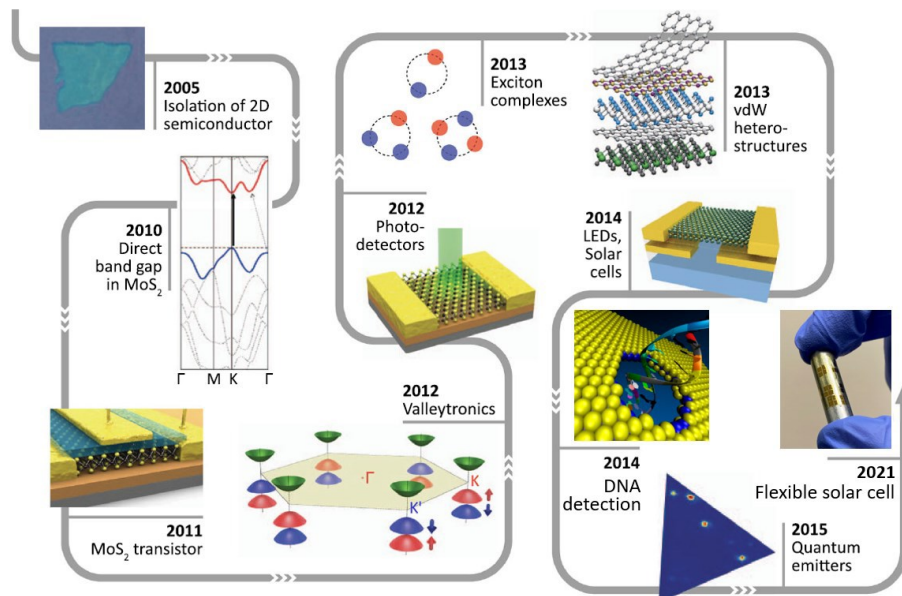


Figure 1.1: Key milestones in 2D materials research and main advancements in the development of optoelectronic devices.

In the medium to long term, a key goal is to develop emitting devices with efficiencies comparable to those of modern OLED lighting used in screens [Withers et al., 2015]. Additionally, 2D materials hold promise for advancing flexible and transparent electronics, paving the way for future wearable devices [Pang et al., 2020]. These materials could also drive significant progress in the biomedical field, including nano-toxicology, bio-analysis, antibacterial applications, wound healing, bio-imaging, drug delivery, and cancer therapy, thanks to their large surface area, versatile surface chemistry, and excellent biocompatibility [Rohaizad et al., 2021; Wang et al., 2020]. Over the next decade, the benefits of 2D materials are expected to greatly impact the microelectronics industry. They can be seamlessly integrated into silicon-based systems for various applications such as image sensors,

LiDAR, data communications, lasers, piezoelectric devices, NEMS, RF devices, and magnetic devices, potentially extending Moore's Law through further miniaturization.

However, integrating 2D materials into mass-production devices presents several challenges. Achieving large-scale production of high-quality, structurally controlled materials on appropriate substrates remains difficult, with graphene being a notable exception. Precise control over their composition, layer count, lateral dimensions, crystal phases, doping, defects, deformations, vacancies, and surface properties is crucial for tuning their optical and electronic characteristics. Ongoing research in areas like epitaxy, nano-characterization, prototype device fabrication, and theoretical modeling is focused on addressing these fundamental issues to enable the integration and commercialization of 2D materials in everyday electronic devices.

## 1.2 TRANSITION METAL DICALCOGENIDES

As previously mentioned, graphene—a two-dimensional sheet of  $sp^2$ -hybridized carbon—was the first 2D material to be extensively studied (Fig. 1.2). Its remarkable properties have sparked a surge of interest over the past decade. This is driven by its potential integration into a wide range of devices, including high-speed and radio-frequency logic devices, thermally and electrically conductive reinforced composites, sensors, and transparent electrodes for displays and solar cells. Specifically, graphene exhibits an ambipolar field effect, a quantum Hall effect at room temperature, and exceptionally high carrier mobility ( $10^4 - 10^5 \text{ cm}^2/\text{Vs}$ ) [Allen et al., 2010]. However, the lack of a bandgap in graphene makes it unsuitable for the development of logic circuits. It follows that fabrication of electronic devices such as field-effect transistors (FETs), photodetectors, and memory devices requires a different class of 2D materials. Among the most promising candidates are TMDs.

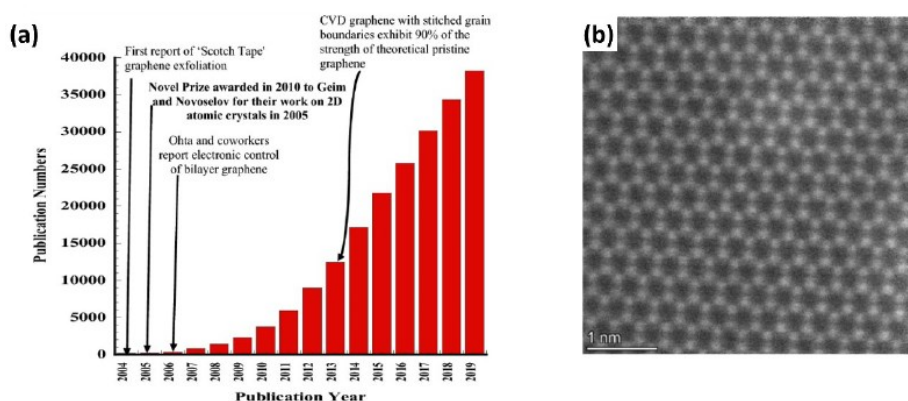
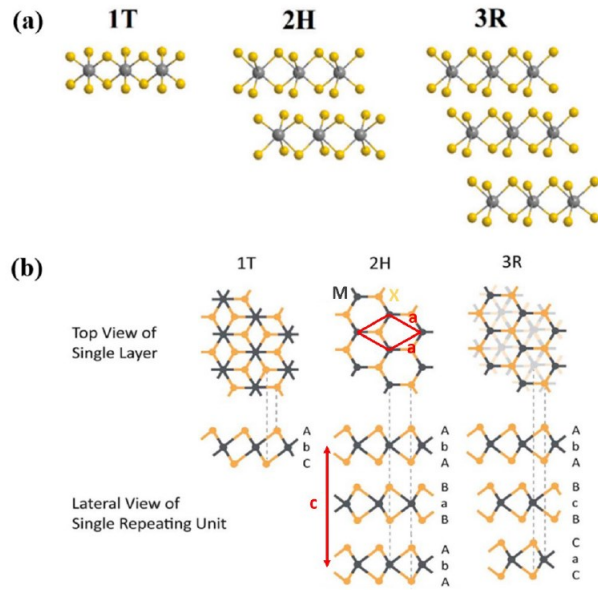


Figure 1.2: (a) A brief timeline of graphene research following its discovery in 2004, illustrating the surge in graphene-related academic publications [Saha et al., 2021]. (b) HAADF-STEM micrograph showing a single-layer graphene sheet, captured using a probe-corrected TEM at 60 kV. Courtesy: Enrico Di Russo.

### 1.1.1 Overview of TMD properties and applications

Two-dimensional transition metal dichalcogenides (TMDs) represent a rapidly emerging class of ultrathin layered materials with properties that vary based on their phases, composition, and layer count. A basic monolayer of a TMD consists of  $\text{MX}_2$  units, where M is a transition metal and X is a chalcogen atom. In this structure, the M atoms form a hexagonal lattice plane, which is sandwiched between two similarly packed chalcogen layers. While covalent bonds hold together the atoms within a single monolayer, the layers themselves interact via weak van der Waals forces [Vazirisereshk et al., 2019].

Three main polytypes are typically observed, depending on the stacking order and the coordination of X atoms relative to the central M atoms: 1T, 2H, and 3R, as illustrated in Fig. 1.3. The number 1, 2 or 3 reflects to the number of layers in a unit cell, while the letter denotes the crystallographic structure—trigonal (T), hexagonal (H), or rhombohedral (R). The two most commonly occurring polytypes in nature are 2H and 3R, which differ in their stacking structure: the 3R polytype has a non-centrosymmetric point group  $C_{3v}$  for all layer counts, whereas the 2H polytype exhibits the  $D_{3h}$  ( $D_{3d}$ ) point group for odd (even) layer counts [Samadi et al., 2018]. The 2H polytype, characterized by its hexagonal lattice and two molecules per unit cell with an AbA|BaB stacking order, is the most prevalent and particularly significant for electronic device fabrication due to its semiconducting properties [Samadi et al., 2018]. In a monolayer structure, the 2H polytype is typically referred to as 1H.



*Figure 1.3: The three primary polytypes of TMD materials, including their distinct stacking orders and structural parameters [Hoang et al., 2021].*

Another common crystalline phase is the 1T polytype, characterized by its octahedral coordination symmetry. In this phase, the sulfur layers are shifted, resulting in an AbC stacking sequence [Voiry et al., 2015]. However, the 1T phase of group-VI TMDs is generally unstable, leading to the formation of a superlattice structure to enhance material stability [Voiry et al., 2015]. Compared to the thermodynamically stable 2H polytype, most 1T-TMDs exhibit metallic or semi-metallic behavior, with only a few, such as  $\text{MoTe}_2$  and  $\text{WTe}_2$ , possessing stable distorted 1T phases [Lai et al., 2021].

The phase transition between different polytypes can be understood in terms of the rearrangement of electronic orbitals [Wang et al., 2018]. Fig. 1.4 illustrates the change in the molecular orbital structure of  $\text{MoS}_2$  during the transition from a trigonal prismatic to an octahedral structure. When the low-energy orbitals are fully occupied, the material demonstrates semiconducting properties, as seen in 1H- $\text{MoS}_2$ . In contrast, if the orbitals associated with 1T- $\text{MoS}_2$  are partially filled with single electrons, the material exhibits metal-like behavior [Wang et al., 2018]. For most TMDs, a transition from the 1T phase to the 2H phase can occur through annealing or natural aging [Song et al., 2015]. For a detailed review of TMD polytypes and phase engineering, refer to [Wang et al., 2018; Voiry et al., 2015].

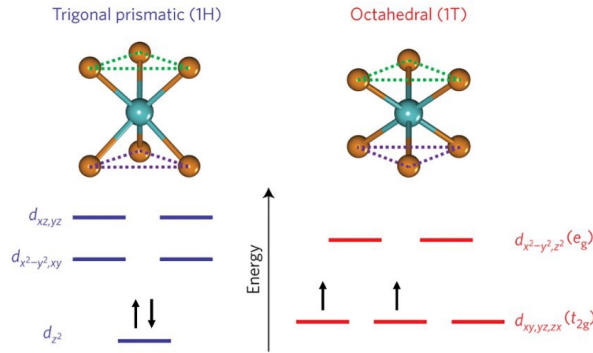


Figure 1.4: Comparison of *d*-orbital splitting caused by the crystal field in 1H-MoS<sub>2</sub> and 1T-MoS<sub>2</sub> [Yang et al., 2017].

A distinctive feature of this class of materials is that TMD monolayers exhibit direct bandgaps and optical properties that are highly dependent on their composition and phase. For instance, 2H-MoTe<sub>2</sub> (1.1 eV), MoSe<sub>2</sub> (1.5 eV), MoS<sub>2</sub> (1.8 eV), and WS<sub>2</sub> (2.1 eV) all possess direct bandgaps and can be combined to form ternary alloys to fine-tune properties such as bandgap, light emission, and light absorption. In contrast, their bulk counterparts typically exhibit indirect bandgaps. Fig. 1.5 provides an overview of the bandgaps of various 2D materials. Notably, these materials span the entire light spectrum, from UV (h-BN) to IR (MoSe<sub>2</sub>), making them suitable for a wide range of applications in photonics, including communication, light detection, lighting, microwaves, and terahertz technologies.

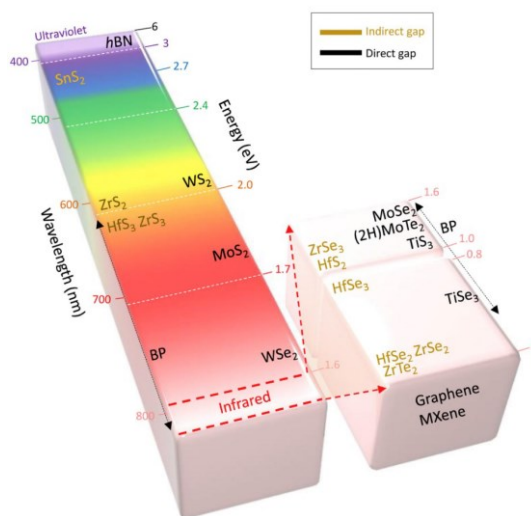


Figure 1.5: Bandgap of 2D materials, from graphene (zero bandgap) to h-BN. The color in the column represents the wavelength associated with the bandgap transition energy. Materials with indirect and direct bandgaps are indicated by different colors [Choi et al., 2017].

The band structures of selected TMD bilayers are illustrated in Fig. 1.6 Most TMDs exhibit a direct bandgap when isolated as monolayers. Additionally, as the material thickness decreases from bulk to around five layers, the indirect bandgaps tend to increase slightly, with a sudden shift to a much smaller direct bandgap in single-layer materials [Mak et al., 2010]. This behavior is typical of MoS<sub>2</sub> and WS<sub>2</sub>, two of the most common TMDs. However, some TMDs follow different bandgap trends or may not transition to a direct bandgap when reduced to a monolayer. For instance, in MoSe<sub>2</sub> and WSe<sub>2</sub> bilayers, the direct and indirect transitions occur at nearly the same energy level [Zhao et al., 2013]. MoTe<sub>2</sub>, on the other hand, already exhibits a direct bandgap when reduced to a bilayer [Lezama et al., 2015], while WSe<sub>2</sub> maintains an indirect bandgap even in monolayer form [Zhang et al., 2015]. Generally, the emission energies observed from direct transitions differ significantly from the material's bandgaps due to the high exciton binding energy, which remains substantial even at room temperature [Klots et al., 2014].

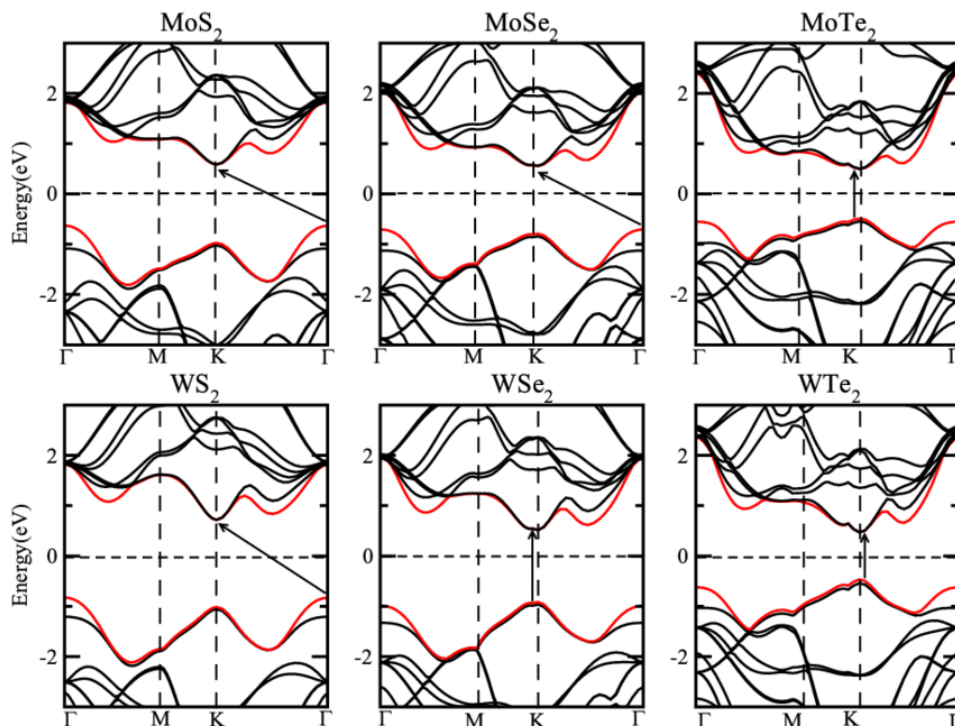


Figure 1.6: Electronic band structures of pristine AB-stacked bilayer TMDs with highlighted band gap transitions [Kumar et al., 2013].

Even though pristine crystalline TMDs exhibit remarkable properties, structural defects can easily arise during material growth or subsequent processing, leading to the deterioration of these properties. Therefore, understanding the nature of these defects and controlling their formation is crucial. A detailed review of defects in TMDs can be found in [Samadi et al., 2018]. Among the most common defects are sulfur vacancies that form during material

growth, significantly impacting surface oxygen absorption. In general, filling these sulfur vacancies with oxygen is thermodynamically favored, even under ambient conditions. Additionally, oxygen can be absorbed on the surface even without vacancies being present. Substitutional atoms also play a critical role in technological applications. The controlled introduction of such impurities forms the basis of doping processes. For instance, in MoS<sub>2</sub>, specific atoms can fill sulfur vacancies to act as dopants—N, As, P, or Sb atoms for n-type doping, and F, Cl, Br, or I atoms for p-type doping [Komsa et al., 2012]. Grain boundaries are another common defect in TMDs, generally leading to reduced electron mobility, a phenomenon that occurs regardless of the tilt angle between grains [Algara-Siller et al., 2013].

Due to their unique combination of properties, TMDs are highly attractive for applications in electronics, photonics, sensing, and energy devices. A schematic outlining some of these applications is provided in Fig. 1.7. Among these, there is growing interest in flexible nanotechnology, such as thin-film transistors (TFTs), displays, sensors, and solar cells. TMDs offer mechanical flexibility and strength similar to graphene. For example, in the absence of stacking faults and defects, the in-plane stiffness of a MoS<sub>2</sub> monolayer is approximately  $(180 \pm 60)$  N/m, corresponding to an effective Young's modulus comparable to that of steel ( $\sim 270$  GPa) [Bertolazzi et al., 2011]. Only carbon nanotubes and graphene among commonly used materials exhibit such a high Young's modulus [Bertolazzi et al., 2011]. Thanks to their flexibility, TMDs can mitigate effects related to the strain of the crystalline structure, such as bandgap deformation and shift. This property is essential for developing FETs on flexible or "wearable" substrates while maintaining the material's electrical properties.

The cornerstone of flexible electronics is the development of TFTs, as FET devices are fundamental to semiconductor technology. In recent years, prototypes of TFTs based on various TMDs have emerged [Choi et al., 2017], and it has been possible to achieve cutoff frequencies beyond 5 GHz on plastic substrates [Chang et al., 2016]. Additionally, MoS<sub>2</sub>-based TFTs demonstrate robust electronic performance under mechanical bending, enduring up to 3% strain [Yogeesh et al., 2016]. With their high on/off ratios, saturation velocity, and mechanical strength, TMDs are a promising solution for low-power radio frequency TFTs designed for flexible and wearable devices.

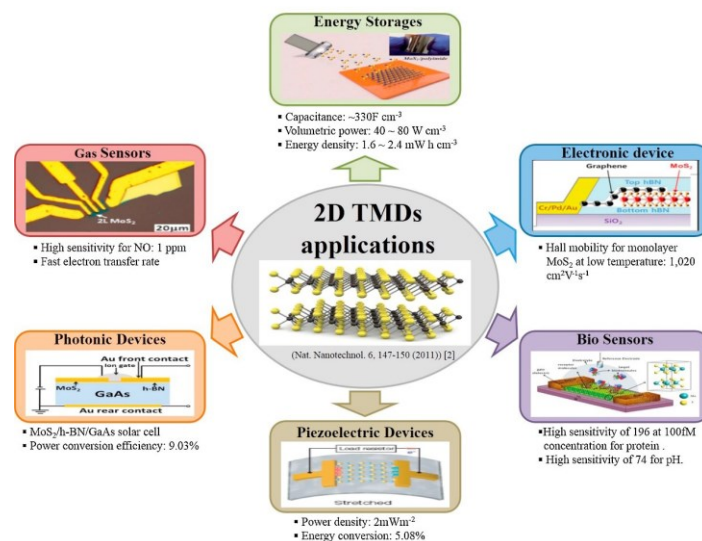


Figure 1.7: Electronic, opto-electronic and energy devices based on 2D transition metal dichalcogenides (TMDs) [Choi et al., 2017].

### 1.1.2 MoS<sub>2</sub> structure and Raman spectra

MoS<sub>2</sub> is the most extensively studied of the transition metal dichalcogenides (TMDs) and has been widely explored and utilized in device prototypes. Initially, research on MoS<sub>2</sub> focused on its bulk properties, particularly its effectiveness as a lubricant. This is due to its low friction coefficient, which is significantly smaller in the in-plane direction (0.10) compared to the perpendicular direction (0.26) [Song et al., 2015]. This behavior arises from the weak van der Waals interactions between layers, which are much weaker than the strong covalent bonds connecting the molybdenum (Mo) and sulfur (S) atoms within each layer. However, bulk MoS<sub>2</sub> is an indirect bandgap semiconductor with an energy gap of approximately 1.2 eV, resulting in a low quantum yield for photoluminescence (0.4% for a 1000-layer crystal). This characteristic limit its potential applications in optoelectronics [Mak et al., 2010].

MoS<sub>2</sub> exists in three polytypes: 1T, 2H, and 3R, with their respective crystal lattice parameters listed in Table 1.1 The metastable 1T-MoS<sub>2</sub> has octahedral symmetry and does not occur naturally; it can be synthesized from the other polytypes through chemical or



electrochemical exfoliation [Zhang et al., 2016] and can be converted into a more stable polytype through annealing [Song et al., 2015]. The 1T-MoS<sub>2</sub> polytype exhibits metallic behavior, while the 2H and 3R polytypes have semiconducting band structures. The 2H and 3R polytypes share similar lattice constants and layer thicknesses, as well as similar properties, with some differences in band structure and UV-VIS absorption spectrum [Song et al., 2015].

<i>MoS<sub>2</sub> polytype</i>		<i>2H</i>	<i>3R</i>	<i>1T</i>
<i>Lattice constant (Å)</i>	<b>a</b>	3.15	3.17	5.60
	<b>c</b>	12.30	18.38	5.99
<i>Stacking order</i>		AbA BaB	AbA BcB CaC	AbC

Table 1.1: Structural parameters of the main MoS<sub>2</sub> polytypes [Song et al., 2015].

The structure of 2H-MoS<sub>2</sub> is illustrated in Fig. 1.8 It consists of a hexagonal plane of molybdenum (Mo) atoms sandwiched between two hexagonal planes of sulfur (S) atoms, with strong covalent bonds linking the Mo and S atoms. These layers are stacked on top of each other, held together by weak van der Waals forces. The thickness of a single monolayer is 3.15 Å, while the spacing between adjacent layers is 3.49 Å [Song et al., 2015].

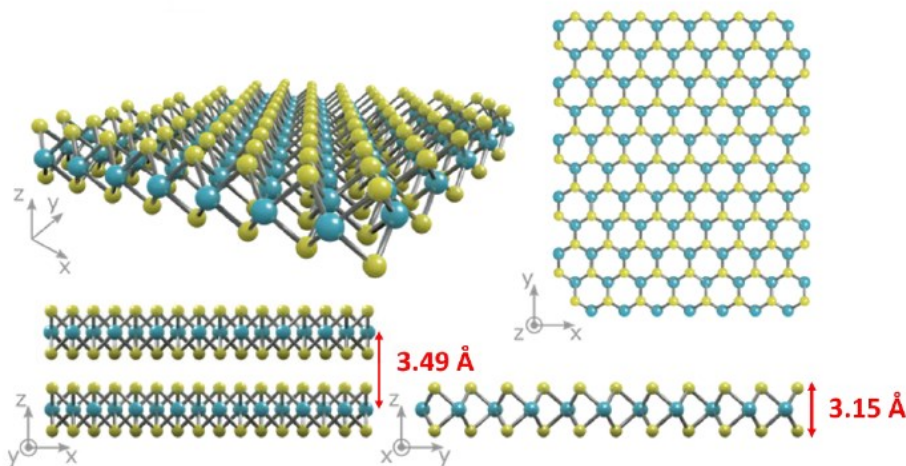


Figure 1.8: Detail of the crystal structure of monolayer MoS<sub>2</sub>: molybdenum atoms (blue) lie in a plane sandwiched between other two planes formed by sulfur atoms (yellow) [https://www.ossila.com/en-eu/pages/molybdenum-disulfide-mos2].

In terms of band structure, a 2H-MoS<sub>2</sub> monolayer exhibits significantly different electrical properties compared to its bulk form (Fig. 1.9). When the interlayer interactions are removed,

and electrons are confined to a single plane, the material transforms into a direct bandgap semiconductor with an increased bandgap of approximately 1.89 eV [Splendiani et al., 2010]. In bulk MoS<sub>2</sub>, the band transition occurs between the valence band maximum at the  $\Gamma$  point and the conduction band minimum, which lies between the  $\Gamma$  and K points. Density Functional Theory (DFT) calculations reveal that the conduction band states at the K point originate from the d orbitals of Mo atoms, which remain unaffected by interlayer coupling [Wang et al., 2012]. Conversely, the states at the  $\Gamma$  point result from a combination of Mo and S orbitals and are sensitive to changes in interlayer coupling. As the number of layers decreases, the band structure shifts, and direct transitions at the K point replace the indirect transitions, resulting in the formation of a direct bandgap material [Mak et al., 2010].

In a 2H-MoS<sub>2</sub> monolayer, the formation of a direct bandgap is linked to the emission of two excitonic peaks: one at approximately 1.92 eV (known as the A exciton) and another at around 2.08 eV (the B exciton) [Mak et al., 2010]. These peaks result from the splitting of the valence band at the K point due to spin-orbit coupling, which gives rise to two optically active transitions [Samadi et al., 2018]. Notably, excitons in this material remain stable even at high temperatures due to their strong binding energy, which exceeds 500 meV.

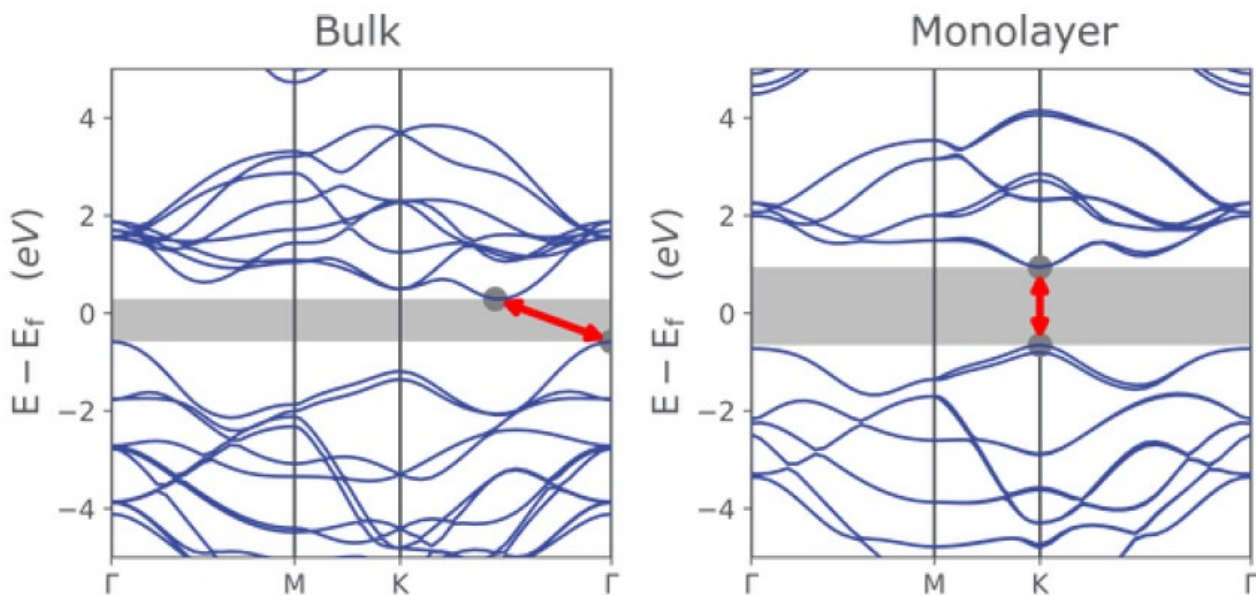


Figure 1.9: Band structure diagram of (left) bulk and (right) monolayer MoS<sub>2</sub> showing the crossover from indirect to direct bandgap accompanied by a widening of the bandgap [<https://www.ossila.com/en-eu/pages/molybdenum-disulfide-mos2>].

The analysis of Raman spectra offers valuable insights into the structure of MoS<sub>2</sub> layers. In the spectra of 2H-MoS<sub>2</sub>, four first-order Raman active modes can be identified: A<sub>1g</sub>, E<sub>2g</sub><sup>1</sup>, E<sub>2g</sub><sup>2</sup>, and E<sub>1g</sub> (Fig. 1.10). Of these, only the A<sub>1g</sub> and E<sub>2g</sub><sup>1</sup> modes are easily observable, typically appearing around 400 cm<sup>-1</sup>. In contrast, the E<sub>2g</sub><sup>2</sup> and E<sub>1g</sub> modes are not detectable in standard Raman spectroscopy and require more advanced techniques to be observed. The commonly observed Raman peaks correspond to in-plane (E<sub>2g</sub><sup>1</sup>) and out-of-plane (A<sub>1g</sub>) vibrations of atoms when viewed along the [100] direction [Ye et al., 2015]. The frequencies of these two modes exhibit a specific dependence on the film thickness.

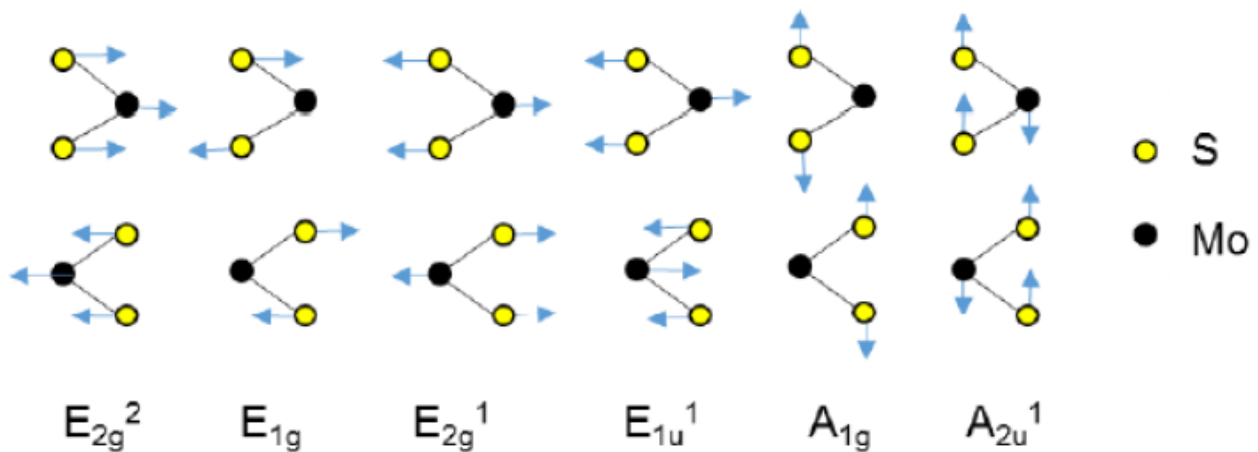


Figure 1.10. Atomic displacement vector of the four first-order Raman-active E<sub>2g</sub><sup>2</sup>, E<sub>1g</sub>, E<sub>2g</sub><sup>1</sup>, A<sub>1g</sub> modes and two IR-active E<sub>1u</sub><sup>1</sup> and A<sub>2u</sub><sup>1</sup> modes, as viewed along the [100] direction [Ye et al., 2015].

As the thickness of a MoS<sub>2</sub> film increases from a monolayer to bulk, the frequency of the E<sub>2g</sub><sup>1</sup> mode decreases (red-shift), while the frequency of the A<sub>1g</sub> mode increases (blue-shift) (Fig. 1.11a-b-c). This distinct relationship between peak width and frequency shift can be used to determine the number of MoS<sub>2</sub> layers, although this method is accurate for up to five layers and only in the absence of lattice strain or folded structures. Specifically, when the number of layers exceeds five, the peak separation surpasses 25 cm<sup>-1</sup>. Conversely, as the number of layers decreases from five to one, the peak separation narrows from 25 to about 18 cm<sup>-1</sup> (Fig. 1.11e). Additionally, as the number of MoS<sub>2</sub> layers increases, the Raman signal from the underlying Si substrate diminishes and disappears after about 20 layers.

The dependence of these two Raman modes on layer thickness can be explained using a simple van der Waals model. As the number of layers increases, the restoring force between interlayer S–S bonds strengthens, causing the A<sub>1g</sub> mode frequency to rise.

However, the  $E_{2g}^1$  mode experiences a red-shift as the layer thickness increases, which contrasts with the predictions of a classical coupled harmonic oscillator model, where only weak interlayer interactions are considered. The reduction in  $E_{2g}^1$  mode frequency with increasing layer thickness is partly due to the shorter intra-layer S-Mo-S distance in thinner  $\text{MoS}_2$ , indicating that stacking affects the intralayer structure. Furthermore, long-range Coulomb interlayer interactions must be considered to explain the anomalous red-shift of the  $E_{2g}^1$  mode as the thickness increases.

These observations suggest that two forces influence the interlayer interactions when transitioning from a monolayer to bulk  $\text{MoS}_2$ . The short-range force slightly increases due to enhanced restoring interactions between adjacent layers. However, the long-range force decreases because the layers extend beyond the effective charge, leading to Coulomb screening. This effect is particularly significant for Mo atoms. Since the  $E_{2g}^1$  mode involves in-plane vibrations of Mo atoms (see Fig. 1.11), the substantial reduction in long-range Coulomb interactions between Mo atoms outweighs the slight increase in short-range interactions. In contrast, the  $A_{1g}$  mode remains unaffected by Coulomb potential screening, as it involves only out-of-plane vibrations of S atoms.

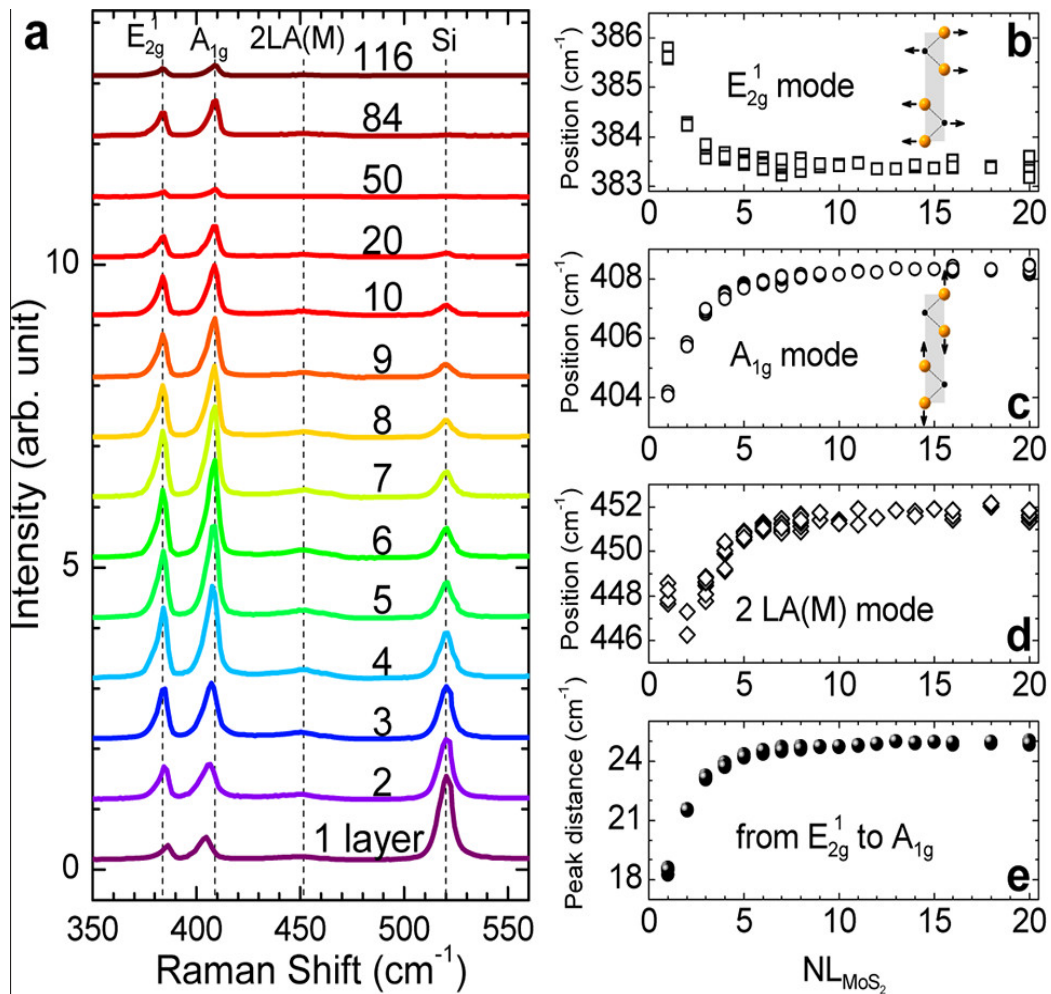


Figure 1.11: Evolution of the Raman spectra for MoS<sub>2</sub> flakes as a function of the material thickness: (a) Raman spectra of MoS<sub>2</sub> flakes for a number of layers ranging from 1 to 116; (b-d) Position evolution for the three principal Raman modes: E<sub>2g</sub><sup>1</sup>, A<sub>1g</sub> and 2-LA(M) as a function of the number of layers; (e) Peak distance between the E<sub>2g</sub><sup>1</sup> and A<sub>1g</sub> modes [Li et al., 2012].

### 1.3 TMD SYNTHESIS TECHNIQUE

Much research has been devoted to the synthesis and study of TMD properties. Right now, the significant issue that hinders the integration of TMDs into novel devices is the preparation of high quality TMDs on a large scale. It follows that a suitable synthesis method needs to be devised to obtain highly crystalline TMDs on wafer-scale areas compatible also with industrial processes. These processes need to be optimized for both single layer and Van der Waals heterostructures. The current synthetic techniques still require optimization to improve the material crystallinity, and they should be tailored over the desired substrates. For example, good quality graphene can be grown on Cu sheets [Alrefae et al., 2017], but not on Si substrates due to the Si-C reactivity. Additionally, the high thermal budget required for synthesizing 2D materials thwarts their integration with Si CMOS technology at the back-

end-of-line fabrication step where temperatures must not exceed 500 °C [Kozhakhmetov et al., 2020]. Despite these challenges, integrating 2D materials at the back-end-of-line is seen as a potential strategy to enhance the performance and multifunctionality of Si CMOS-based devices.

### 1.3.1 Mechanical exfoliation

Mechanical exfoliation, originally used for graphene, has been successfully applied to various 2D materials. This top-down method involves exfoliating bulk crystals using adhesive tape, overcoming the weak interlayer bonding forces (Fig. 1.12) It is a cheap, fast, and versatile technique, widely used for h-BN, TMDs, and MoS<sub>2</sub>, where it enables the quick fabrication of mono- or few-layer samples. The obtained flakes are usually high quality but limited in size (hundreds of μm) [Zavabeti et al., 2020]. Moreover, the technique's unreliable thickness control poses challenges for TMD-based optoelectrical devices. Laser thinning can be used to address local thickness variations, but a reliable and scalable mechanical exfoliation method for large-scale industrial use is lacking. Contamination is another issue, that can severely degrade device performance [Das et al., 2015]. Despite these downsides, mechanical exfoliation remains the best method for obtaining high-quality few-layer TMDs and is widely used in research and made possible most of the reported results in the literature [Wang et al., 2015].

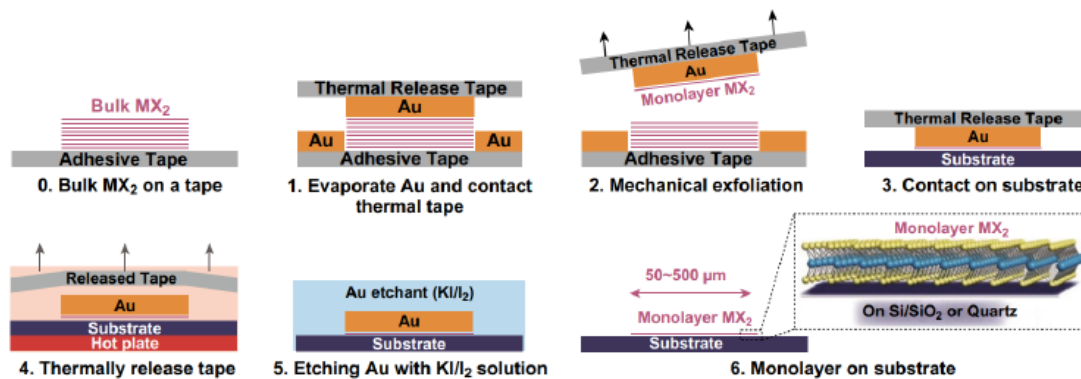


Figure 1.12: Schematic illustration of the Au exfoliation process from a bulk MX<sub>2</sub> crystal [Zavabeti et al., 2020].

### 1.3.1 Chemical vapor deposition

Chemical vapor deposition (CVD) is a widely used bottom-up technique for fabricating single-crystal islands of atomically thin TMDs over large areas. CVD forms solid products through gaseous reactions on substrates. Properties of the material, such as size, morphology, and dopants, can be controlled by adjusting parameters like temperature,

pressure, gas type, and flow rate [Zhang et al., 2019]. A detailed review of CVD for TMD growth can be found in reference [Cai et al., 2018].

CVD techniques are usually categorized into two approaches:

- Chalcogenization of pre-deposited metal precursors and vaporization.
- Direct reaction of both metal and chalcogen precursors.

The first approach (Fig. 1.13) is one of the simplest and involves depositing transition metals (e.g., Mo, W, Nb) via techniques like DC-sputtering [Wu et al., 2017], producing large-area homogeneous films, limited by substrate size [Ji et al., 2015]. Post-chalcogenization with S or Se powders forms TMDs but results in small crystalline domains and non-uniform films. The use of  $H_2S$  gas as a sulfur precursor improves uniformity but this requires specific equipment due to toxicity and flammability [Lee et al., 2014]. Still, high substrate temperatures of more than  $750^\circ C$  hinder TMD growth on pre-existing structures [Pawbake et al., 2016].

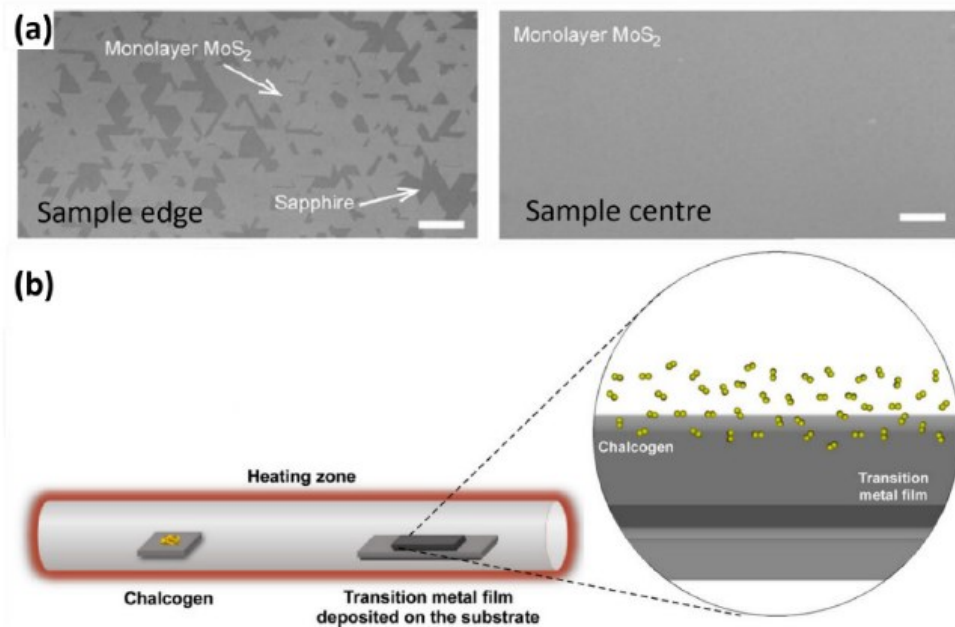
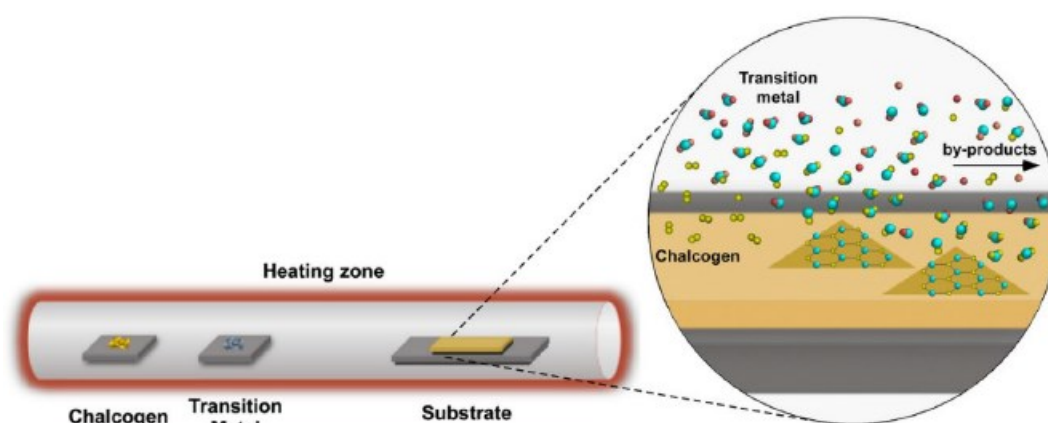


Figure 1.13: (a) Optical microscope images of a  $MoS_2$  sample grown by CVD, which produces well-defined equilateral triangular single-crystal domains that merge into a continuous monolayer film in the centre of a sapphire substrate ( $6\text{ mm} \times 1\text{ cm}$ ). The scale bars are  $20\text{ nm}$  for the left image and  $10\text{ nm}$  for the right image respectively. [Li et al., 2015]. (b) Schematics of vapor phase

*chalcogenization of pre-deposited precursor (metal, metal oxide, etc.) film for the synthesis of large-area TMDs [Hernandez et al., 2022].*

The second CVD approach involves instead an initial step where metal oxide precursors (e.g.,  $\text{MoO}_3$ ,  $\text{WO}_3$ ) are evaporated and reduced to suboxides on the substrate (Fig. 1.14)  $\text{MoO}_3$  combined with S powder is usually employed for powder vapor transport (PVT) growth of  $\text{MoS}_2$ , known as powder source CVD. Although  $\text{MoO}_3$  is stable and non-hazardous, its high melting temperature ( $\sim 800^\circ\text{C}$ ) requires heating to over  $600^\circ\text{C}$  for effective vapor pressure, necessitating placement close to the substrate for adequate vapor flux.



*Figure 1.14: Schematics of a one-step powder vapor transport (PVT) CVD growth of TMDs [Hernandez et al., 2022].*

Although CVD is commonly used, it has a low growth rate and produces non-uniform samples, which are not ideal for industrial processes [Das et al., 2015]. These issues can be addressed with gas source CVD or metal-organic CVD (MOCVD), which use gas-phase precursors like  $\text{Mo}(\text{CO})_6$  and  $(\text{C}_2\text{H}_5)_2\text{S}$ , and can control growth with high precision [Choudhury et al., 2020]. MOCVD allows for layer-by-layer growth and excellent material uniformity at lower substrate temperatures ( $< 500^\circ\text{C}$ ), but low-temperature processes can lead to poor layer control and small grain sizes [Kozhakhmetov et al., 2020].

Atomic layer deposition (ALD) is a common CVD method where precursors are introduced alternately to maintain a self-limiting regime and avoid intermixing [Tan et al., 2014]. ALD can achieve full substrate coverage with a continuous  $\text{MoS}_2$  monolayer, but the films are initially amorphous and require high-temperature annealing [Mattinen et al., 2023].





Figure 1.15: Schematics of an atomic layer deposition process (ALD) [Mattinen et al., 2023].

Molecular beam epitaxy (MBE) is ideal for epitaxial growth of ultrathin films, using thermal or electron-beam evaporation of solid-source precursors to produce epitaxial films on crystalline substrates [Choudhury et al., 2020]. MBE allows precise control over source flux and in-situ characterization, but for TMDs, it requires high temperatures (>700 °C) due to reduced surface mobility of transition metals like Mo and W. At temperatures below 500 °C, MBE results in poor film morphology and non-coalesced domains.

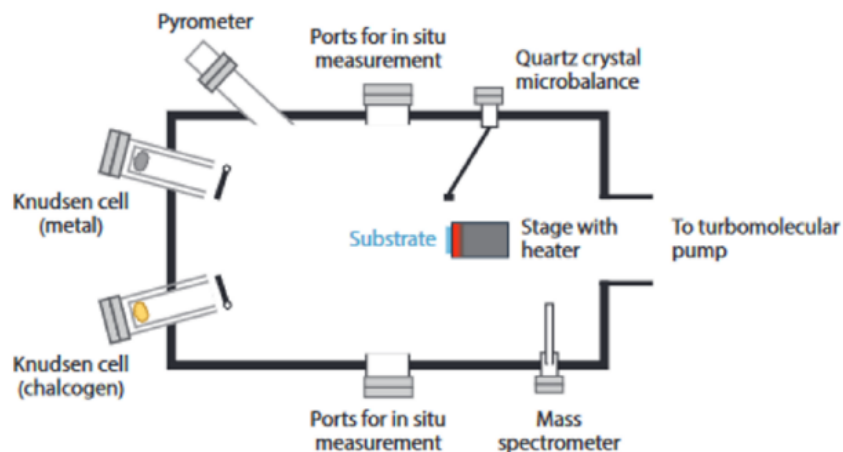


Figure 1.16: Schematics of powder vapor transport (PVT) MBE growth of TMDs [Choudhury et al., 2020].

Integrating TMDs into the back-end-of-line (BEOL) of Si CMOS technology requires a method that produces wafer-scale layers while keeping the substrate temperature below 500 °C. Process conditions and expected crystal sizes for various synthesis methods are summarized in Fig. 1.17. Even if growth temperatures stay within BEOL limits, post-growth annealing needs higher temperatures, and low-temperature processes often lead to poor morphology control and small or isolated crystals.

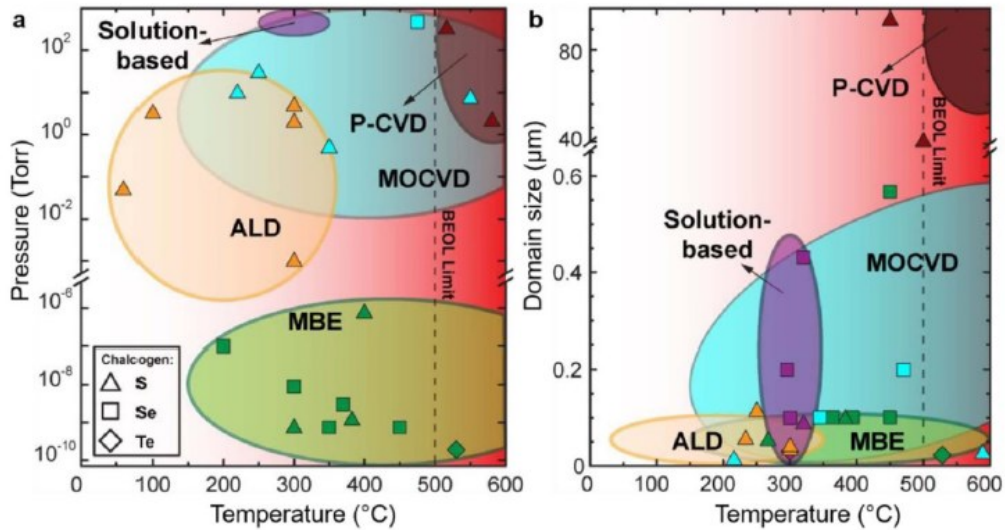


Figure 1.17: (a) CVD, MOCVD, MBE, ALD and solution-based synthesis condition of TMDs as a function of the growth temperature. (b) Map of the crystals domain size as a function of the growth temperature [Kozhakhmetov et al., 2020].

### 1.3.3 Radio frequency magnetron sputtering-based techniques

Radio frequency magnetron sputtering (RFMS), introduced in 1974, is a reliable and cost-effective coating method with high deposition rates up to 10 nm/s [Brauer et al., 2010]. It can deposit various materials, including metals, insulators, and some TMDs like MoS<sub>2</sub> and BN. RFMS is noted for its homogeneous, large-area films with good reproducibility and control over surface morphology and composition [Musil et al., 1998].

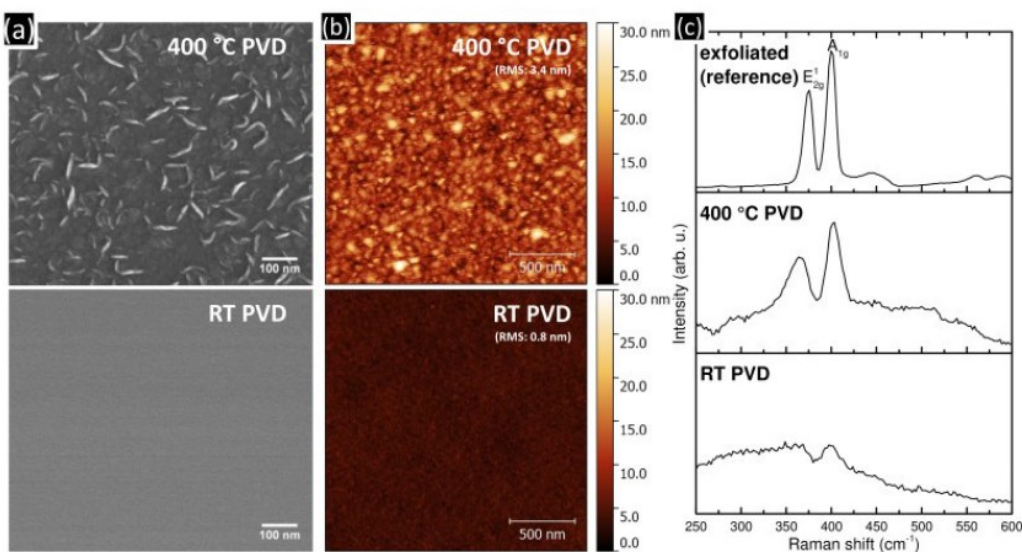


Figure 1.18: (a) SEM and (b) AFM images of MoS<sub>2</sub> ( $\approx 100$  nm) deposited at RT and 400 °C. (c) Ex situ Raman spectra of MoS<sub>2</sub> films deposited at RT ( $\approx 1000$  nm) and 400 °C ( $\approx 100$  nm), compared to an exfoliated MoS<sub>2</sub> crystal as reference. [Kaindl et al., 2017].

During RFMS, plasma ions bombard a target material, however it is difficult to keep the correct stoichiometry due to preferential sputtering and target erosion. Using a MoS<sub>2</sub> target in RFMS can lead to preferential sputtering of chalcogen due to its higher vapor pressure, affecting film stoichiometry [Baker et al., 1999]. This issue can be mitigated by using reactive sputtering gases like H<sub>2</sub>S [Jang et al., 2020]. Another challenge is chalcogen desorption during growth, which can be addressed by low-temperature sputtering (room temperature to 400 °C) followed by post-annealing (300-700 °C) [Samassekou et al., 2017]. This method results in high-quality MoS<sub>2</sub> films with conductivity comparable to CVD and mechanical exfoliation. There are many different approaches that based on sputtering, with a complete review reported in the reference [Acar et al., 2021].

## 1.4 FIELD EFFECT TRANSISTORS (FET)

### 1.4.1 FET working principles and model

Modern electronics rely on field-effect transistors (FETs), which are voltage-controlled devices used in various applications including high-power and high-frequency switching, RF amplifiers, voltage-controlled resistors, and logic circuits [Qian et al., 2019]. FETs operate with an active channel where carriers, either electrons or holes, flow to generate a drain current  $i_{DS}$ . This channel is situated between two electric contacts: the source and the drain. The voltage difference  $V_{DS}$  between these contacts is crucial for controlling the device's operation as it alters the channel's conductivity. Another key parameter is the gate-to-source voltage  $V_{GS}$ . In the most common FET type, the metal-oxide-semiconductor FET (MOSFET), the gate is isolated from the channel by a dielectric layer (such as an oxide), as shown in Fig. 1.19-a for a MoS<sub>2</sub> channel. When  $V_{GS}$  is not applied, no conductive channel forms, and the threshold voltage  $V_{TH}$  is needed to turn on the device  $V_{GS} > 0$ .

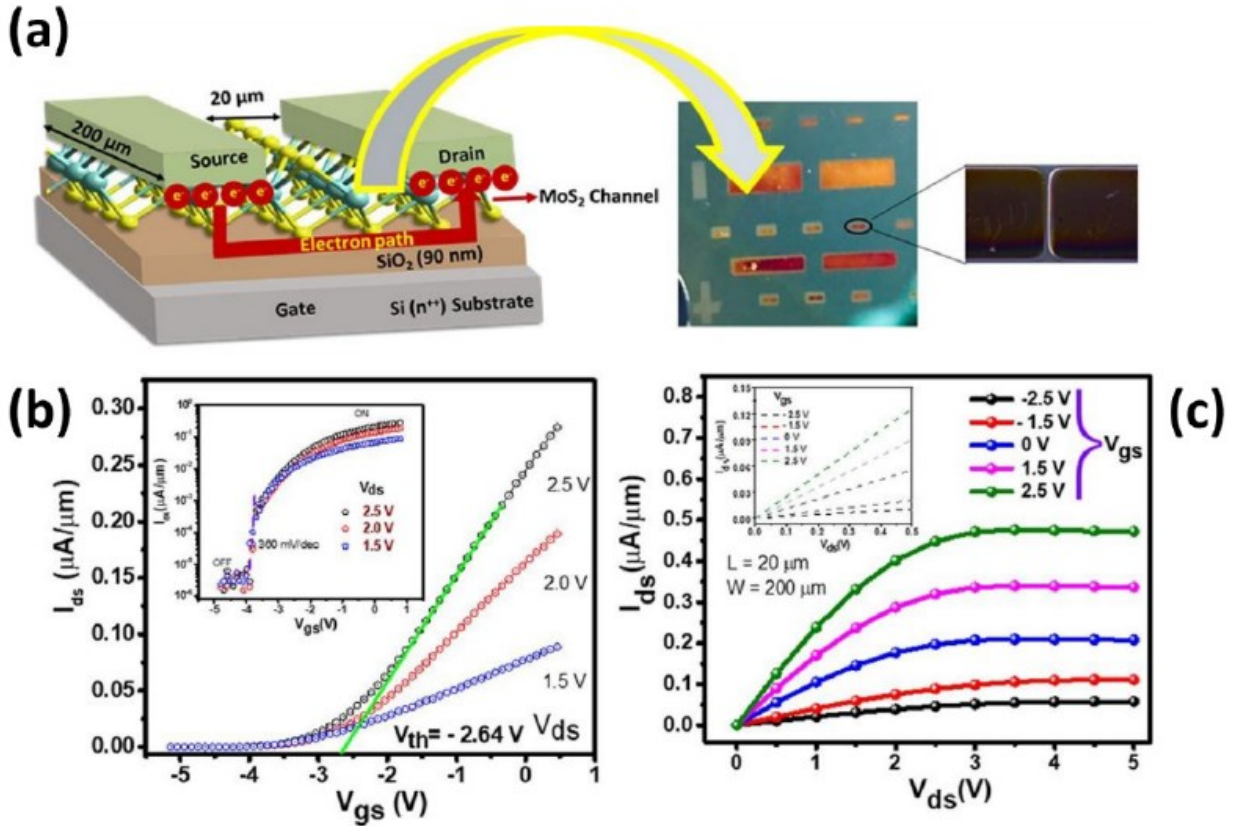


Figure 1.19: Schematic of: (a) FET created using as active channel a MoS<sub>2</sub> crystal; (b) transfer, and (c) output curve of the device represented in (a) [Kumar et al., 2021].

For an n-type MOSFET, once  $V_{GS}$  is high enough to create a conductive layer near the oxide interface, the device's behavior depends on whether  $V_{GS}$  is greater or less than  $V_{DS}$ . When  $V_{GS} > V_{DS}$  the MOSFET operates in the linear region like a resistor, with the drain current expressed as:

$$i_D = \frac{\mu C_{OX} W}{L} [(V_{GS} - V_{TH})V_{DS} - V_{DS}^2]$$

where  $\mu$  is the carrier mobility,  $C_{OX}$  is the capacitance of the dielectric layer,  $W$  is the channel width, and  $L$  is the channel length.

When  $V_{GS} < V_{DS}$ , the channel enters the pinch-off region: it becomes wedge-shaped, thinner near the drain. Despite this, conduction still occurs due to the high  $V_{DS}$ , and the drain current is primarily controlled by  $V_{GS}$ , approximated as:

$$i_D = \frac{\mu C_{OX} W}{2L} (V_{GS} - V_{TH})^2$$

Fig. 1.19b and c illustrate these variations in  $i_{DS}$  with respect to  $V_{DS}$  and  $V_{GS}$ .

For digital logic FETs, a significant difference between the on and off states is crucial. The on current  $i_{ON}$  is defined as the current when  $V_{GS} = V_{DS} = V_{DC}$ , where  $V_{DC}$  is the supply voltage. The off current  $i_{OFF}$  is measured when  $V_{GS} = 0$  and  $V_{DS} = V_{DC}$ . Digital applications require an on-off ratio of approximately  $10^4$  to  $10^7$  [The International Technology Roadmap for Semiconductors, [http://www.itrs.net.](http://www.itrs.net)], so  $i_{OFF}$  should be minimized and  $i_{ON} / i_{OFF}$  maximized.

Contact resistance is another critical factor. The channel's conductivity is not only influenced by the gate-source voltage but also by the potential difference between the gate and the channel at the source, as well as  $V_{DS}$ . Additional series resistances in the source and drain regions, and at the metal-semiconductor interfaces, can degrade device performance. Therefore, it is important to reduce contact resistance by choosing the appropriate metal for each semiconductor material [Schwierz et al., 2015].

#### **1.4.2 Limitations of modern devices and rationale for TMD based FETs**

The scaling of silicon-based FETs has highlighted significant issues related to channel control, particularly due to short channel effects (SCEs) when channel lengths approach the depletion layer widths of the source and drain junctions. These effects comprise drain-induced barrier lowering, velocity saturation, quantum confinement, and hot carrier degradation [Jeong et al., 2020]. Various solutions have been proposed to address these limitations, such as adopting multi-gate architectures [Ferain et al., 2011] or applying strain to the silicon lattice [Thompson et al., 2002].

Currently, 2D TMDs offer a promising alternative for FET channel materials, thanks to their advantageous properties like naturally passivated surfaces, tunable bandgaps, and potentially high mobility [Wang et al., 2017; Chhowalla et al., 2016]. Additionally, combining different TMDs can exploit their diverse bandgaps and the benefits of van-der Waals structures [Li et al., 2014]. However, the industrial-scale adoption of TMD-based FETs is constrained by the size and quality of TMD films, which are often limited to micrometer-scale flakes.

For  $\text{MoS}_2$  films used in FET prototypes, as shown in Fig. 1.20a-b, typical carrier mobility for pristine exfoliated monolayers is around  $0.5 - 3.0 \text{ cm}^2/\text{Vs}$  at room temperature, which is relatively low due to surface impurities, defects, traps, and significant phonon scattering

[Huo et al., 2018]. Charge traps at the substrate interface are a major factor contributing to low mobility in MoS<sub>2</sub> devices [Ghatak et al., 2011]. Electron mobility for monolayer MoS<sub>2</sub> varies widely (from 1 to 1000 cm<sup>2</sup>/Vs) due to differences in material quality, fabrication methods, and measurement conditions. n-type behavior is commonly observed, as depicted in Fig. 1.20c, and mobility enhancement can be achieved by adding a top gate dielectric material such as HfO<sub>2</sub> [Radisavljevic et al., 2011]. To optimize FET performance, particular attention is needed for electrical contacts, typically made of Au or Ti. As channel lengths decrease, contact resistance  $R_C$  becomes a significant factor. As illustrated in Fig. 1.21d, the total device resistance  $R_{TOT}$  is the sum of channel resistance and a constant contact resistance term  $2R_C$ , with the latter obtained from the vertical intercept of a linear fit of  $R_{TOT}$  versus channel length ( $L$ ). Smaller contact dimensions, necessary for scaled transistors, increase contact resistance [English et al., 2016]. Fig. 1.21e shows that different contact materials yield varying resistance values. Ti, with a work function close to MoS<sub>2</sub> (4.3 eV and 4.0 eV respectively), is better suited for ohmic contacts with lower resistance. Mo contacts, however, have a small 0.1 eV Schottky barrier at the MoS<sub>2</sub> interface [Kang et al., 2014]. Achieving a clean metal-MoS<sub>2</sub> interface is crucial for reducing contact resistance, as demonstrated by recent work showing that e-beam evaporation contact deposition is sensitive to process pressure, with higher pressures leading to less clean surfaces and increased resistance [English et al., 2016].

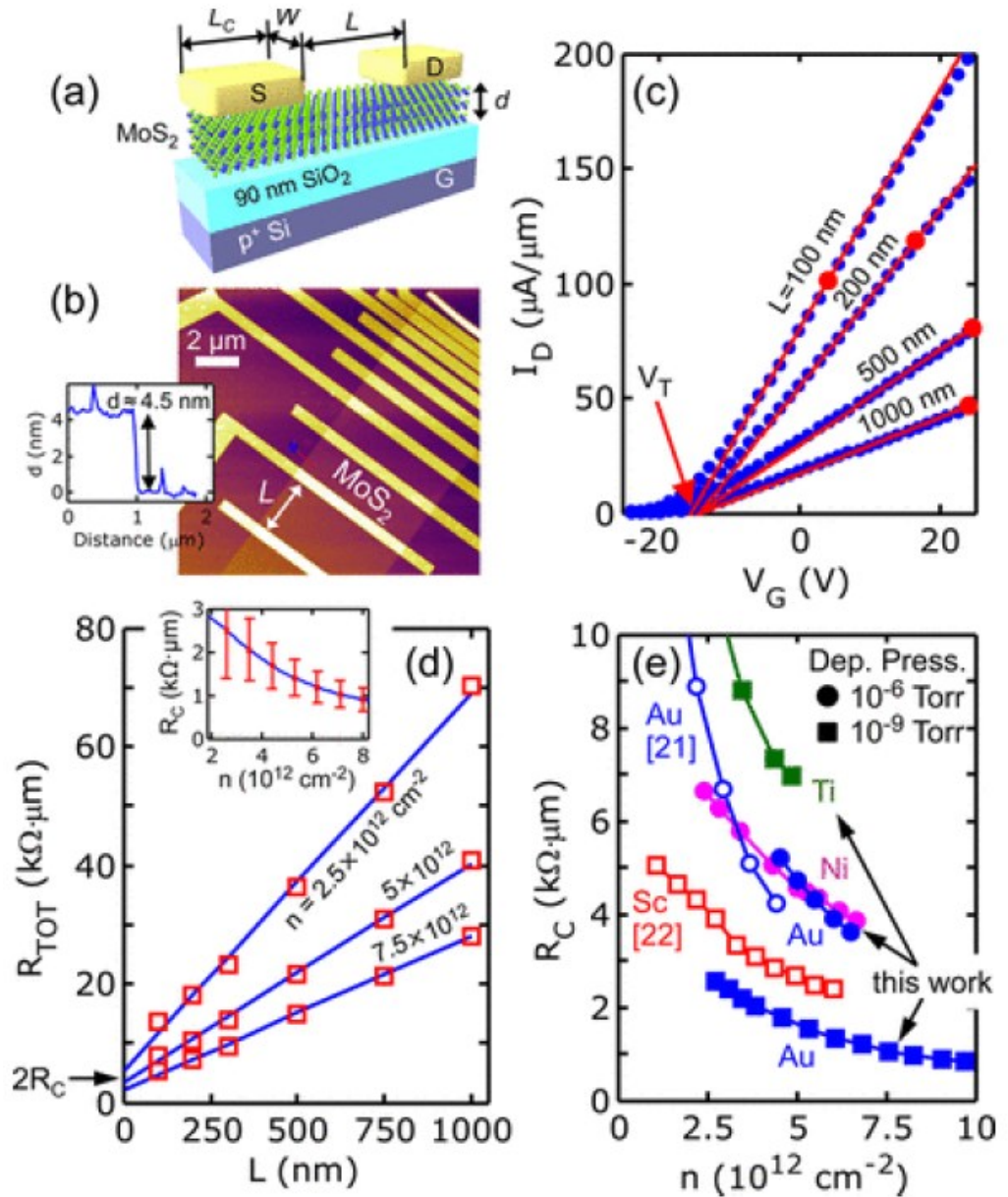


Figure 1.20: (a) Schematic of a MoS<sub>2</sub> devices. (b) AFM image of TLM structure on MoS<sub>2</sub>. Inset: AFM cross-section of height profile. (c) Measured current vs gate voltage ( $V_D = 1$  V) for Au electrodes. (d) Total device resistance vs length for various carrier densities. Inset:  $R_C$  vs  $n$  for “clean” Au contacts. (e) Measured  $R_C$  vs  $n$  for multiple contact metals at different deposition pressures. Lower deposition pressures lead to cleaner interfaces and lower  $R_C$  [English et al., 2016].

### 1.4.3 Mobility

Electrical conductivity is significantly affected by both charge carrier density and mobility.

Mobility ( $\mu$ ) is defined as:

$$\mu = \sigma / en$$

where  $\sigma$  is the conductivity, and  $n$  is the carrier density. In many studies, field-effect mobility ( $\mu_{FE}$ ) is approximated from transfer curves, as determining exact carrier density can be challenging. Carrier density can be adjusted through electrostatic or electrochemical gating in a FET. A simple setup involves two metal electrodes (source and drain), with a third gate electrode inducing positive or negative charges on the sample surface via a dielectric material. In this configuration, the variation of  $I_{DS}(V_{GS})$  as a function of  $V_{DS}$  allows for calculating carrier mobility ( $\mu$ ) in MoS<sub>2</sub> thin films. Mobility ( $\mu$ ) can be determined using the equation:

$$\mu_{FE} = - \frac{L}{WC_{OX}V_{DS}} \frac{\partial I_{DS}}{\partial V_{GS}}$$

where  $L$  is the channel length (varies between devices),  $W$  is the channel width,  $V_{DS}$  is a fixed value (e.g., 1 V), and  $C_{OX}$  is the capacitance of the underlying oxide (SiO<sub>2</sub>) per unit area, calculated as:

$$C_{OX} = \frac{\epsilon_{OX}\epsilon_0}{d}$$

where  $d$  is the dielectric film thickness,  $\epsilon_{OX}$  is the dielectric constant of the oxide (3.80 for SiO<sub>2</sub>), and  $\epsilon_0$  is the vacuum dielectric constant. The gate can be configured in either a back-gated geometry, usually with a heavily doped silicon substrate and thermal oxide, or a top-gated configuration with an additional dielectric material and metal contact. Electronic doping can be enhanced by adding a top gate terminal, which enables stronger doping through the use of a high dielectric constant and thinner oxide layer, such as HfO<sub>2</sub>, compared to the typical bottom gate SiO<sub>2</sub> layer [Radisavljevic et al., 2013].

Monolayer MoS<sub>2</sub> FETs typically exhibit n-type behavior, turning on when a positive gate bias is applied and showing sheet resistance in the range of several k $\Omega$  [Schmidt et al., 2015]. Theoretically, phonon scattering is expected to be the primary factor limiting mobility [Kaasbjerg et al., 2012], but experimental studies often report much lower mobility, usually below 1000 cm<sup>2</sup>/Vs even at low temperatures. This suggests that other factors, such as impurities and defects, play a significant role, especially at lower temperatures [Schmidt et al., 2015]. The mobility values for various MoS<sub>2</sub> devices reported in the literature, shown in Fig. 1.21, vary widely due to differences in material quality, device fabrication processes, and measurement conditions. Interestingly, no significant differences in mobility are observed between mechanically exfoliated and CVD-grown MoS<sub>2</sub> samples, indicating that point defects have a greater impact than grain boundaries, which are typically associated



with CVD-grown layers [Schmidt et al., 2015]. Additionally, at room temperature, mobility tends to increase with the number of layers, likely due to a reduced impact of charged impurities in thicker samples [Li et al., 2013]

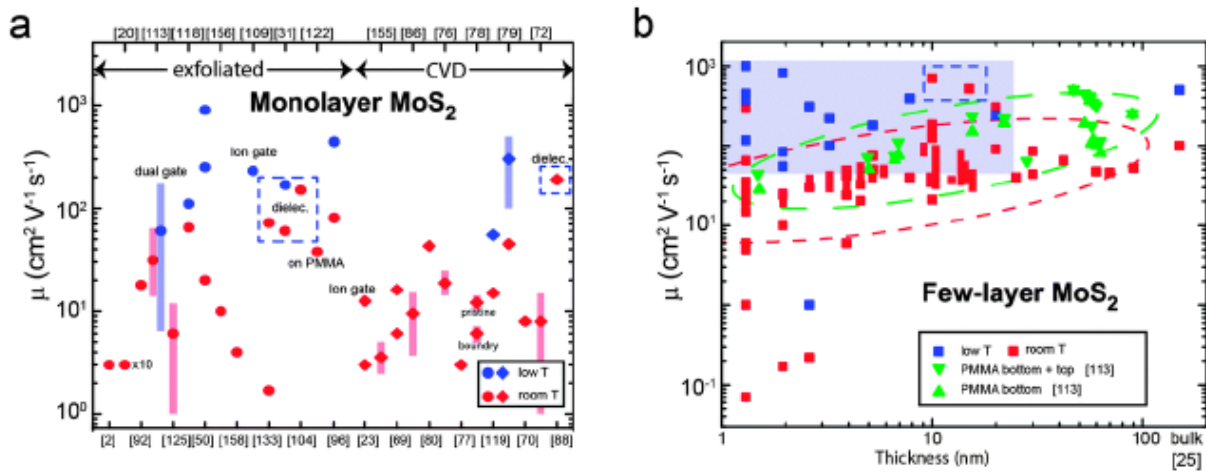


Figure 1.21: Carrier mobilities reported for (a) monolayer and (b) few-layer  $\text{MoS}_2$  [Schmidt et al., 2015].

#### 1.4.4 Doping

To further adjust the electrical properties of 2D materials, introducing dopants is the most effective method. However, doping methods must be carefully designed to preserve the structure and intrinsic properties of these materials. A detailed review of doping techniques and their outcomes can be found in [Yoo et al., 2021], but only key aspects are discussed here.

TMD doping can be divided into two main approaches: atom-substitutional and molecular doping. In atom-substitutional doping, a dopant atom replaces one of the compound's atoms without disrupting the crystal structure. In contrast, molecular doping involves either charge transfer from a dopant molecule or utilizing its dipole effect [Yoo et al., 2021].

Research shows that both atomic species, such as Mo [Yue et al., 2020] and S [Kim et al., 2020], can be substituted. For example, Ti doping can yield either n-type or p-type materials by adjusting the doping level and site [Samy et al., 2021]. This substitution forms a new chemical bond, offering a more stable doping effect than charge transfer doping. However, molecular doping has advantages such as low-cost, large-area processing [Yoo et al., 2021]. Molecular doping typically results in a heterostructure, with the doping film adsorbed onto the  $\text{MoS}_2$  layer. In charge transfer doping, physical adsorption occurs, so air stability must be considered [Fang et al., 2013]. Dipole-effect doping, such as with transition metal oxides [Xu et al., 2017], offers better stability and is often combined with self-assembled

monolayers (SAMs), where these materials form a junction on the TMD surface, creating an interface dipole [Kang et al., 2015].

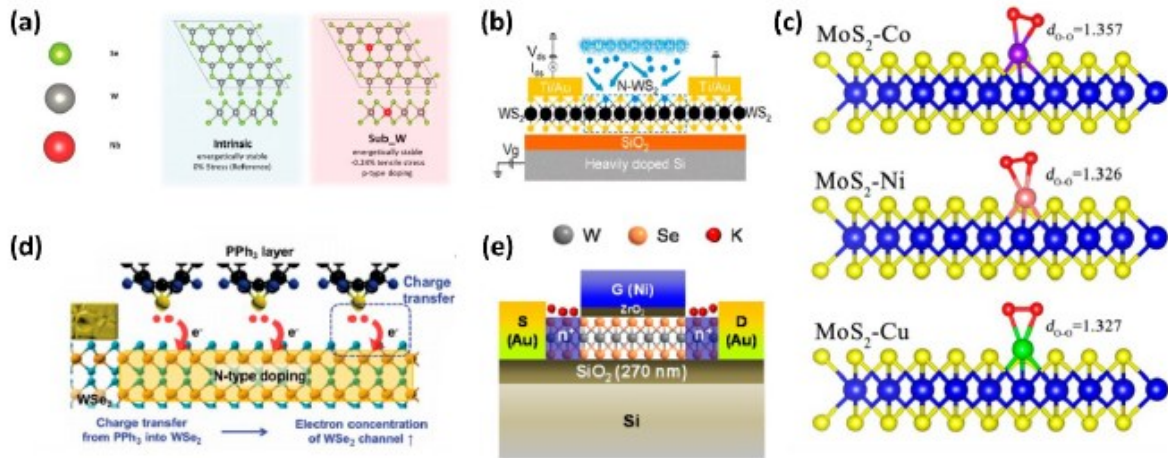


Figure 1.22: Examples of different doping techniques for TMDs. (a) Nb-doped WSe<sub>2</sub> monolayer for DFT calculations. (b) Cross-sectional view of bottom-gated monolayer WS<sub>2</sub> FETs doped by atomic nitrogen treatment. (c) Structure and charge density difference for intermediate OOH adsorption on hydrogenated MoS<sub>2</sub>-TM (Co, Ni and Cu). (d) Schematic of a top-gate WSe<sub>2</sub> transistor with chemically n-doped source/drain contacts by K exposure (e) Diagram for n-doping mechanism of PPh<sub>3</sub> at the PPh<sub>3</sub>/WSe<sub>2</sub> interface [Yoo et al., 2021].

### 1.4.5 FET fabrication technique

When fabricating micro- or nanoscale devices, specialized techniques are essential for creating precise patterns and contacts. Lithography is particularly critical for achieving accurate patterns. Over the past few decades, micro- and nanolithography have played a key role in the integrated circuit manufacturing industry. Lithographic techniques enable patterning at scales ranging from nanometers to tens of millimeters. These methods fall into two categories: mask-based and maskless lithography.

Mask-based lithography enables high production rates by working over large areas simultaneously. One of the most prominent processes in this category is photolithography [Pimpin et al., 2012].

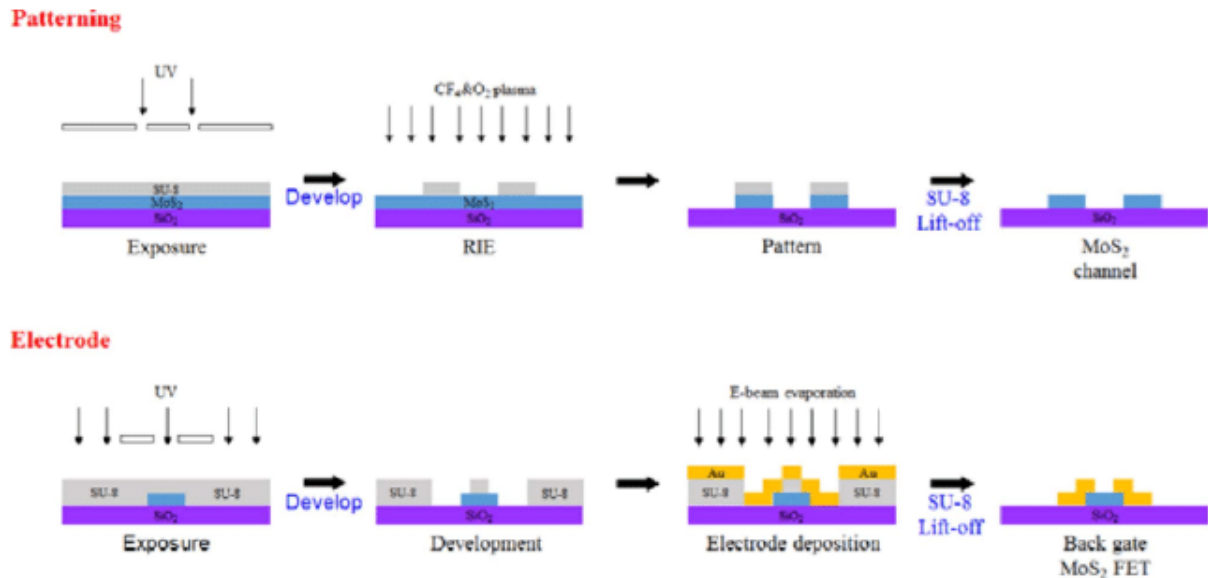


Figure 1.23: Example of process flow for device fabrication by photolithography [Joung et al., 2017].

Photolithography involves exposing light-sensitive polymers, known as photoresists, to UV light through a mask that selectively illuminates the photoresist. The exposed areas are modified and can be easily removed, leaving behind the desired pattern. Photolithography has been successfully applied to fabricate low-voltage, high-current FET devices based on CVD-grown, large-scale MoS<sub>2</sub> [Kwon et al., 2019]. These devices achieved linear mobility of 10 cm<sup>2</sup>/Vs, an ON/OFF ratio of 10<sup>8</sup>, and a fabrication success rate of 80% when operating at 5 V.

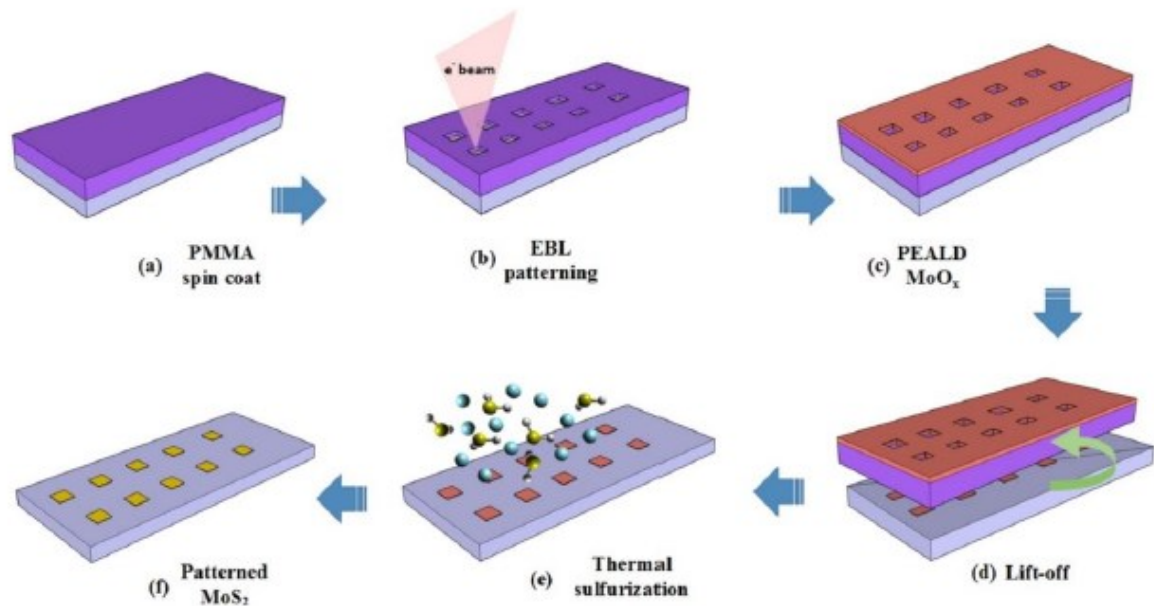


Figure 1.24: Process scheme for patterned MoS<sub>2</sub> synthesis, combining EBL and ALD [Sharma et al., 2020].

On the other hand, maskless lithography techniques, such as electron beam lithography (EBL), offer ultra-high resolution for creating complex patterns of arbitrary shapes, with feature sizes reaching a few nanometers. However, this precision comes at the expense of lower throughput, limiting its use in industrial-scale processes. Despite this, EBL remains a leading technique for fabricating nanoscale patterns. During EBL, an electron beam is accelerated and focused onto electron-sensitive resists. The beam, typically just a few nanometers wide, scans the resist surface to generate a pattern. Resolutions of 5-20 nm are common, determined by the electron wavelength. One of the main challenges of EBL is that even low-dose electron beams can alter the structure of MoS<sub>2</sub> films. Nevertheless, EBL is well-suited for fabricating FETs from triangular-shaped monolayers of MoS<sub>2</sub> (i.e., single flakes) and can even be used to tailor the band structure of MoS<sub>2</sub> films [Zheng et al., 2019].

Generally, research has been more focused on fabricating and characterizing devices on flakes of MoS<sub>2</sub> either obtained via exfoliation or via CVD. However, in order to integrate TMDS into novel devices it is necessary to process continuous films of these materials using a high-throughput lithography technique such as photolithography. This thesis work addresses this issue by exploring the fabrication of FET devices using photolithography on a continuous film of MoS<sub>2</sub> that is one to three monolayer thick.

## CHAPTER 2: EXPERIMENTAL

### WORKPLAN

The MoS<sub>2</sub> samples used in this work were supplied by CEA-LETI within the framework of the ASCENT+ project. The structure of these samples consists either of a 1 or 2/3 monolayer thick MoS<sub>2</sub> film deposited on a SiO<sub>2</sub>/Si substrate, where the SiO<sub>2</sub> layer is 500 nm thick, while the underlying Si is p-doped. The MoS<sub>2</sub> was synthesized via Atomic Layer Deposition (ALD) using a Molybdenum Tetrakis(dimethylamide) [Mo(NMe<sub>2</sub>)<sub>4</sub>] organometallic precursor and 1-2-ethanedithiol [HS(CH<sub>2</sub>)<sub>2</sub>SH] [Cadot et al. 2017]. HRTEM images of the film show that the resulting film is polycrystalline with domain sizes of 10-20 nm.

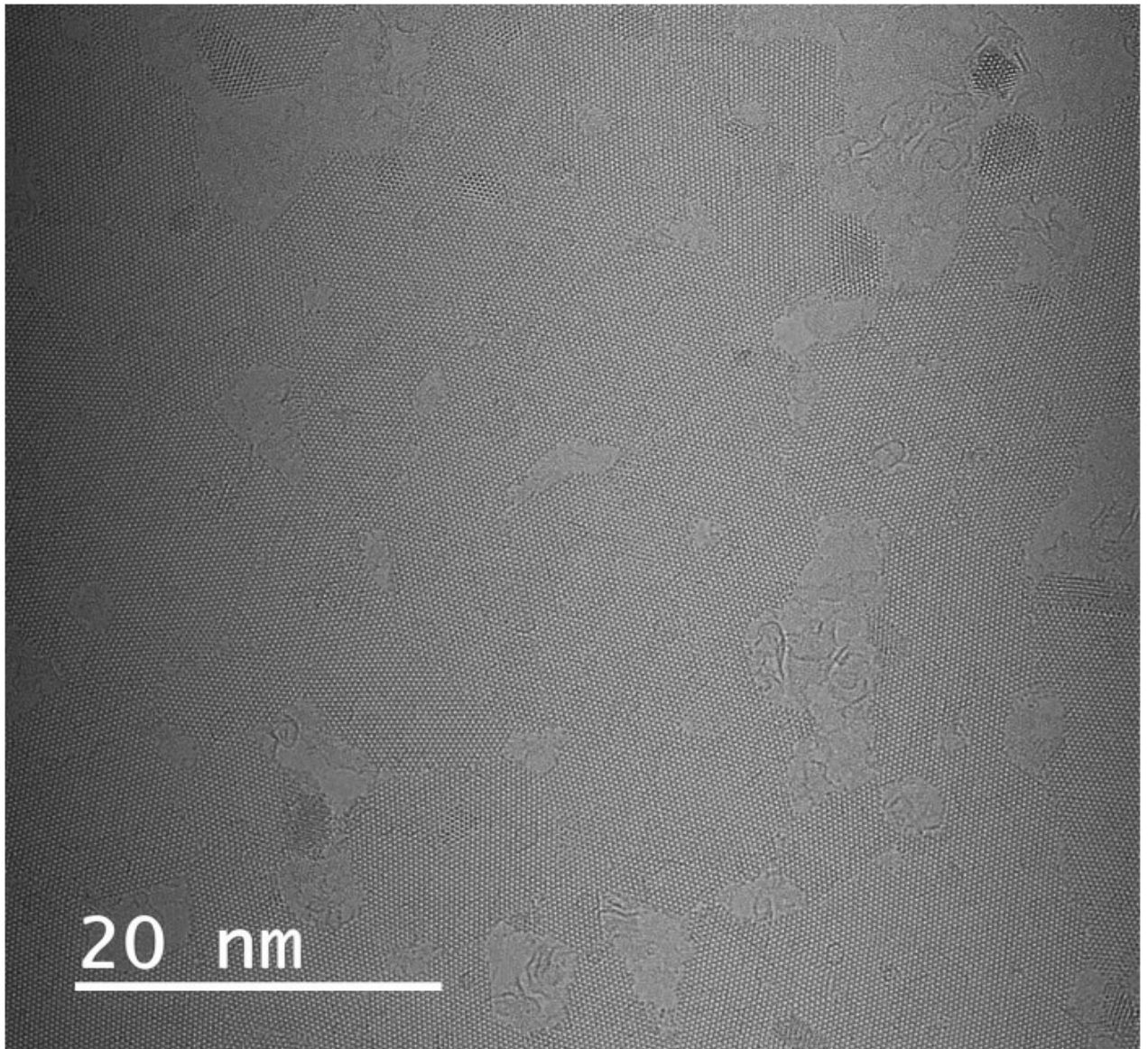


Figure 2.1: In-plane HRTEM image of the MoS<sub>2</sub> deposit obtained after 3 ALD cycles and annealing at 800°C under argon for 30 min [Cadot et al., 2017]

The objective of this thesis is to fabricate Field Effect Transistors (FET) devices based on MoS<sub>2</sub> using photolithography and to identify and study the critical steps involved in this technological process. The long-term goal is to establish a procedure suitable for fabricating functional devices capable of measuring the electrical properties of MoS<sub>2</sub>, specifically mobility and contact resistance between the Ti metal contacts and the MoS<sub>2</sub> film. The workplan to achieve this goal is the following:

1. Design of a suitable FET geometry.
2. Study on the effects of the cleaning procedure on the MoS<sub>2</sub>, using Raman Spectroscopy and Optical Microscopy.
3. Study and optimization of the parameters of the photolithography steps. This step involves the spin-coating of a resist on the MoS<sub>2</sub> samples, the patterning via direct laser writing of the resist and finally the removal of the resist. The effects of different experimental conditions on the MoS<sub>2</sub> are investigated using Raman Spectroscopy and Optical Microscopy.
4. FET fabrication via DC sputtering of Ti and Au over a patterned resist and characterization of the devices at the probe station.
5. Study on the effects of Pulsed Laser Annealing (PLA) to improve the Ti/MoS<sub>2</sub> contact using Raman Spectroscopy and Atomic Force Microscopy (AFM).

A brief description of the fabrication and material characterization techniques employed in this work is reported in this chapter along with the relevant parameters used in the experiments.

## RESIST SPIN COATING

A spin coater machine was used to deposit the resist bilayer on the MoS<sub>2</sub> samples. Spin coating is a widely adopted technique for depositing thin films, known for its simplicity and effectiveness in achieving high uniformity and reproducibility across large surfaces. This technique involves dispensing a liquid solution onto a substrate and spinning it at high speeds, allowing centrifugal force to spread the liquid uniformly across the surface.

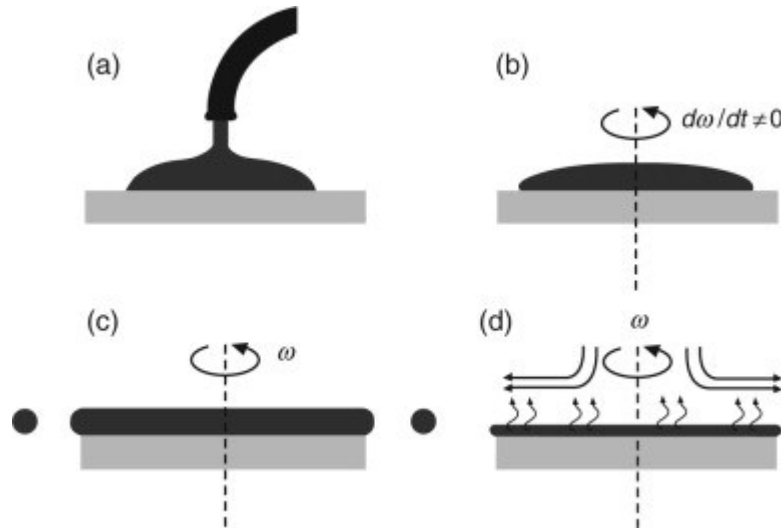


Figure 2.2: Schematic representation of the spin coating process. A drop of solution is deposited on the substrate (a). The substrate spinning velocity increases (b). The substrate spinning velocity is constant (c) so that the solution is distributed uniformly, and the solvent evaporates.

One of the primary advantages of spin coating is the precise control it offers over the film thickness. The thickness of the deposited film is influenced by several parameters, including the rotational speed  $\omega$ , spin duration  $t$ , angular acceleration  $d\omega/dt$  and the viscosity  $\mu$  and density  $\rho$  of the solution. When the effect of viscous flow dominates, the liquid spreads uniformly over the substrate, resulting in a thicker film. In particular, the thickness of the deposited layer can be approximated by the following equation:

$$h(t) = \frac{1}{\omega \sqrt{\frac{4\rho}{3\mu} t}}$$

Conversely, if the evaporation rate of the solvent is the prevailing factor, a thinner film is produced. In addition to these process parameters, post-deposition thermal treatment can further enhance the properties of the coated film. Heating the as-deposited sample can improve the adhesion of the film to the substrate and refine its morphology, leading to better overall performance and stability of the thin film. This step is especially important in applications where uniformity and long-term durability are critical.

In this work to disperse the resist a two-step process was used. In step 1, the resist was distributed uniformly by rotating the substrate at a relatively low rotational speed. In step 2 the rotational speed was increased to achieve a thickness of 1  $\mu\text{m}$ . The baking step was necessary to remove the built in strains in the resist and to reduce the solvent contents

	SF11 LOR (Lift-off resist)	S1813 (Imaging resist)
Step 1	500 rpm for 10 seconds	500 rpm for 10 seconds
Step 2	4000 rpm for 50 seconds	4000 rpm for 50 seconds
Baking step	160 °C for 5 minutes	130 °C for 1 minute

*Table 2.1: Spin-coating and baking parameters used in this work.*

## **OPTICAL LITHOGRAPHY**

Optical lithography is still the most widely used technique to pattern semiconductor materials. This technique is based on the irradiation of a photoresist by UV light. The resist can either be positive or negative, meaning that a developer solution removes either the irradiated or the non-irradiated region, respectively. If a mask is placed between the UV source and the sample, the positive or the negative pattern of the mask is reproduced on the resist after the developing phase. In this work the exposure to UV lights was done using a maskless direct-writing lithography system ( $\mu\text{MLA}$ ) supplied by Heidelberg instruments shown in Fig. 2.2



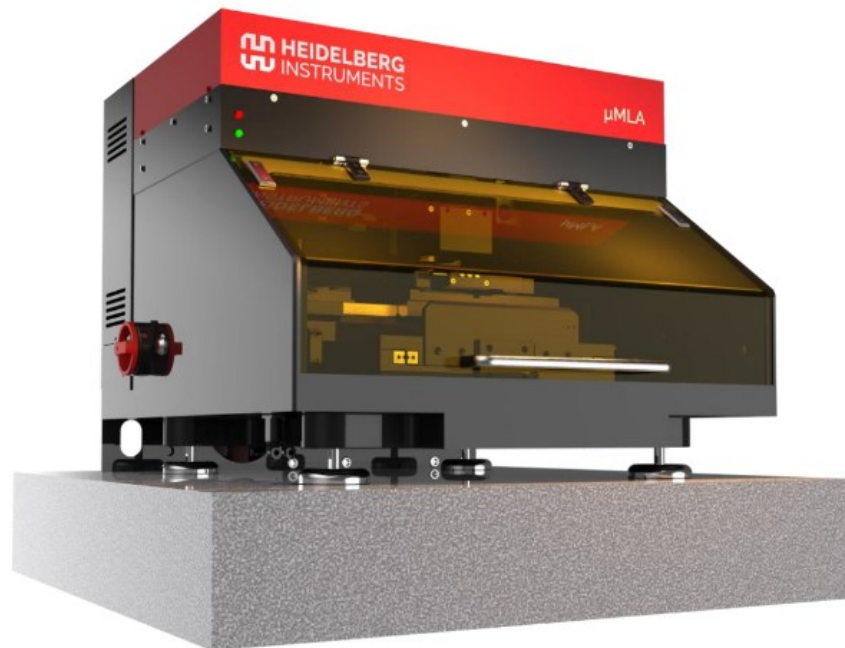


*Figure 2.2: Image of the  $\mu$ MLA direct laser writing lithography machine used in this work.*

The advantage of this system is that it eliminates the need for a physical mask. The workflow of the machine is the following:

1. An AutoCAD file is loaded into the software that controls the  $\mu$ MLA. This AutoCAD file contains the dimensions and shapes of the regions that are then irradiated on the resist.
2. The  $\mu$ MLA irradiated the regions using a grid of UV-LEDs with a wavelength of 365 nm.

After the exposure step the samples are dipped in developing solution that etches the regions of the resist that have been irradiated. More detailed information on this and on the following steps are reported in Chapter 3 paragraph 3.4.1.

## **METAL SPUTTERING**

Direct current (DC) and Radio-frequency (RF) magnetron sputtering are versatile physical vapor deposition (PVD) techniques for fabricating large-area thin films. A diagram of the sputtering setup is shown in Fig. 2.1. The sputtering process involves vaporizing a target material by bombarding it with gaseous plasma molecules, which eject atoms from the

target. These atoms then deposit onto a substrate placed in front of the target. For this thesis, Titanium (Ti) and Gold (Au) films were deposited using Ti and Au targets.

The DC diode sputtering system consists of two planar electrodes: a cold cathode and an anode. The cathode's plasma-facing surface is coated with the target material, while its reverse side is cooled by water. Substrates are placed on the anode. When the sputtering chamber is filled with argon gas at 0.1 Torr and several kilovolts of DC voltage with a series resistance of 1-10 kΩ are applied between the electrodes, a glow discharge is triggered. Argon ions within the discharge are accelerated toward the cathode, sputtering the target material, which leads to the deposition of a thin film on the substrates.

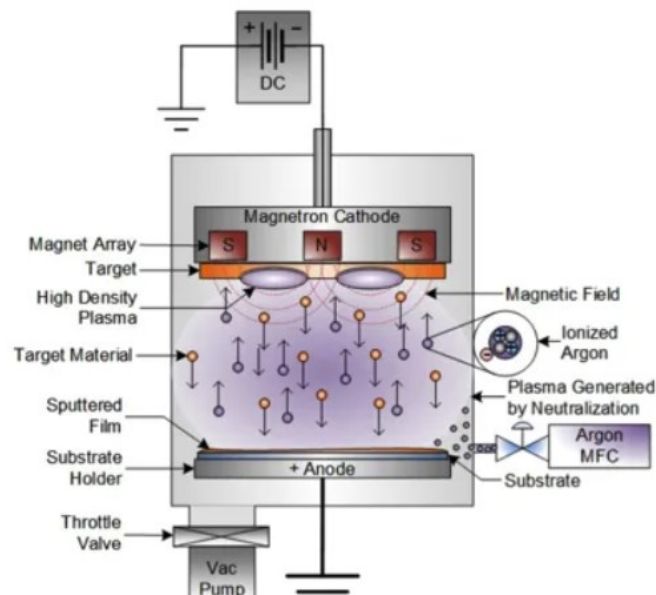


Figure 2.3: Schematic representation of a DC sputtering process [https://www.semicore.com/news/66-planar-magnetron-pvd-coating]

During sputtering, a high-voltage RF source, typically operating at 13.56 MHz, is applied between the anode and cathode to generate and confine the plasma. The plasma is created near a metal electrode positioned behind the sputtering target. The periodic inversion of polarity in the plasma prevents charge accumulation on the target surface, enabling the sputtering of dielectric and insulating materials. In the magnetron configuration, permanent magnets are used to generate a magnetic field that focuses and intensifies the plasma near the target, increasing ion bombardment and enhancing the deposition rate. Argon (Ar), a heavy inert gas, is typically used as the sputtering gas, facilitating high-energy collisions that boost the deposition rate while preventing chemical reactions with the target atoms.

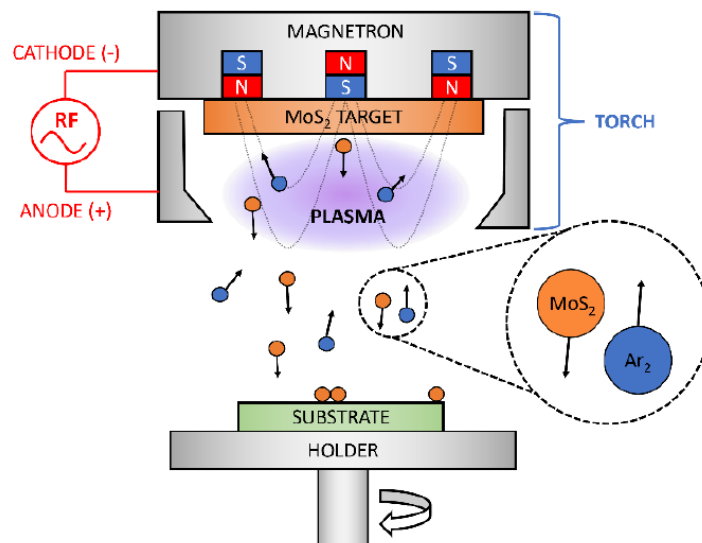
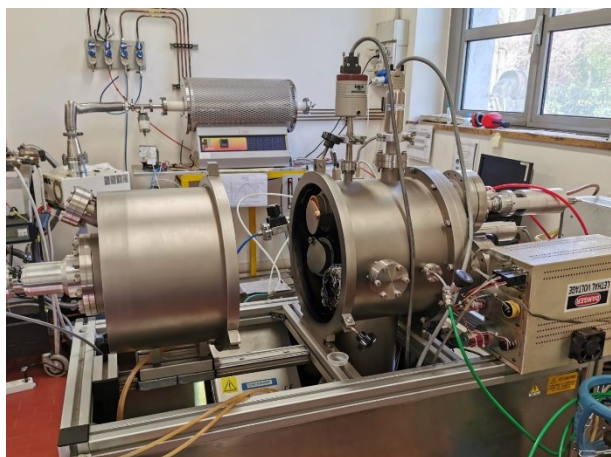


Figure 2.4: Schematic representation of a DC sputtering process.

The experimental procedure consisted in pumping the chamber pressure down to about  $1 \times 10^{-6}$  mBar. Then a chamber working pressure of  $5 \times 10^{-3}$  mBar was reached through high-purity Ar<sub>2</sub> gas injection and maintain in a dynamic vacuum regime with a gas flow of about 12.7 sccm. In the case of deposition of only Ti films, only the use of DC torch was required. This torch was operated with an applied power of 20 W. The torch shutter was kept close for at least 1 minute to clean the surface of the target (i.e. pre-sputtering step). Once the shutter was opened the sputtering process lasted for 30 s. This time was determined through calibration deposition in order to achieve a Ti film of about 3 nm thickness. At the end of the deposition the shutter was closed while the torch was switched off. The chamber was then filled with with Ar<sub>2</sub> gas until reaching ambient pressure in order to retrieve the samples. The deposition of both Ti and Au metals required instead the use of two torches due to the instrument configuration, one DC-torch and one RF-torch. First, the Ti deposition was performed following the same steps reported in the previous paragraph. The sample was then moved in front of the Au target mounted on the RF torch. The operative power applied was set to 30 W. The DC-torch with Ti target was switched on with a power of about 10 W in order to trigger the RF torch ignition and then it was immediately switched off. The Au deposition was calibrated to reach a thickness of about 100 nm.



*Figure 2.5: Image of the sputtering system used in this thesis.*

## **LASER PROCESSING**

The thermal annealing of MoS<sub>2</sub> was carried out using a Coherent COMPex 201 KrF excimer laser. This pulsed gas laser operates with a mixture of krypton (Kr), fluorine (F<sub>2</sub>), and neon (Ne) as the active medium within a plane-parallel optical resonator. The laser is excited by a high voltage discharge (18-27 kV), which generates KrF excimers. When these excimers dissociate into their elemental components, they release a single UV pulse (248 nm) with a duration of 22 nanoseconds.

A diagram of the laser beam delivery system is shown in Fig. 2.6. The energy of the laser pulses can be adjusted by a motorized attenuation system with dual mirrors positioned immediately after the laser. The pulses are then directed through a beam delivery system, which includes a series of lenses (L) and mirrors (M). The laser beam's Gaussian intensity profile is transformed into a highly uniform beam by a homogenizer array (HA) composed of  $9 \times 9$  lenses, producing a square beam with dimensions of  $5 \times 5 \text{ mm}^2$  and spatial energy variations of less than 2%. A diode inline detector, with the help of a beam splitter (BS), measures part of the output and adjusts the attenuator accordingly. The beam is cropped by a mask and focused onto the sample, striking it vertically as it rests on a horizontally adjustable holder. The energy density (ED) delivered to the sample can be adjusted between approximately 40 and 1200 mJ/cm<sup>2</sup>. However, as the gas mixture deteriorates over time, periodic refilling is required to prevent significant power reduction. Although the laser can operate at a repetition rate of 10 Hz, all multi-pulse thermal treatments in this study were conducted at a repetition rate of 1 Hz. A constant flow of nitrogen (10 L/min) was directed onto the sample to minimize the presence of oxygen on its surface.

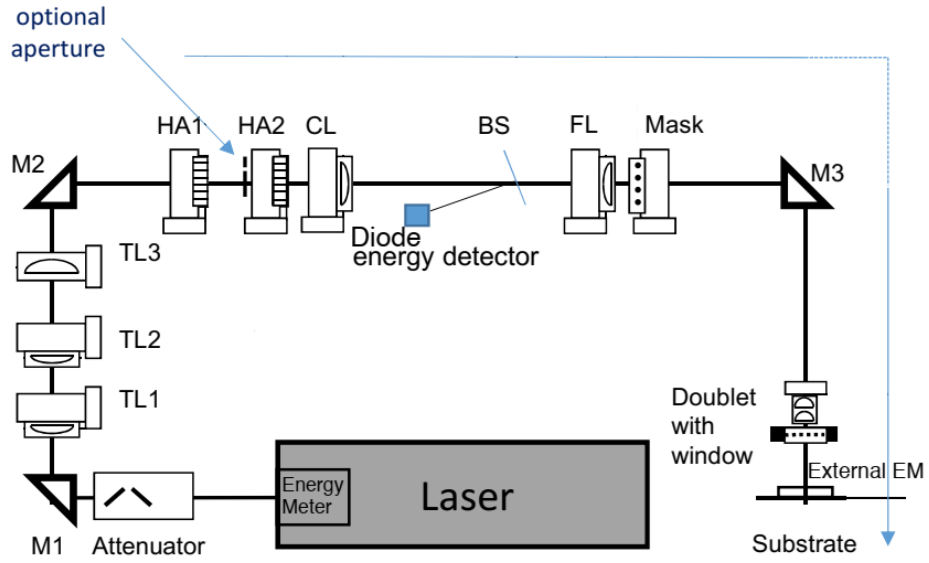


Figure 2.6: Schematic representation of the laser beam delivery unit.

## RAMAN SPECTROSCOPY

In this work Raman spectroscopy was employed to assess the degradation of the MoS<sub>2</sub> after each step of the photolithographic and pulsed laser annealing process.

The underlying phenomenon that makes Raman spectroscopy possible is the interaction between monochromatic light and the lattice vibrational modes of the material. Specifically, when the radiation impinges on the sample, different scattering phenomena take place. The predominant effect is the Rayleigh scattering, an elastic process by which the energy of the outgoing photon remains unaltered. Instead, the other scattering process involves the excitation of a vibrational mode of the lattice that leads to a slight decrease in the energy of the emerging photon. Because of the different cross sections of the two processes, the fraction of photons subject to Raman scattering is the 10<sup>-7</sup> %. Therefore, an appropriate Raman spectrometer is needed to detect these photons.

In this work the *XploRA plus – Horiba microRaman* spectrometer was used to collect the spectra. A schematic layout of the setup is shown in Figure 2.7. The source of the exciting radiation is a solid-state laser. The laser beam is focused on the sample through objective lenses. The backscattered radiation is then collected by these same lenses and directed towards a diffraction grating that disperses the light with different wavelengths onto a CCD position-sensitive detector. Finally, this device measures the intensity of each component of

the radiation. In addition, the lenses collect the image of the surface-sample that is recorded by a camera.

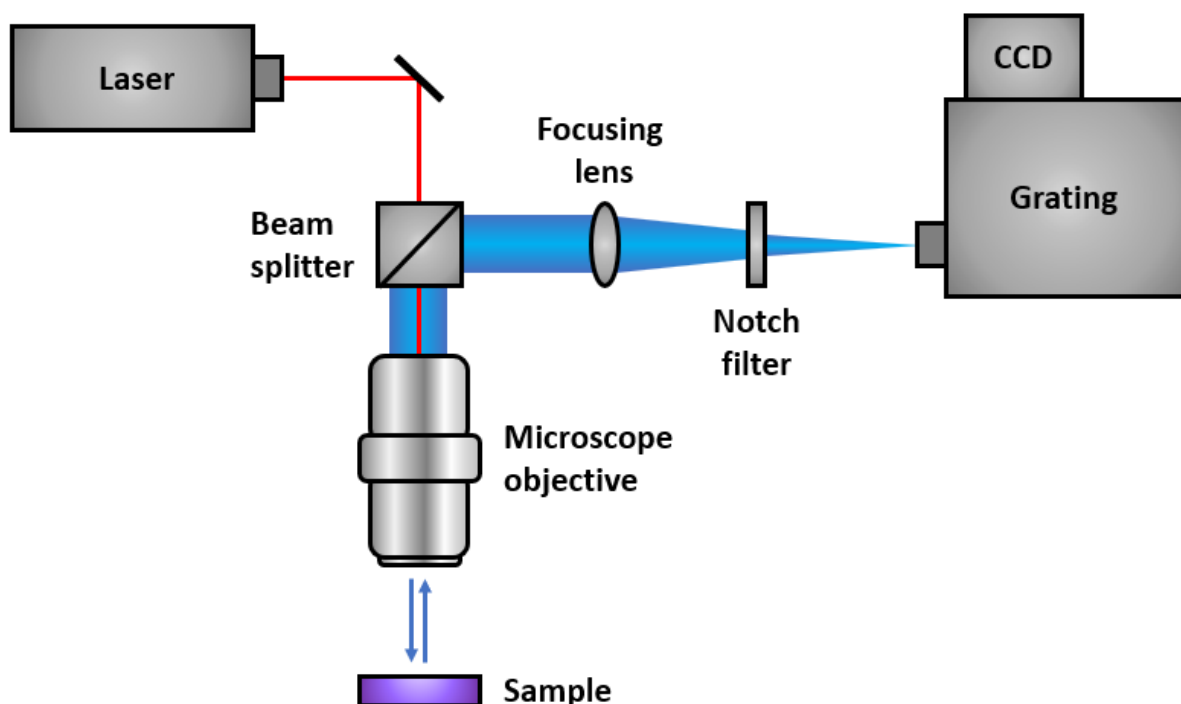


Figure 2.7: Schematic representation of the Raman confocal microscope.

For this research, the excitation wavelength was set to 532 nm. The nominal laser power of 100 mW was reduced with filters during the focusing and measurement steps to avoid heating and therefore possible damage of the sample. In particular, the focusing was carried out with the laser intensity reduced to 0,1%, while the spectra were collected with a 1% filter to increase the signal intensity. The focusing was done by manually adjusting the distance between the 100x objective lens and the sample holder until the laser spot size was minimized to 1.0  $\mu\text{m}$ . Finally, each Raman spectrum was acquired in the -10 to 1000  $\text{cm}^{-1}$  range resulting from an average of 10 exposures and an integration time of 10 s.

## AFM

Atomic Force Microscopy (AFM) enables the imaging of a sample's surface morphology on a micrometer scale, achieving a vertical resolution of approximately 50 pm. A comprehensive overview of AFM-based techniques and their operating methods can be found in reference [Mironov, 2004]. In this thesis, the surface morphology changes of  $\text{MoS}_2$  and Ti/MoS thin

films following laser annealing were investigated using a Nanosurf FlexAFM microscope in "semi-contact" mode, also known as "tapping" mode. A schematic of the instrument's main components is shown in Fig. 2.11. AFM imaging is based on the interaction between a V-shaped tip attached to a flexible cantilever and the sample surface. The probes used in this research were Multi75E-G, provided by Nanosensor, which are standard high-resolution AFM probes for non-contact mode. Each probe features a pyramidal tip with a curvature radius of less than 25 nm, mounted on a cantilever measuring 225  $\mu\text{m}$  in length and 28  $\mu\text{m}$  in width. The cantilever has a nominal force constant of 3 N/m and a nominal free resonant frequency of about 75 kHz. The cantilever's reflective coating is made up of a 5 nm thick layer of Chromium and 25 nm thick layer of platinum on both sides, which enhances the reflectivity of the laser beam. Further details on the probes can be found on the official supplier's website [<https://www.nanoandmore.com/AFM-Probe-ElectriMulti75>].

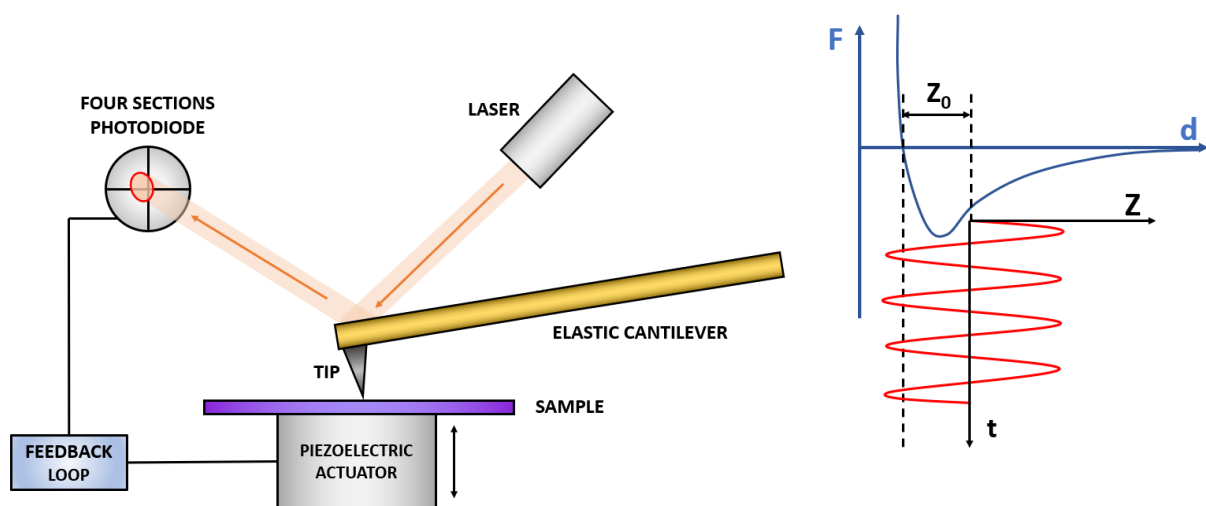


Figure 2.8: (left) Scheme of the NanoSurf FlexAFM atomic force microscope (AFM); (right): Total force acting on the tip  $F$  as function of the distance between the tip and the surface of the sample  $z$  (blue); oscillations of the tip  $z$  as function of time  $t$  (red).

In the AFM setup, a laser beam reflects off the edge of the cantilever and onto the center of a four-segment detector. This detector measures the cantilever's bending and torsion, which are caused by attractive or repulsive forces between the tip and the sample surface. These forces result in a displacement of the laser beam from the center of the photodetector. During sample scanning, variations in the photodetector signal, compared to the reference signal (which corresponds to no interaction between the tip and the sample), serve as the primary feedback parameter, generating what is known as the "error signal." This signal is sent to a

piezoelectric actuator, which controls the sample's position, to correct any cantilever deflections from their initial settings.

Scanning can be conducted in a quasi-static regime, where the tip remains in direct contact with the surface, known as "contact mode." In this mode, a low-stiffness cantilever is used to minimize the impact of the tip on the surface. However, direct mechanical contact can damage both the sample surface and the tip, leading to significant imaging artifacts. For MoS<sub>2</sub> thin films, contact mode is unsuitable due to the weak bonding caused by van der Waals interactions.

Instead, this thesis uses "semi-contact mode" (also called "tapping mode") to image the morphology of MoS<sub>2</sub> thin films. In this mode, the cantilever is excited in order to oscillate at its resonant frequency ( $f_{\text{res}}$ ) and interacts repulsively with the sample surface only during a small portion of the lower half of each oscillation cycle (Fig. 2.8). If  $z_0$  is the distance the tip travels from its equilibrium position to the surface, semi-contact mode occurs only when  $z_0$  is less than the amplitude of the cantilever's free oscillations. In this regime, the van der Waals force gradient causes shifts in the cantilever's amplitude and phase responses relative to the free oscillation amplitude and frequency ( $f_{\text{res}}$ ). The feedback system ensures a constant oscillation amplitude by adjusting the piezoelectric actuator to maintain a steady distance between the tip and the sample. This feedback signal is then used to generate a topographic map of the sample.

## **ELECTRICAL CHARACTERIZATION**

The FET prototypes fabricated during this thesis were tested using a probe station located in the cleanroom of the Physics Department, operated with a Keithley Source Measure Unit (SMU). The probe station (Fig. 2.9) features several metallic probes connected to micrometric manipulators, enabling a gentle and precise approach to the FET electrical contacts, as well as allowing lateral precision movements. The sample is positioned on a metallic plate that can be adjusted vertically with micrometer precision. An optical microscope is used to observe the sample and guide the placement of the probes. The entire probe station is housed in a Faraday cage, which shields the sample from external light. The SMU is directly connected to the probes and is designed to supply or measure voltage differences and currents. The high precision of the SMU in current measurements (down to 0.1 nA) is crucial for testing the FET response when voltage differences in the range of volts or tens of volts are applied between the source and drain.



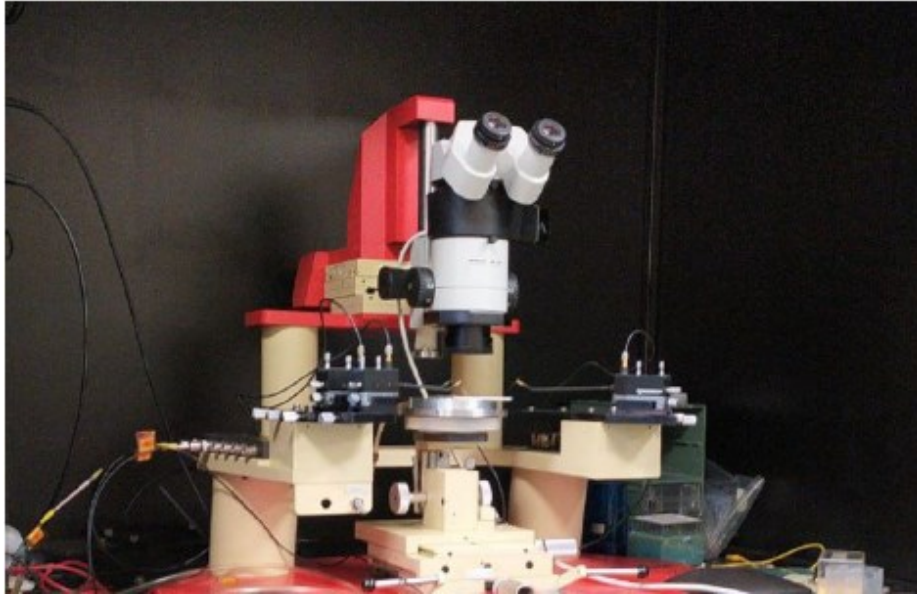


*Figure 2.9: The probe station used to test the FET devices.*

A schematic of the electrical contacts made using the probe station is shown in Fig. 2.10. Two probes were used to establish the source and drain contacts on a single FET, while a third probe was connected to the back-gate contact. The current,  $i_{DS}$ , was measured as a function of the applied voltage,  $V_{DS}$  with a fixed gate-source voltage,  $V_{GS}$ . This gate-source voltage must be limited to avoid damaging the oxide film. It is well known that  $\text{SiO}_2$  thin films reach irreversible breakdown at an electric field strength of approximately 2.7 V/nm, where impact ionization and accelerated electrons lead to the destruction of Si–O bonds [Usui et al., 2013]. Since the oxide layer is 500 nm thick, in principle, more than 1300 V can be applied before oxide breakdown occurs.

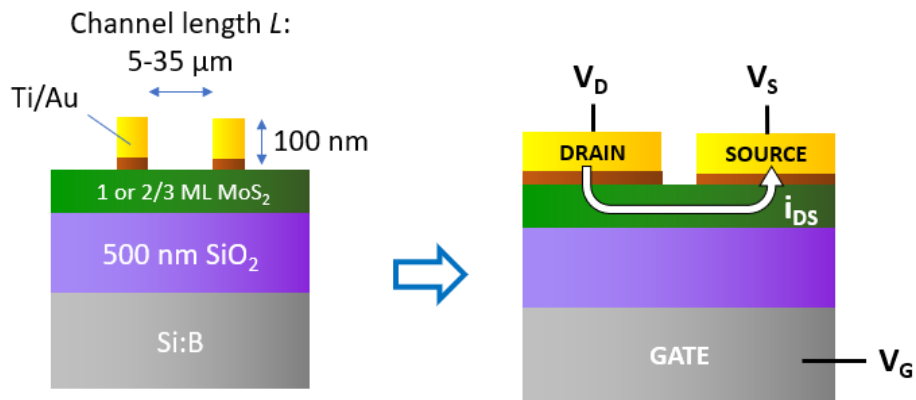


Figure 2.10: (left) Scheme of a FET structure. (right) Scheme of the FET electrical contacts.

# CHAPTER 3: RESULTS

## 3.1 INTRODUCTION

The experimental results obtained during this thesis (i.e. optimization of FET fabrication processes, material characterization, electrical measurements) are reported and discussed in this chapter. This includes all the steps from the design of a suitable FET geometry to the optimization of the photolithography parameters (dose, developing time), to the liftoff optimization. In particular, the impact of each FET fabrication step on the underlying MoS<sub>2</sub> is studied by means of optical microscopy and Raman spectroscopy. At the end of this first section the electrical characterization results are reported. Lastly, to improving the metal-MoS<sub>2</sub> contact resistance, an exploratory study is conducted to investigate the effect of PLA on the metal-MoS<sub>2</sub> contact. The results obtained in this preliminary work might then be transferred to FET metal-MoS<sub>2</sub> contact processing and verify an improvement in the contact resistance

## 3.2 FET DESIGN

First, a suitable configuration for the FET devices was chosen. Because the structure of the sample consisted of a continuous layer of MoS<sub>2</sub> on a 500 nm thick SiO<sub>2</sub>-on-Si substrate a backgated geometry was deemed more suitable. In this way, 500 nm thick SiO<sub>2</sub> layer acts as a gate oxide (Fig. 3.1 a). Second, the source and drain electrodes were designed using the AutoCAD software. This design adopted is reported in Fig. 3.1 b

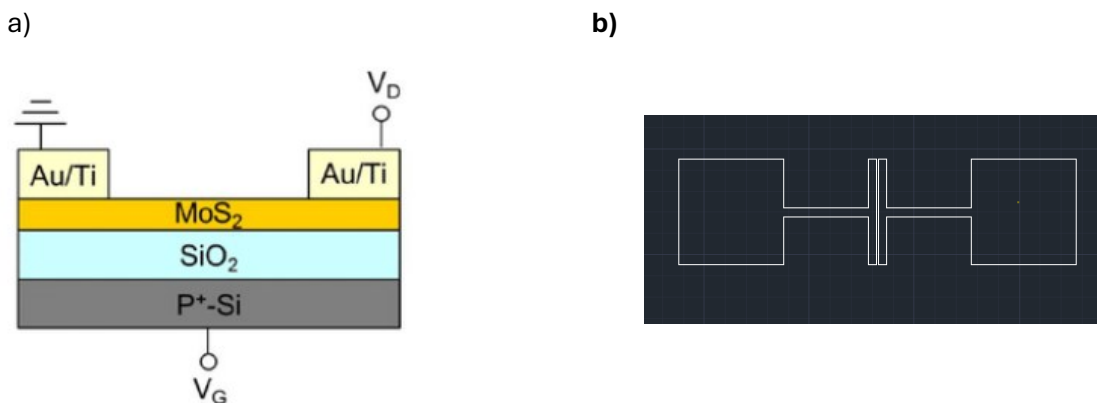


*Figure 3.1: (a) Schematic representation of a FET backgated geometry. (b) Design chosen for the FET used in this work. The dimensions of the square pads are 250  $\mu\text{m}$  x 250  $\mu\text{m}$ , those of the horizontal rectangular parts are 200  $\mu\text{m}$  x 20  $\mu\text{m}$ , finally the dimensions of the vertical rectangular parts are 20  $\mu\text{m}$  x 250  $\mu\text{m}$ .*

The reason behind this geometry is to ensure a large enough contact area between the tip of the probe station and the two electrodes. Furthermore, the channel lengths were maintained below 35  $\mu\text{m}$  to keep a higher density of field lines inside the channel.

## 3.4 STUDY OF THE PHOTOLITHOGRAPHY PROCESS

### 3.4.1 Substrate preparation

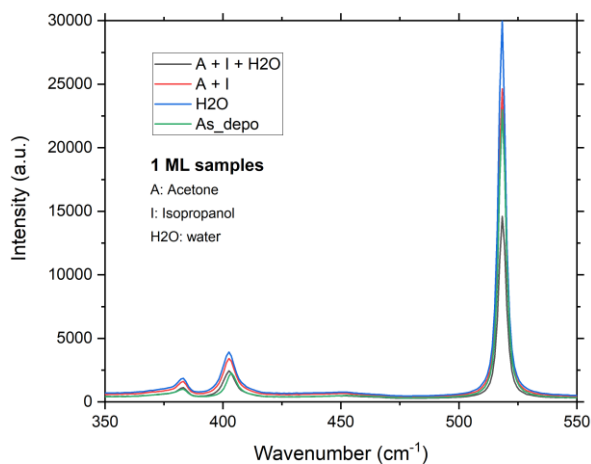
A preliminary study has been performed to investigate the effect of different solvents on the 1 and 2/3 ML MoS<sub>2</sub> samples. Their effect was evaluated using Optical Microscopy and Raman Spectroscopy. The solvents used were acetone, isopropanol and water. In particular, the combinations used were acetone, isopropanol and water, acetone and isopropanol, and water. The samples were cleaned by dipping the samples in the solvents for the following amounts of time:

- Acetone for 30 seconds, isopropanol for 30 seconds and water for 30 seconds
- Acetone for 45 seconds, isopropanol for 45 seconds
- Water for 90 seconds.

Then, Raman spectra were acquired to confirm that the MoS<sub>2</sub> crystalline quality remained intact throughout the process. Each sample was observed using the optical microscope of the Raman spectrometer, before acquiring the spectra. It was found that the MoS<sub>2</sub> film delaminated on the sample treated with only water (Fig. 3.4). Therefore, Raman spectra were acquired on the regions where MoS<sub>2</sub> was still present. Representative spectra for 1 ML and 2-3 ML films are reported in Fig. 3.2a and Fig. 3.2b, respectively. The selected spectral window shows three main peaks, two of which correspond to the MoS<sub>2</sub> crystalline film. The E<sup>1</sup><sub>2g</sub> peak, which is positioned at 383 cm<sup>-1</sup> for the 1 ML film and 382 cm<sup>-1</sup> for the 2-3 ML film, corresponds to the in-plane vibrational mode. The out-of-plane A<sup>1</sup><sub>1g</sub> mode is observed at around 404 cm<sup>-1</sup> for the 1 ML film and 406 cm<sup>-1</sup> for the 2-3 ML film. These results are consistent with the number of layers present in each film [Li et al., 2012]. The final peak, observed around 521 cm<sup>-1</sup>, is associated with the silicon substrate. This Si peak is significant because it serves as a reference for normalizing the MoS<sub>2</sub> signal, allowing for quantitative analysis from Raman spectroscopy [Li et al., 2012]. The average values of the normalized

MoS<sub>2</sub> A<sub>1g</sub> Raman peaks for the 1 ML and 2-3 ML films are shown in Fig. 3.3a and Fig. 3.3b, respectively.

a)



b)

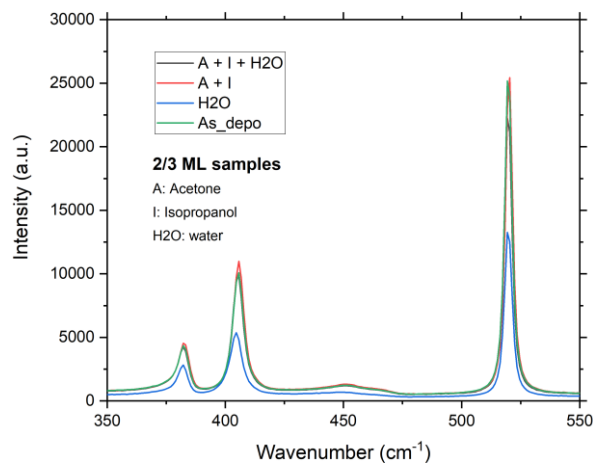
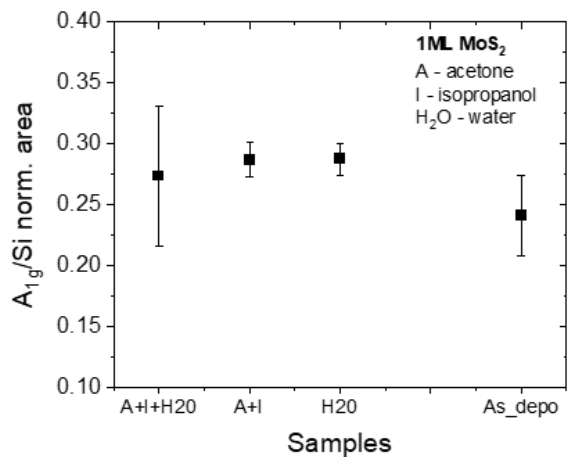


Figure 3.2: Raman spectra acquired on (a) 1 ML MoS<sub>2</sub> samples and (b) 2/3 ML MoS<sub>2</sub> samples subjected to different cleaning solvent

a)



b)

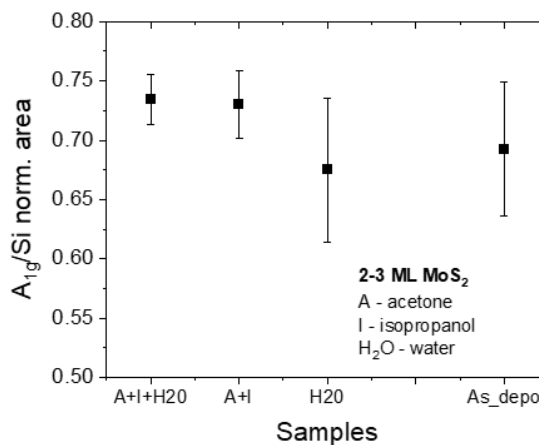


Figure 3.3: Normalized intensity of the A<sub>1g</sub> MoS<sub>2</sub> peaks of (a) 1 ML MoS<sub>2</sub> samples and (b) 2/3 ML MoS<sub>2</sub> samples subjected to different cleaning solvent. For each sample five spectra were acquired. The reported values are the averages of the five normalized intensities.



*Figure 3.4: 1 ML sample treated with water only.*

Figures 3.3 and 3.2 show that no solvent leads to a degradation of the Raman signal. However, Fig. 3.4 shows that water leads to the delamination of the MoS<sub>2</sub> films in both 1 ML and 2/3 ML samples. It is therefore clear that the best solvents to perform the cleaning steps are organic ones like acetone and isopropanol.

### **3.4.2 Overview of the main photolithography steps**

A comprehensive flow of all the steps involved in the photolithography process necessary to build the FETs is reported in Fig. 3.5, while the composition of the chemicals involved is reported in Fig. 3.6

Step 1 consists in the spin coating and soft baking of the liftoff resist (LOR). The use of an LOR is necessary because this polymer is etched more rapidly than the overlaying photoresist [Conde-Rubio et al., 2022]. In this way, the metal film that is subsequently deposited on the substrate does not come into contact with the resist layer, avoiding the delamination of the metal during the liftoff phase.

Step 2 consists in the spin coating and baking of the S1813 imaging resist. For both the resists the baking step is necessary because right after the coating the resist film contains 20 % to 40 % solvent by weight. If the resist film is not baked it loses solvent gradually by evaporation, thus changing the properties of the film during time. The baking step removes the excess solvent, and the film becomes stable at room temperature. This leads to a

reduced thickness, an improved adhesion. Also, the film becomes less tacky therefore it is less susceptible to particle contamination.

Step 3 consists in the exposure of the sample under UV light in the  $\mu$ MLA machine. This causes a Wolff-rearrangement process leading to the final formation of a carboxylic acid. The regions irradiated with UV-light are therefore soluble in the alkaline solution provided by the developer. It is of critical importance to choose an appropriate energy density of the impinging radiation, to avoid proximity effects that enlarge the patterns on the mask.

In step 4 the sample is dipped in the developing solution of Tetra-methyl-ammonium-hydroxide. This solution dissolves over time the irradiated regions of the resist layer. An important parameter in this step is the time the sample stays in contact with the solution, indeed if it is too short the patterns are not fully developed.

Finally, after the metal deposition (step 5) the resist bilayer is removed using the PG Remover, a solution based on the N-methyl-2-pyrrolidone in which the LOR resist is soluble. This last step is particularly critical because delamination of the underlying  $\text{MoS}_2$  film might happen together with the removal of the resist bilayer.

Figure 4: LOR/PMGI Process Flow



1. Coat and soft-bake LOR or PMGI.



2. Coat and soft-bake imaging resist.



3. Expose imaging resist.



4. Develop resist and LOR or PMGI. LOR or PMGI develops isotropically, creating a bi-layer re-entrant sidewall profile.



5. Deposit film. The re-entrant profile ensures discontinuous film deposition.



6. Lift off bi-layer resist stack, leaving only desired film.

Figure 3.5: Schematic representation of each lithography step

<p>LOR (SF11) Based on a polyaliphatic imide copolymer</p>	
--	--



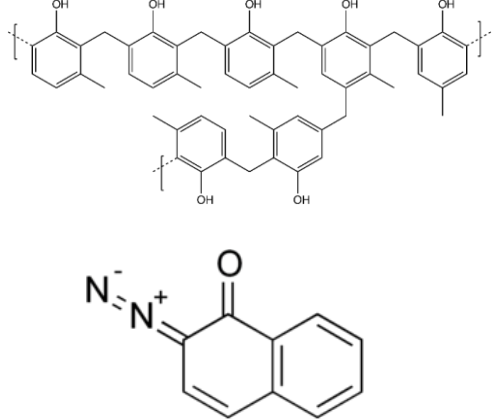
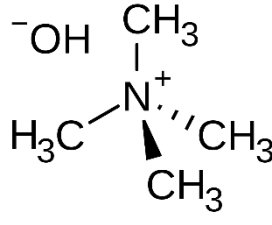
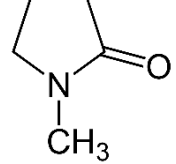
<p>S1813 imaging resist</p> <p>Based on a cresol – novolac polymer.</p> <p>Diazonaphtoquinone is the photosensitive molecule</p>	 <p>The image shows the chemical structure of a cresol-novolac polymer, which consists of a chain of benzene rings connected by methylene bridges, with hydroxyl groups attached to the rings. Below it is the structure of diazonaphtoquinone, a naphthalene ring system with a diazo group and a carbonyl group.</p>
<p>Developer</p> <p>Tetramethylammonium hydroxyde</p>	 <p>The image shows the chemical structure of Tetramethylammonium hydroxyde, which is a central nitrogen atom with a positive charge, bonded to four methyl groups and one hydroxide ion.</p>
<p>Remover</p> <p>1-methyl-2-pyrrolidone</p>	 <p>The image shows the chemical structure of 1-methyl-2-pyrrolidone, which is a five-membered ring containing a nitrogen atom and a carbonyl group, with a methyl group attached to the nitrogen.</p>

Figure 3.6: Chemicals involved in the photolithography process.

### 3.4.3 LOR baking and liftoff temperature optimization

The initial trials aimed at investigating the effect of the liftoff on the underlying MoS<sub>2</sub> layers were done, after baking the LOR at 180 °C for 5 min and performing the liftoff at 100 °C on a 1 ML MoS<sub>2</sub> sample. The pattern used is reported in Fig. 3.7.



*Figure 3.7: Pattern used in the study of the effect of the photolithography process on the MoS<sub>2</sub> samples. The square pads are 250 μm x 250 μm separated. Each column is made up of couples of pads distanced by 80-70-60-50-40-30-25-20-15-10-5-4-3-2-1 μm.*

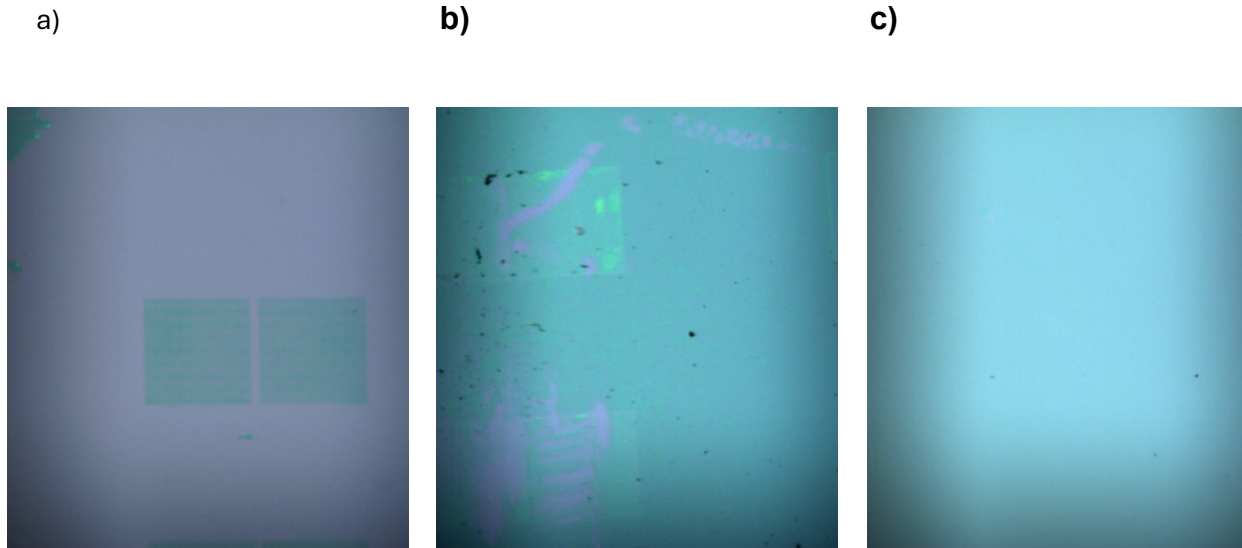


*Figure 3.8: Images acquired using optical microscopy of different 1 ML MoS<sub>2</sub> substrates after (a) Soft-baking at 180 °C and lift-off at 100 °C. (b) Soft-baking at 180 °C and lift-off at 180 °C. (c) Soft-baking at 160 °C and lift-off at 160 °C.*

The liftoff with the initial conditions of 180 °C of soft-baking and 100 °C of lift-off led to the delamination of the 1 ML MoS<sub>2</sub> film (Fig. 3.8a). It was proposed that the polymer's dissolution mechanism led to the delamination of this effect. When the solvent contacts the polymer, solvent molecules penetrate its structure, introducing stress to the polymer [Beth A. Miller-Chou et al. 2003]. If the polymer is below its glass transition temperature, approximately 190°C for LOR, the polymer cannot absorb this stress, leading to the formation of cracks and causing small polymer fragments to erupt from the surface. This process is likely to damage the underlying MoS<sub>2</sub> layer. To address this, the sample with resist was heated to 180°C, and liftoff was performed at the same temperature. As shown in Fig. 3.8b, this resulted in significantly reduced delamination. To minimize the effect further, the baking temperature was lowered to 160°C, leaving some solvent in the polymer structure and making it less rigid. Ultimately, a liftoff at 160°C was sufficient to prevent damage to the MoS<sub>2</sub> layer, as illustrated in Fig. 3.8c.

Raman spectroscopy was conducted to confirm that the MoS<sub>2</sub> crystalline quality remained intact throughout the process, with the results presented in Fig. 3.9.

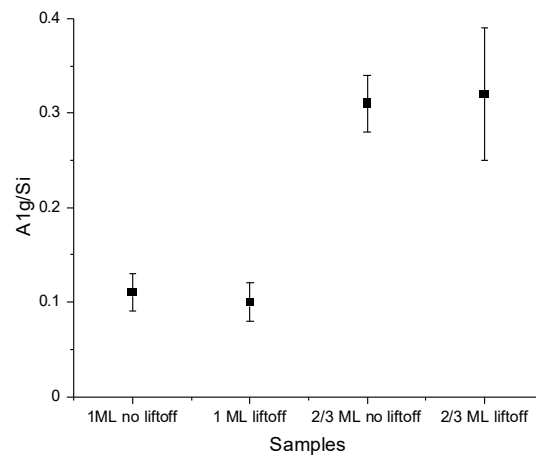


Figure 3.9: Normalized intensity of the  $A_{1g}$  peak of the unprocessed samples (no-liftoff) and of the unprocessed samples (liftoff).

The graph shows that the normalized intensity of the  $A_{1g}$  peak does not vary with respect to the untreated sample.

### 3.4.4 Dose and developing time optimization

After determining the best baking and liftoff conditions, the optimal dose and developing time was determined by patterning the design reported in Fig. 3.10 This design consists in couples of pads of  $25\ \mu\text{m} \times 100\ \mu\text{m}$  distanced by a  $5 - 4 - 3 - 2 - 1\ \mu\text{m}$  channels, to verify whether the proximity effect under different parameters led to the collapse of the channel. On each sample the pattern was replicated using doses of  $50 - 75 - 100 - 125 - 150 - 175 - 200\ \text{mJ}/\text{cm}^2$  as seen in Figure 3.11

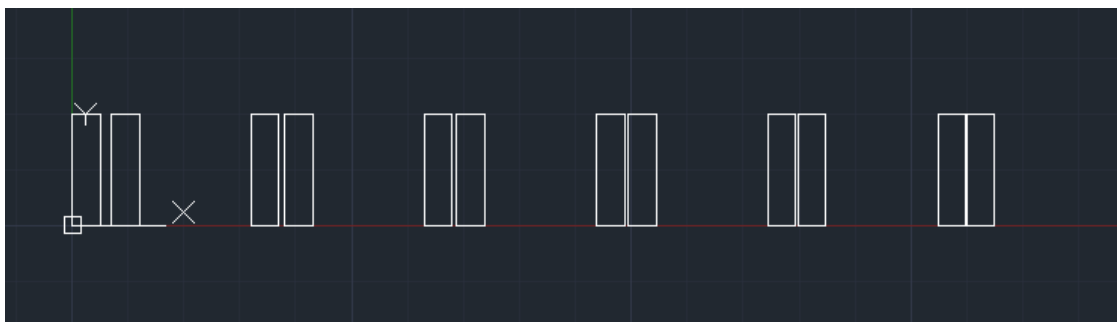


Figure 3.10: Design used to determine the optimal dose and developing time

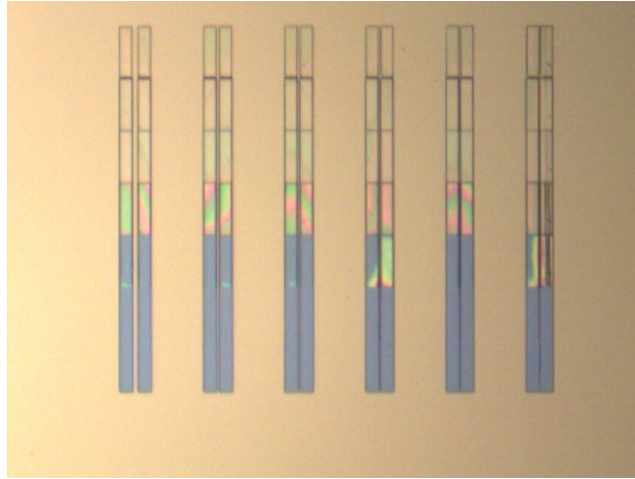
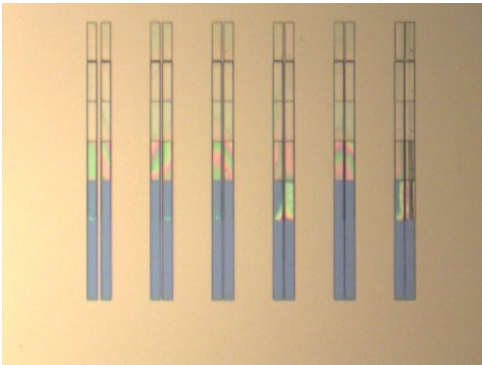
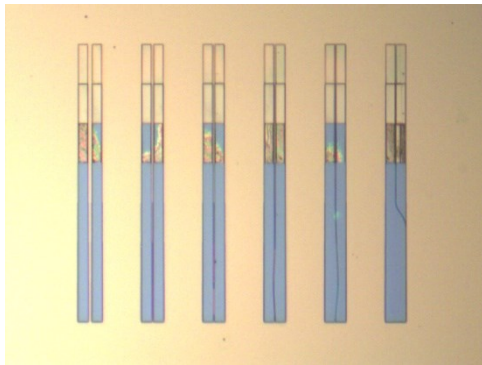


Figure 3.11: Example of a sample after the developing step. Each row was obtained using a different dose. Beginning with the top row, the doses applied were 50 – 75 – 100 – 125 – 150 – 200 mJ/cm<sup>2</sup>.

Four different samples were prepared, and they were developed for 60 - 90 - 120 - 150 s respectively. Figure 3.12 shows images of the patterned samples after different developing times.

60 s	90 s
	
120 s	150 s

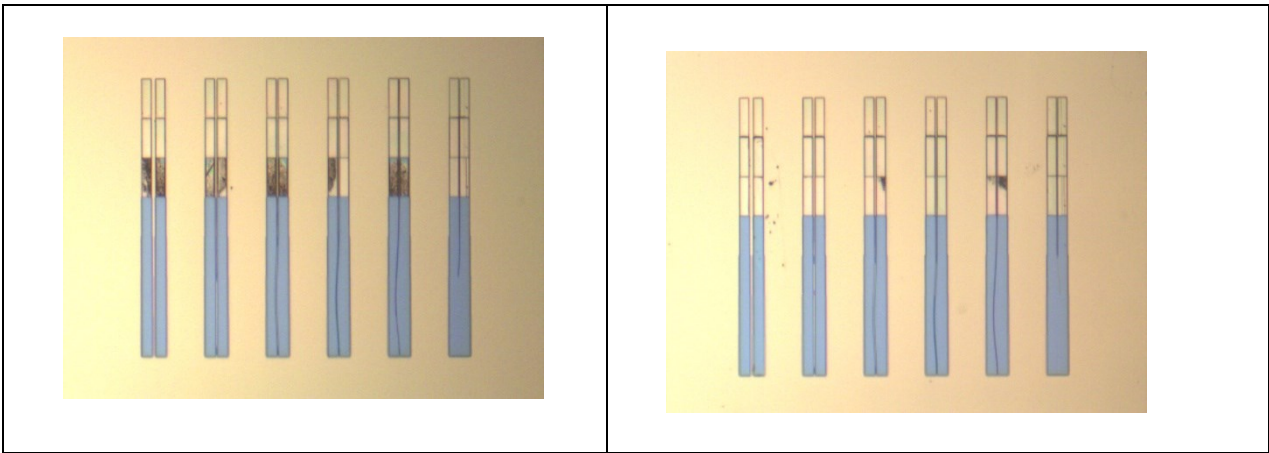


Figure 3.12: Images of the patterned samples obtained via optical microscopy after 60 – 90 - 120 – 150 s.

No complete developing happens for doses under  $125 \text{ mJ/cm}^2$  at any developing time. For doses over  $125 \text{ mJ/cm}^2$  at 90 s or more developing time it is seen that the  $1 \mu\text{m}$  channel collapses due to the proximity effect, and only the one of the  $125 \text{ mJ/cm}^2$  survives. At 60 s and  $200 \text{ mJ/cm}^2$  the  $1 \mu\text{m}$  channel is thinner than the one at  $175 \text{ mJ/cm}^2$ . Following these considerations, it is evident that the best conditions are either  $175 \text{ mJ/cm}^2$  at 60 s or  $125 \text{ mJ/cm}^2$  at 90 s. Therefore, the profilometer was employed to measure the thickness of the resist layer over the  $1 \mu\text{m}$  channel. The results are reported in Fig. 3.12 a and b

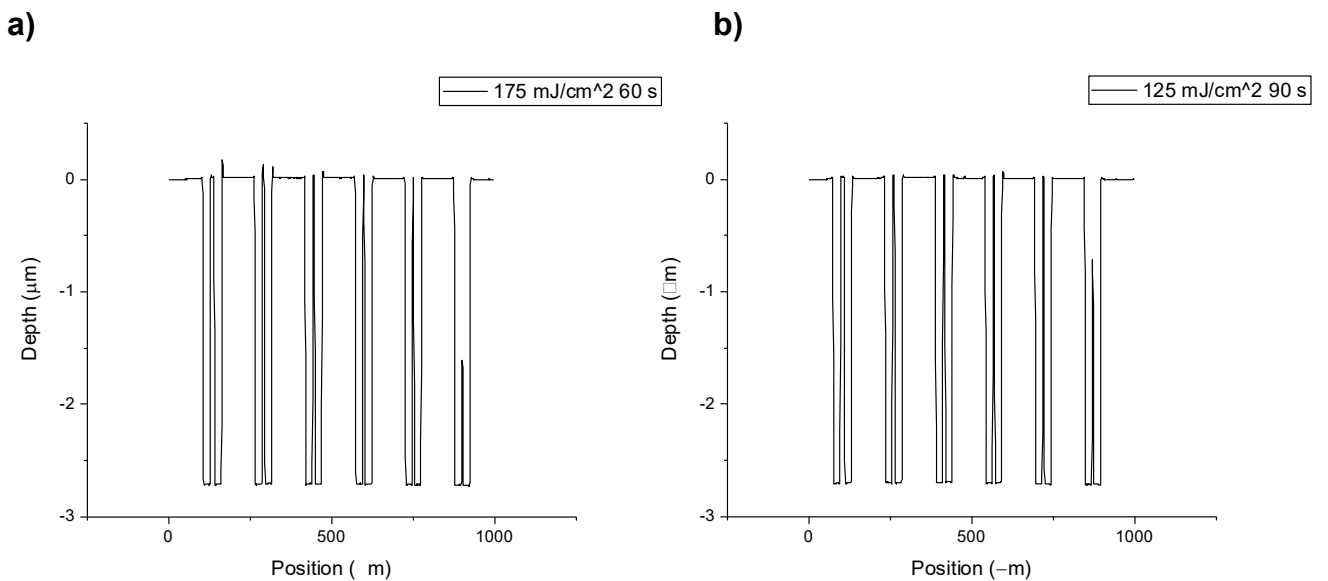


Figure 3.12: (a) Profile of the  $175 \text{ mJ/cm}^2$  row developed for 60 s. (b) Profile of the  $125 \text{ mJ/cm}^2$  row developed for 90 s.

The resist over the 1  $\mu\text{m}$  channel was better conserved with a dose of 125  $\text{mJ}/\text{cm}^2$  and a developing time of 90 s. From then on, the exposure step was performed using these parameters.

## 3.5 FET FABRICATION AND ELECTRICAL MEASUREMENTS

### 3.5.1 FET fabrication

Once the study on the various photolithography steps was complete, masks were fabricated with patterns reported in section 3.2, on six different samples, 3 with 1 ML  $\text{MoS}_2$ , and 3 with 2/3 ML  $\text{MoS}_2$ . It was decided to design a grid of FETs with each column containing the channels of 5 – 10 – 15 – 20 – 25 – 30 - 35  $\mu\text{m}$  in different order. In this way there are FET with the same channel length on different regions of the  $\text{MoS}_2$  film. The design is reported in Fig. 3.13

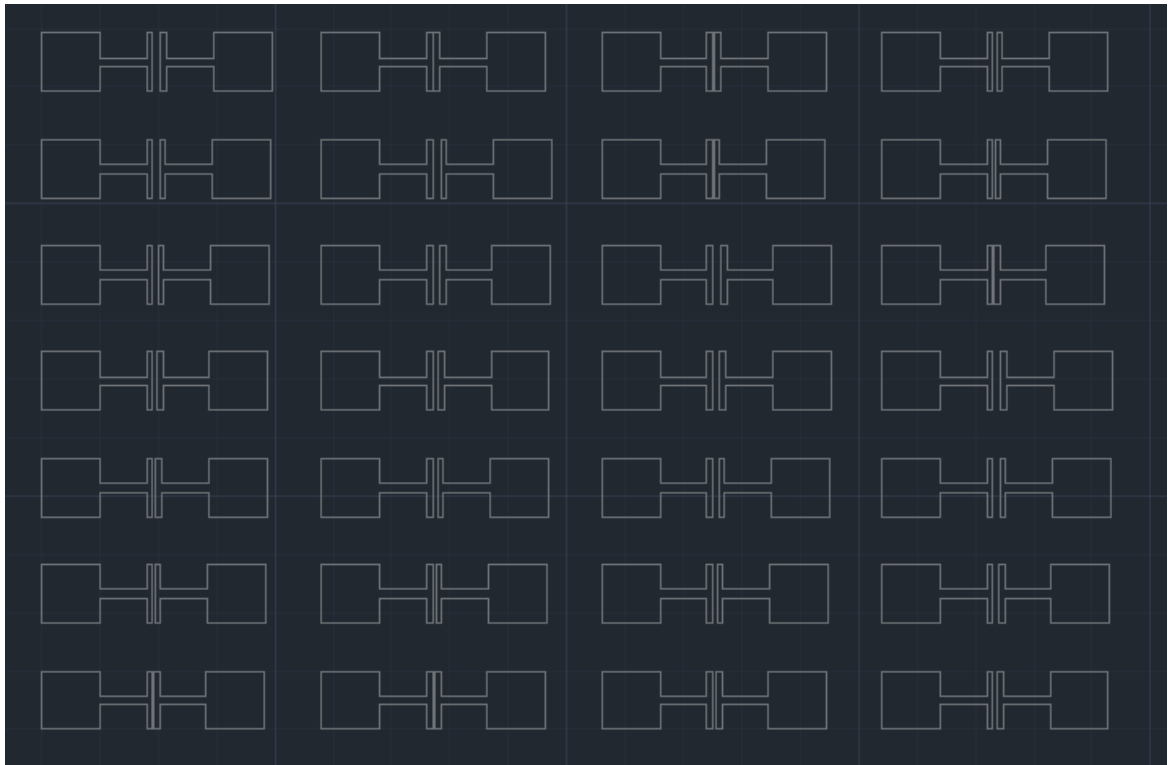


*Figure 3.13: Design of the grid of devices patterned on the  $\text{MoS}_2$  samples.*

Following the developing step, a 6 nm thick Ti layer was deposited on the samples followed by a 100 nm thick Au layer. Both metals were deposited using DC magnetron sputtering. Finally, the liftoff process was performed. The final device is shown in Fig. 3.14

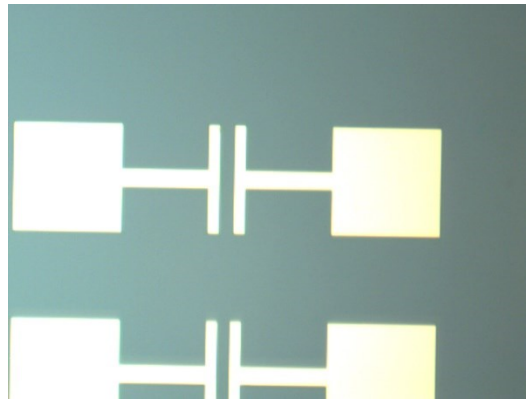


Figure 3.14: Image obtained via optical microscopy of the final device.

To create the gate contact, the SiO<sub>2</sub> layer was removed on one of the edges of the samples and then silver paste was deposited on them.

### 3.5.2 Electrical measurements

The final step consists in the measurement of the I-V curves at the probe station to extract relevant parameters such as the mobility and the contact resistance. The gate terminal at the edge was polarized with a fixed potential, the source pad was kept at 0 V, while the drain pad was varied between  $\pm 10$  V. Unfortunately, Figure 3.15 shows no relevant current either for the 1 ML sample or for the 2/3 ML one with a 5  $\mu\text{m}$  channel.

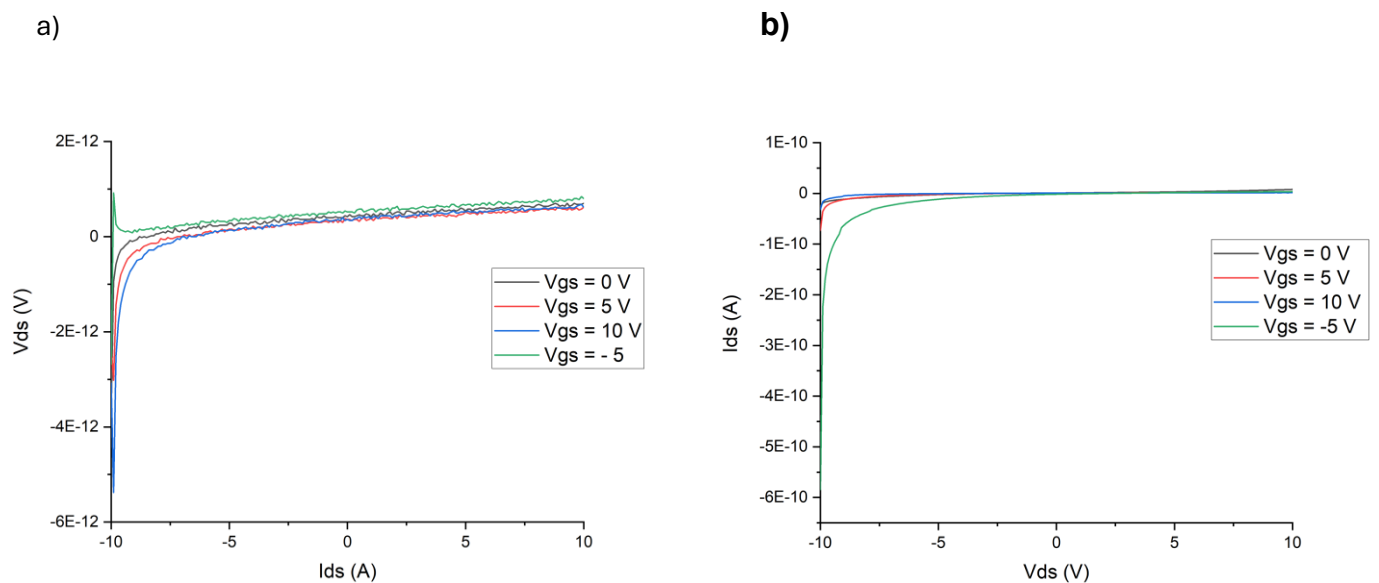


Figure 3.15:  $i_{DS} - V_{DS}$  curves at different  $V_{GS}$  voltages of FET devices fabricated on (a) 1 ML sample and (b) 2/3 ML sample.

A possible explanation for this behavior was the degradation of the  $\text{MoS}_2$  during the photolithography process. In order to verify this, FET were fabricated without the photolithography by using a shadow mask to deposit the metallic contact (supplied by Ossila). These masks are put into contact with the samples and allow the fabrication of pads similar to those fabricated using photolithography. A schematic of these masks is reported in Fig. 3.16.

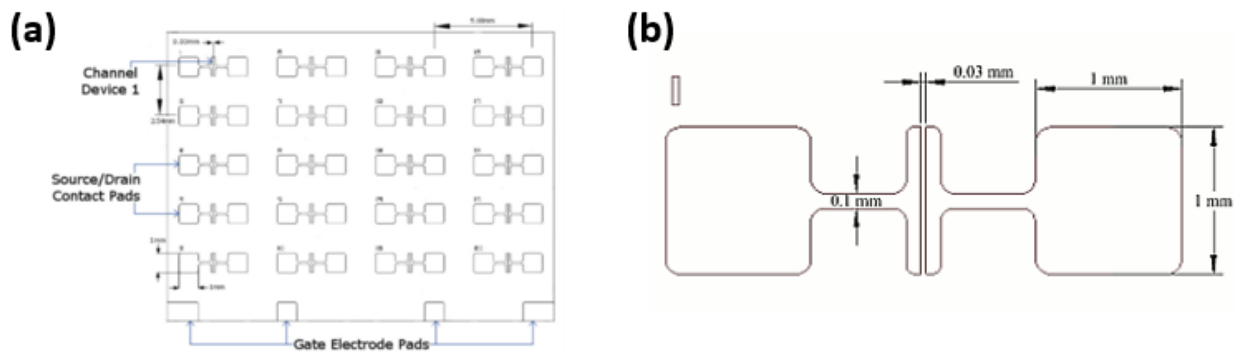
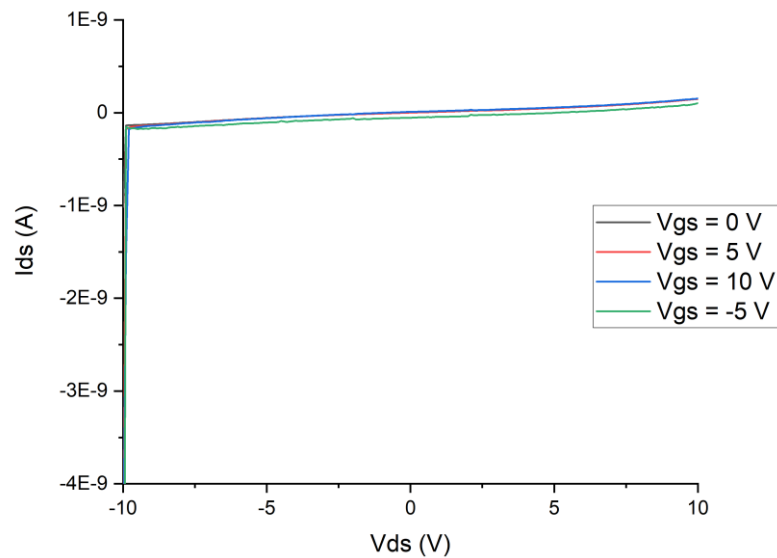


Figure 3.16: (a) Scheme of the source-drain deposition mask. Each mask contains 20 devices with channel lengths 30, 40, 60 or 80  $\mu\text{m}$  (b) Dimension detail of a single FET.



In particular, these devices were then fabricated by depositing the same thickness of Ti and Au on a 2/3 ML sample. The devices were then tested on the probe station but still no significant current was found, as it is reported in Fig. 3.17 for a device with 30  $\mu\text{m}$  channel length.



*Figure 3.17:  $I_{DS} - V_{DS}$  curves at different  $V_{GS}$  voltages of FET devices fabricated using a shadow mask on a 2/3 ML sample.*

The low current measured in FET devices fabricated using a shadow mask to create metallic contacts is an unexpected result, as we instead successfully used the same procedure in the past in MoS<sub>2</sub> layers fabricated by sputter deposition followed by Laser annealing. If the photolithographic FET fabrication process caused degradation of the MoS<sub>2</sub> films, this should not occur when the contacts are deposited using a physical shadow mask. To investigate this, Raman spectra were acquired to verify any structural modifications in the MoS<sub>2</sub> film within the FET channel. Representative spectra are shown in Fig. 3.18. The results indicate a significant reduction in the peak intensity of the E<sub>12g</sub> and A<sub>11g</sub> modes after sputtering deposition of the Ti/Au contacts. The signal intensity is comparable to that of a single monolayer of MoS<sub>2</sub>, suggesting potential delamination of the film. Compared to the reference signal, the peak spacing is larger than in a pristine 1 ML film, which could be explained by the increased disorder following the delamination process [Mignuzzi et al., 2015]. This suggests that the critical process is not photolithography, but the deposition of metal contacts by magnetron sputtering. It is important to note that the use of 'unbalanced

type-II' magnetron sources exposes the plasma to the sample surface. This could be problematic for TMDs due to the weak van der Waals bonds between single layers and between the material stack and the substrate, making TMDs an inherently fragile material class. To address this issue, a potential solution for future applications is to use less aggressive metal deposition techniques, such as thermal evaporation or e-beam evaporation. These methods rely on high-directional metal plumes generated by thermal sublimation, which reach the substrate without plasma generation.

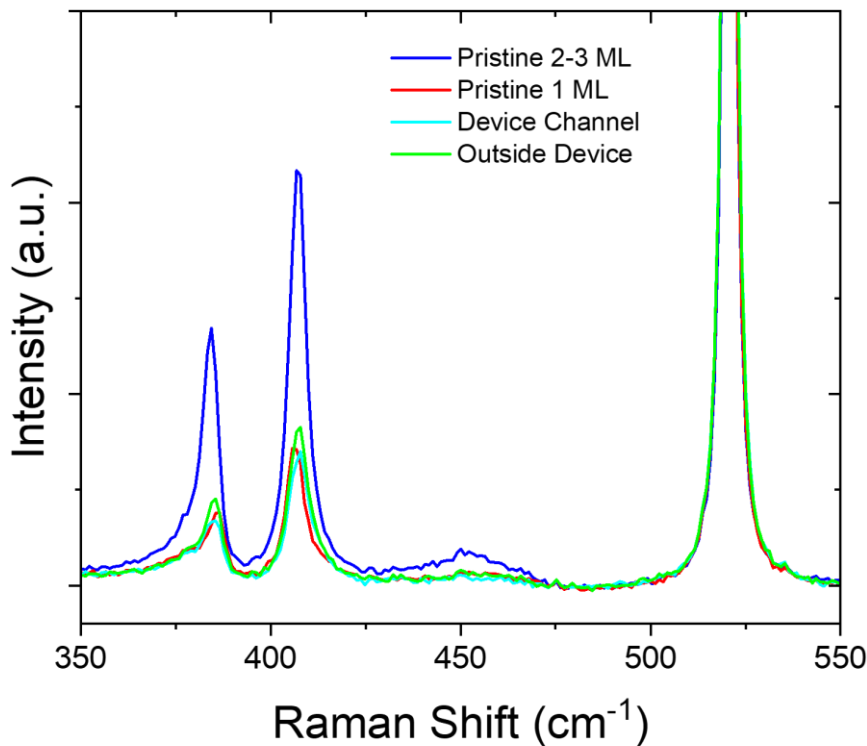


*Figure 3.18: Raman spectra measured inside and outside a FET device channel in a 2-3 ML film after metal contact sputter deposition compared with pristine 2-3 ML and 1ML film spectra.*

While the proposed interpretation may lead to significant improvements in FET performance, an alternative approach to enhancing device performance could involve addressing the damage caused by sputtering at the metal-TMD interface. When such damage occurs, it is expected to result in very high contact resistance, leading to a substantial reduction in the current flowing through the device. To mitigate this issue, the Ti-MoS<sub>2</sub> contacts were subjected to laser processing to explore the effects of this thermal treatment on the overall device properties. The next section will describe the experimental result obtained in this context.

## 3.6 LASER AND THERMAL PROCESSING OF Ti/MoS<sub>2</sub> CONTACT

### 3.6.1 MoS<sub>2</sub> film stability to PLA

The first step for semiconductor/metal interface optimization through pulsed laser annealing was the study of the effect of PLA processes on the MoS<sub>2</sub> film. The aim was to identify a suitable process window in which the TMD film crystallinity was improved or not modified by the process. The laser energy density (ED) was varied in the range from 50 to 200 mJ/cm<sup>2</sup> with a variable number of applied pulses from 1 to 8.

Raman spectroscopy was applied to evaluate the changes in the crystalline phase of the film. In order to evaluate the evolution of the Raman spectra the following quantities were calculated for each annealing condition:

1. Height ratio between MoS<sub>2</sub> A<sub>1g</sub> peak and Si peak (substrate).
2. Area ratio between MoS<sub>2</sub> A<sub>1g</sub> peak and Si peak (substrate).
3. Width of MoS<sub>2</sub> A<sub>1g</sub> peak.
4. Distance between MoS<sub>2</sub> A<sub>1g</sub> and E<sub>2g</sub> peaks.

These quantities are plotted in the following as a function of laser ED for both 1 ML and 2-3 ML films. In order to verify if the uniformity of the film was maintained after the PLA process, Raman spectra were acquired in different location inside the same laser spot. The reported error bars represent the standard variation of the measured signals. Firstly, representative spectra are reported in Fig. 3.19 for both types of film. In shown spectral window, the in-planes E<sub>2g</sub><sup>1</sup> mode is found at around 383 cm<sup>-1</sup> for 1 ML (382 cm<sup>-1</sup> for 2-3 ML) and the out-of-plane A<sub>1g</sub> mode is located at around 405 cm<sup>-1</sup> (406 cm<sup>-1</sup> for 2-3 ML) as expected for a MoS<sub>2</sub> film with this number of layers. Even if the MoS<sub>2</sub> peaks are stable for the lower investigated ED, a general signal reduction can be observed for an increasing ED up to 200 mJ/cm<sup>2</sup>.

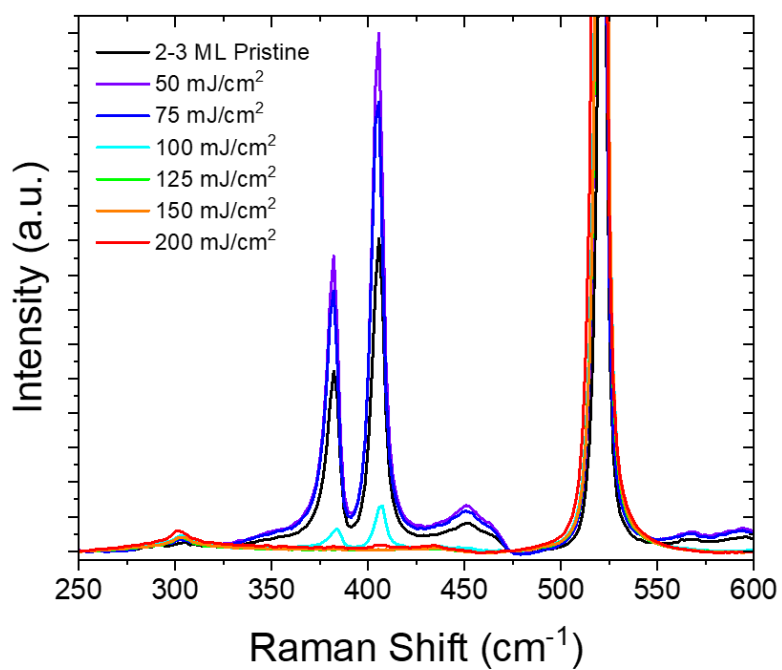
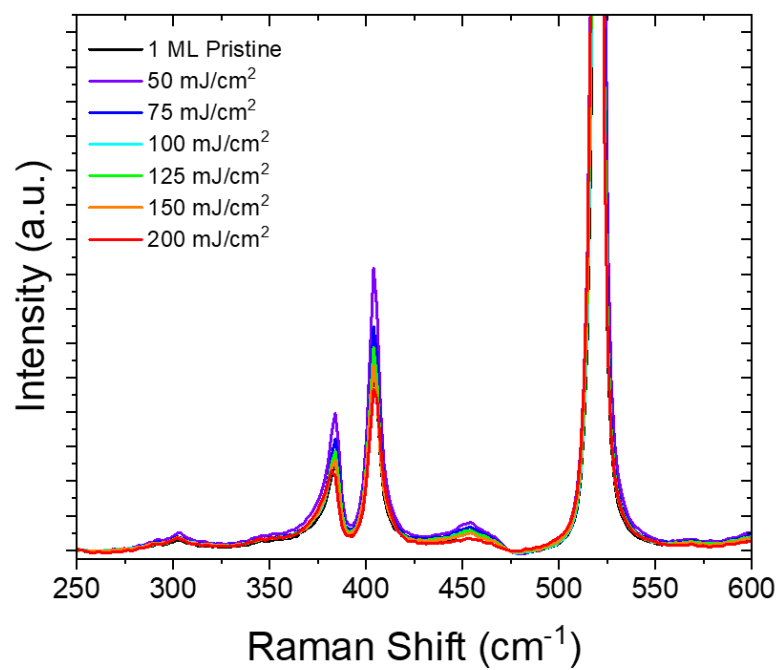


Figure 3.19: Evolution of the Raman spectra of a 1ML (top) and 2-3 ML (bottom) MoS<sub>2</sub> samples pulsed laser annealed under several ED conditions, from 50 to 200 mJ/cm<sup>2</sup>.

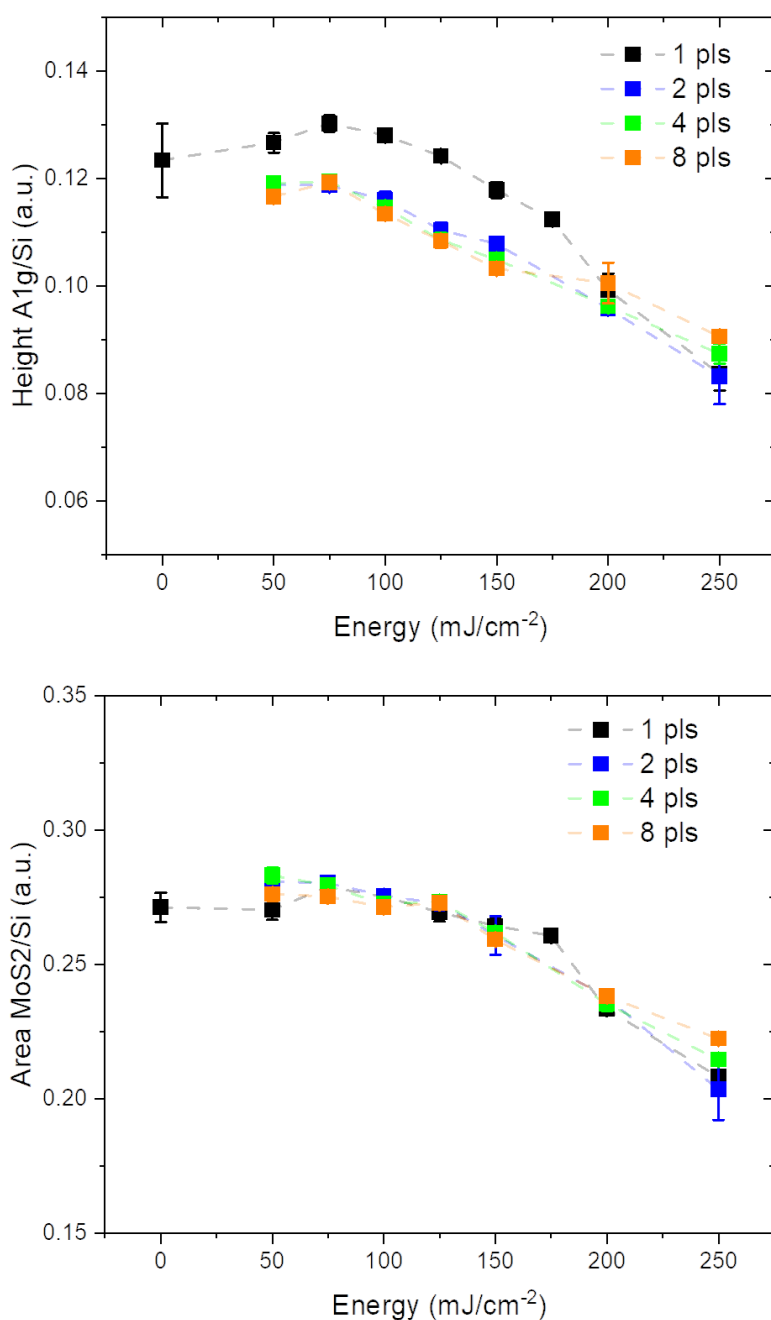


Figure 3.20: Changes of the Raman signal as a function of the ED for a single or multipulse PLA in 1 ML MoS<sub>2</sub> film: A<sub>1g</sub>/Si height ratio (top) and area ratio (bottom).

A<sub>1g</sub> height ratio and area ratio are reported for both film types in Fig 3.20 and Fig 3.21. In each case, both area and height ratio present a similar trend. For the 1 ML film the peak height is slightly improve with a ratio to Si peak remaining above 12% for a single pulse

perform at an ED to  $100 \text{ mJ/cm}^2$ . Above this threshold the film quality starts to deteriorate with the ratio reaching 9% and an increasing inhomogeneity starts to appear as shown by increasing error bars. For multiple pulses there is no quality improvement at low ED but the decreasing signal trend is still present for both 2, 4 and 8 pulses. The area ratio exhibits a decreasing film crystallinity for increasing ED in agreement with the height analysis.

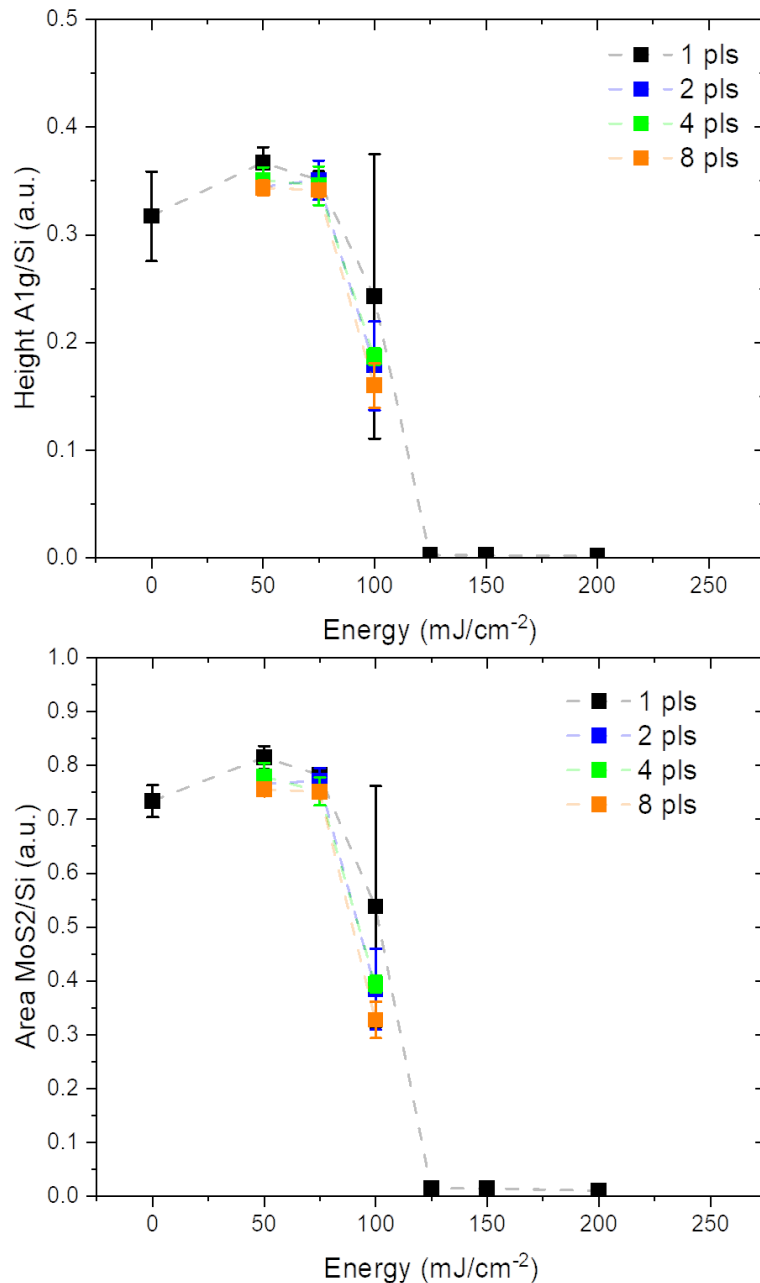
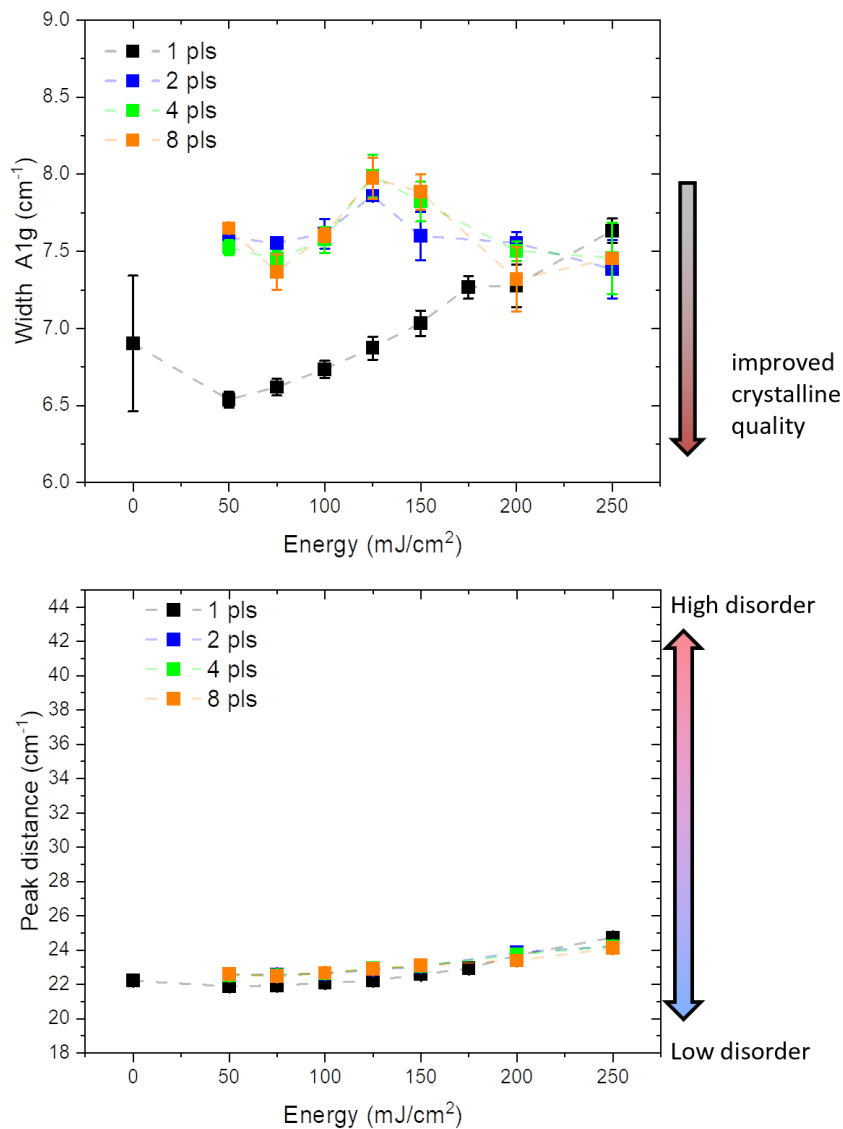


Figure 3.21: Changes of the Raman signal as a function of the ED for a single or multipulse PLA in 2-3 ML  $MoS_2$  film:  $A_{1g}/Si$  height ratio (top) and area ratio (bottom).

The effect is quite different in the 2-3 ML film (see Fig. 3.21): in this case both area and height analysis reveal a small signal improvement for ED between 50 and 75 mJ/cm<sup>2</sup>, with a single pulse treatment achieving the highest intensity. As opposed to the 1 ML film, at around 100 mJ/cm<sup>2</sup> a sudden deterioration of the film takes place with the Raman signal halving with respect to the initial film, resulting in very inhomogeneous film. Above this threshold no Raman signal is detected. This is most likely due to the complete ablation of the film after laser annealing.



*Figure 3.22: Changes of the Raman signal as a function of the ED for a single or multipulse PLA in 1 ML MoS<sub>2</sub> film: A<sub>1g</sub> peak width (top) and A<sub>1g</sub>-E<sub>2g</sub> peaks distance(bottom).*

In Fig 3.22 the width of the A<sub>1g</sub> peak and the A<sub>1g</sub>-E<sub>2g</sub> peaks distance are reported as a function of ED: comparing the trend with the one reported in Fig. 3.21, it is clear that the signal intensity reduction after PLA is followed by a broadening of the peak. This can be explained with an increasing disorder degree after annealing that produce a lower crystalline quality [Mignuzzi et al, 2015] This effect is particularly evident for multiple pulses treatments and single pulse treatment for ED higher than 100 mJ/cm<sup>2</sup>. Similarly, the peak distance increase from 22 cm<sup>-1</sup> in the pristine film, which is compatible with the presence of a monolayer, toward 24 cm<sup>-1</sup>: this can be explained again as the result of an higher degree of disorder in the material [Mignuzzi et al, 2015].



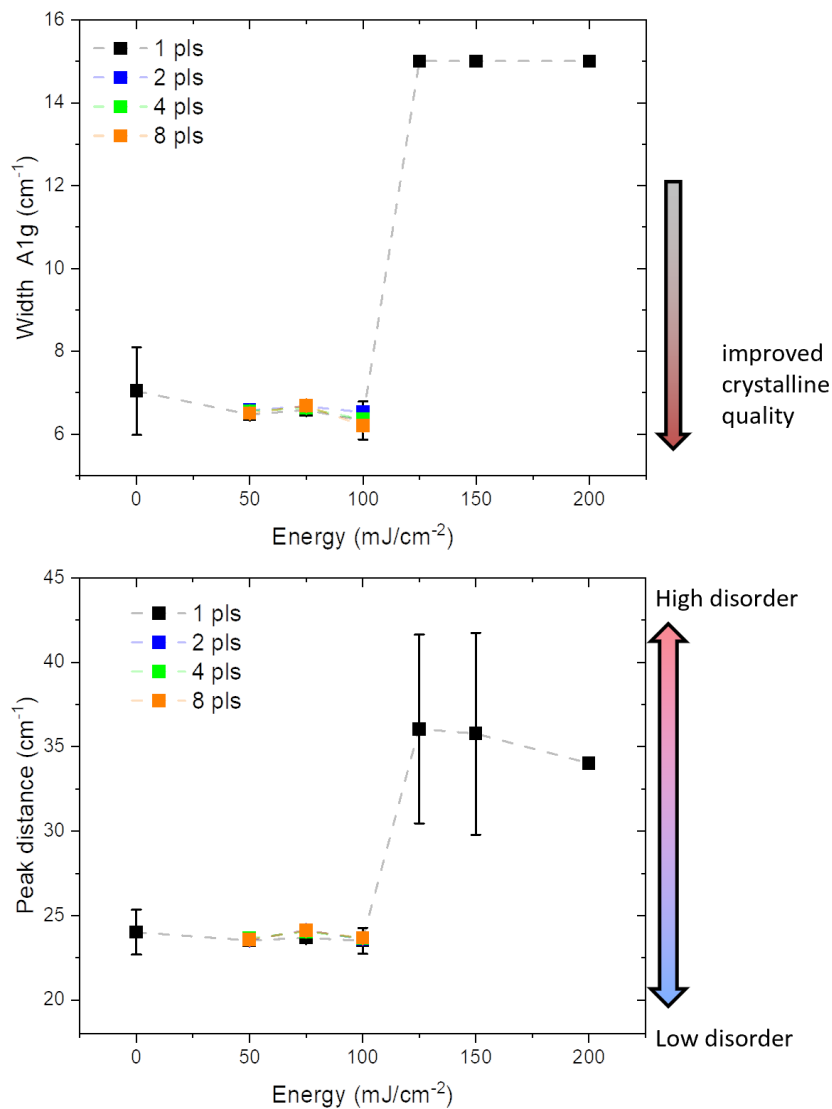


Figure 3.23: Changes of the Raman signal as a function of the ED for a single or multipulse PLA in 2-3 ML MoS<sub>2</sub> film: A<sub>1g</sub> peak width (top) and A<sub>1g</sub>-E<sub>2g</sub> peaks distance (bottom).

The same plot is reported for 2-3 ML films in Fig. 3.23: in this case the effect of ablation of part of the film results in a strong difference before and after the 100 mJ/cm<sup>2</sup> threshold. If the applied ED is too high, both peak width and peaks distance become larger indicating the introduction of a high level of disorder, where part of the film is being removed.

Quantitative information about the sample morphology evolution were acquired through AFM, by taking  $1 \times 1 \mu\text{m}^2$  AFM maps of sample surface under several ED conditions.

In Fig. 3.24 the surface features measured in the case of a 1 ML film show a very flat surface in all investigated cases. The surface roughness, reported for each map, highlight how no significant variation occurred in the film in the ED window 50-125  $\text{mJ}/\text{cm}^2$  where the Raman signal is preserved as well, Thus, this window is appealing for metal/semiconductor interface improvement through PLA.

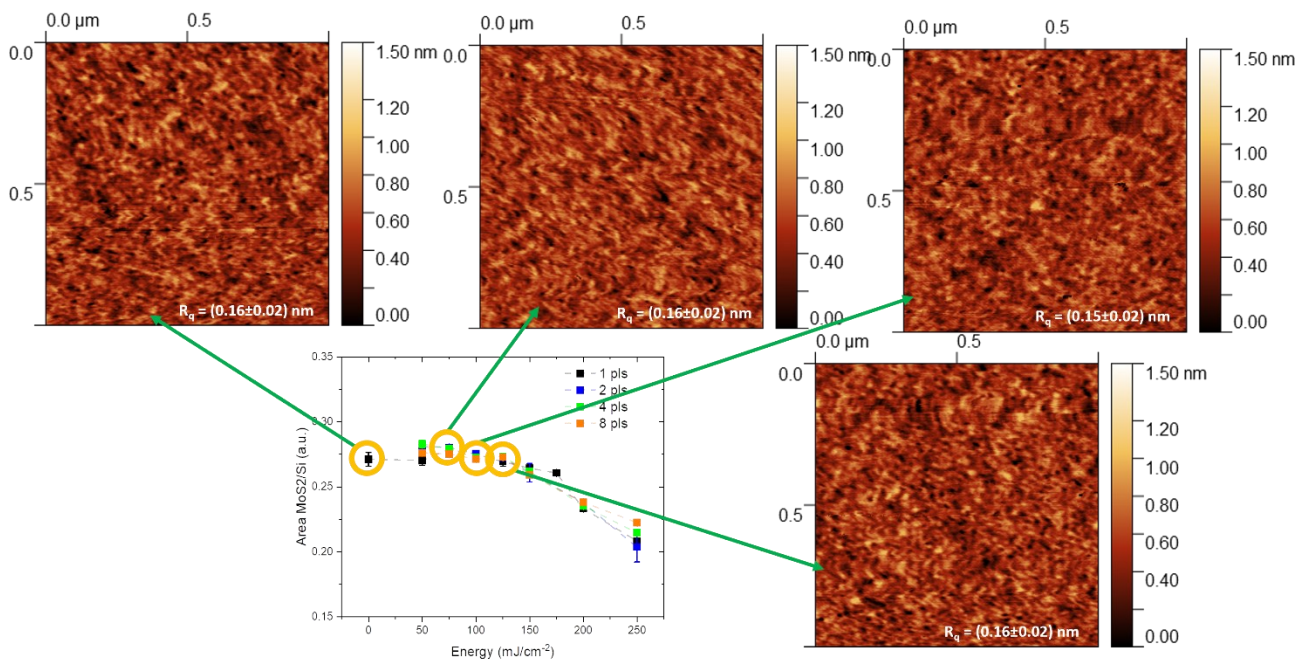


Fig. 3.24: AFM maps of the 1 ML  $\text{MoS}_2$  after performing laser annealing varying the laser energy density with comparison with the measured Raman signal intensity. The images size is  $1 \times 1 \mu\text{m}^2$ . The surface roughness  $R_q$  is reported below each map.

On the contrary the 2-3 ML film AFM maps reported in Fig. 3.25, show a surface roughness increases already at the threshold ED (i.e. 100  $\text{mJ}/\text{cm}^2$ ) where the ablation of significant portion of the film is followed by the formation of large coalescences with a height of around 15 nm. Coalescences are detected with no distinguishable portion of the film present when processing the sample above the ED threshold. For this reason, the ED window for contact annealing must be set below 100  $\text{mJ}/\text{cm}^2$  to avoid damaging the  $\text{MoS}_2$  film.

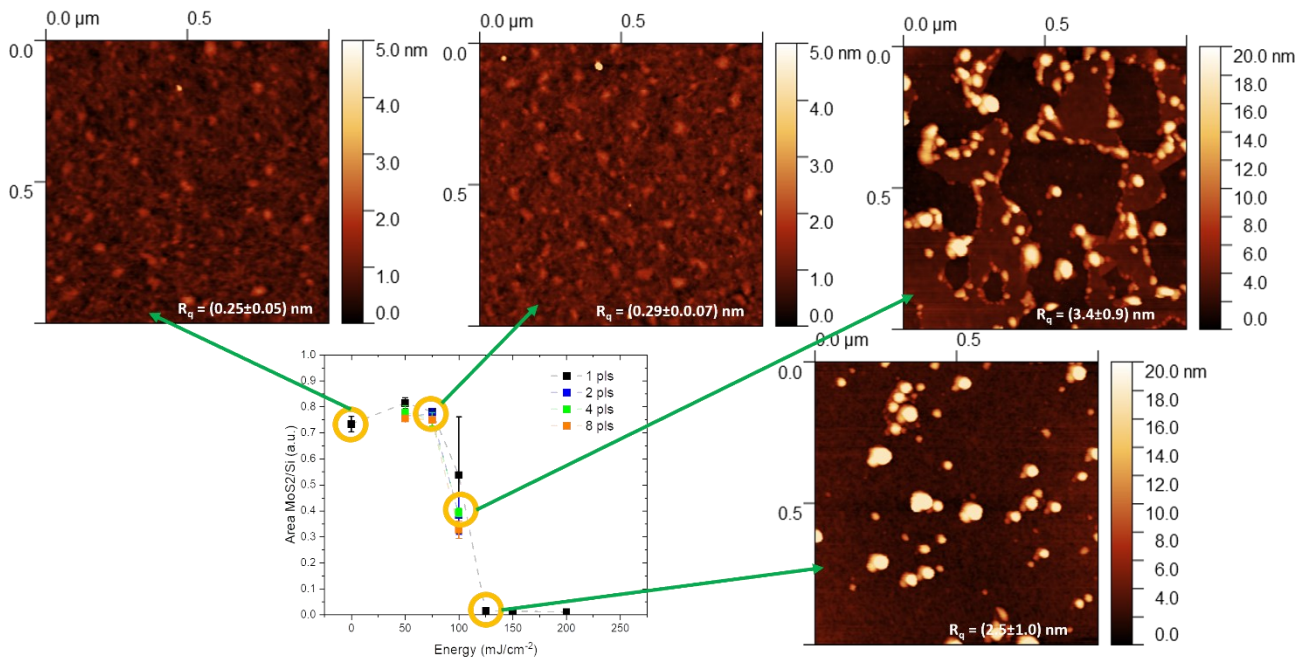


Fig. 3.25: AFM maps of the 2-3 ML MoS<sub>2</sub> after performing laser annealing varying the laser energy density with comparison with the measured Raman signal intensity. The images size is 1 × 1 μm<sup>2</sup>. The surface roughness R<sub>q</sub> is reported below each map.

### 3.6.2 Laser processing of the contacts

First, a 3 nm Ti layer was deposited via DC sputtering on two samples of 1 ML MoS<sub>2</sub> and 2/3 ML MoS<sub>2</sub>. A 1 ML and a 2/3 ML sample were processed using different conditions. On the 1 ML sample a grid was prepared where the energy density was varied from 50 to 150 mJ/cm<sup>2</sup>, with steps of 25 mJ/cm<sup>2</sup> while the number of impulses was varied from 1 to 16 (1,2,4,8,16) impulses.

Raman spectra of the processed spots were acquired. According to the literature [Schaube et al. 2020], Ti could react with the S of the MoS<sub>2</sub> and forms a Ti<sub>x</sub>S<sub>y</sub> compound that leads to the disappearance of the characteristic MoS<sub>2</sub> A<sub>1g</sub> and E<sub>2g</sub> bands. This is confirmed by the Raman spectra reported in Figure 3.26

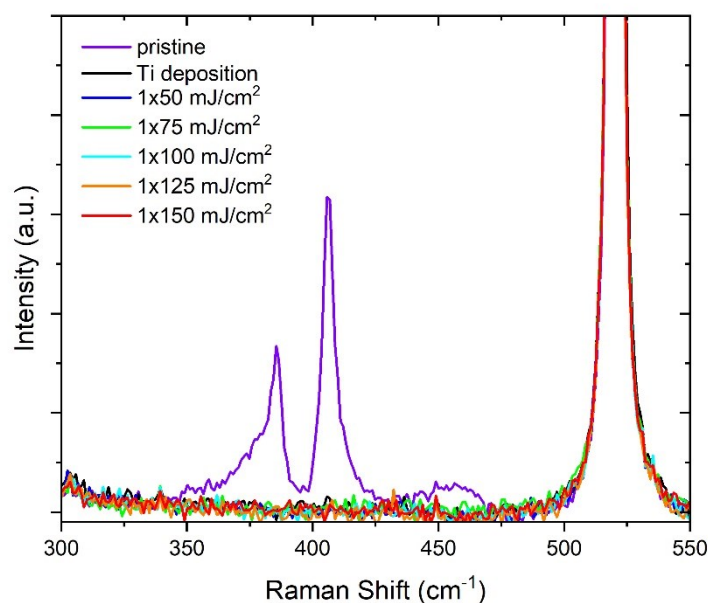


Figure 3.26 Raman spectra of a 1ML MoS<sub>2</sub> samples deposited with 6 nm thick Ti and processed under 50 – 75 – 100 – 125 – 150 mJ/cm<sup>2</sup>

The regions subjected to PLA at different energies were then analyzed using AFM. The images obtained are reported in Figure 3.27

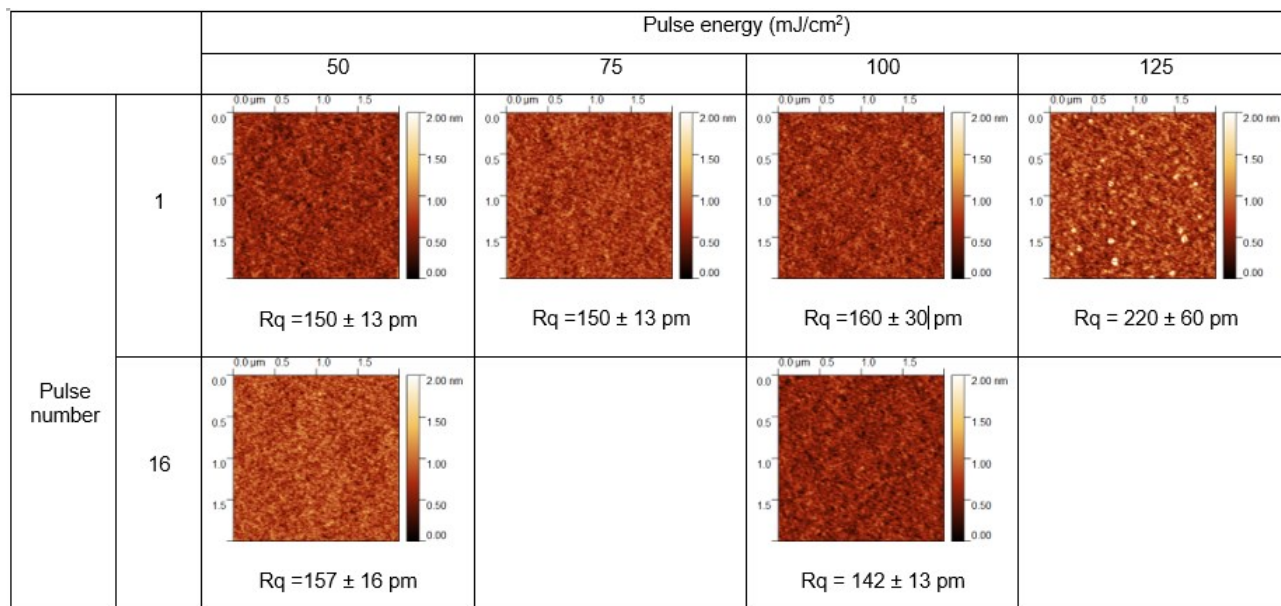
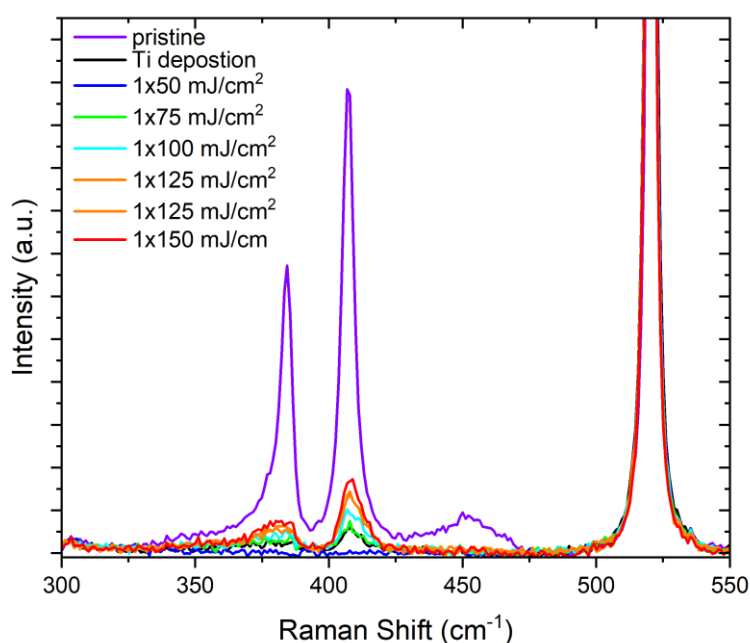


Fig. 3.27: AFM maps of the Ti/MoS<sub>2</sub> contact after performing laser annealing. The images size is 2×2 μm<sup>2</sup>. The surface roughness R<sub>q</sub> is reported below each map.

It is seen that in the case of 1 ML MoS<sub>2</sub> coated with Ti there is an energy density threshold of 100 mJ/cm<sup>2</sup> after which the contact is degraded as it is seen from the roughness values.

The 2/3 ML MoS<sub>2</sub> coated with Ti was instead processed with a series of single pulses from 50 to 150 mJ/cm<sup>2</sup> and subsequently these spots were analyzed using Raman spectroscopy. The results are reported in Figure 3.28



*Figure 3.28 Raman spectra of a 2/3ML MoS<sub>2</sub> samples deposited with 6 nm thick Ti and processed under 50 – 75 – 100 – 125 – 150 mJ/cm<sup>2</sup>*

A clear Raman signal associated to the presence of a MoS<sub>2</sub> layer is still present after the deposition of Ti. This indicates that there are MoS<sub>2</sub> sheets, probably not in contact with the Ti that did not react with the metal. At 50 mJ/cm<sup>2</sup> the MoS<sub>2</sub> peaks disappear, indicating that a reaction between the Ti and the underlying sheets might have taken place. As the ED increases, the intensity of the MoS<sub>2</sub> peaks also increases. One hypothesis is that the laser is removing the layers of Ti and the layer of MoS<sub>2</sub> in contact with the metal that reacted with it, by breaking the Van der Waals bonds between the different sheets. To avoid this problem, a grid was constructed with energies from 50 – 60 – 70 – 80 – 100 mJ/cm<sup>2</sup>. 100 mJ/cm<sup>2</sup> was

chosen as the upper threshold because in that case the Raman signal increased past the signal of the as deposited sample, indicating that more Ti was being removed.

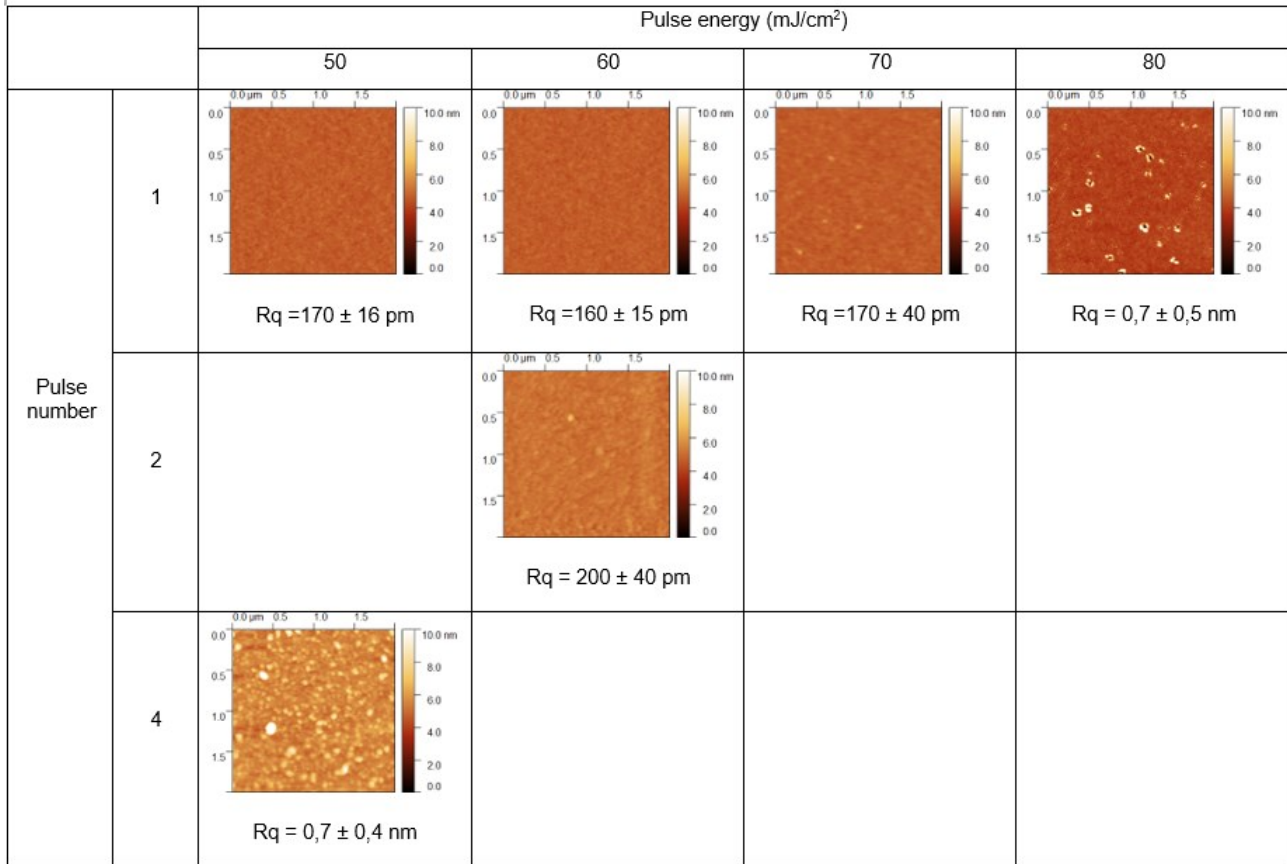


Fig. 3.29: AFM maps of the Ti 2/3 ML MoS<sub>2</sub> contact after performing laser annealing. The images size is 2×2 μm<sup>2</sup>. The surface roughness R<sub>q</sub> is reported below each map.

In the case of the 2/3 ML sample, it is evident also the number of impulses has an effect. This can be explained as before by the fact that already at lower energy densities the laser breaks the weak Van der Waals interactions that keep the different MoS<sub>2</sub> sheets together. This means that multiple impulses at the same energy degrade the contact between the different layers.

### 3.6.2 Laser processing of the pads

To study the effect of the laser processing on the electrical properties of the Ti/MoS<sub>2</sub> FET devices were fabricated via photolithography using the design reported in paragraph 3.2. The process described differs from that in paragraph 3.5.1 in that, after depositing the 6 nm Ti layer, liftoff was carried out, and the source and drain contacts were processed using one impulse of 50 mJ/cm<sup>2</sup>. This step would have been followed by another photolithography

process to deposit the 100 nm thick Au layer on the top of the Ti contacts. Figure 3.30 shows the effect of the laser on the Ti contacts.

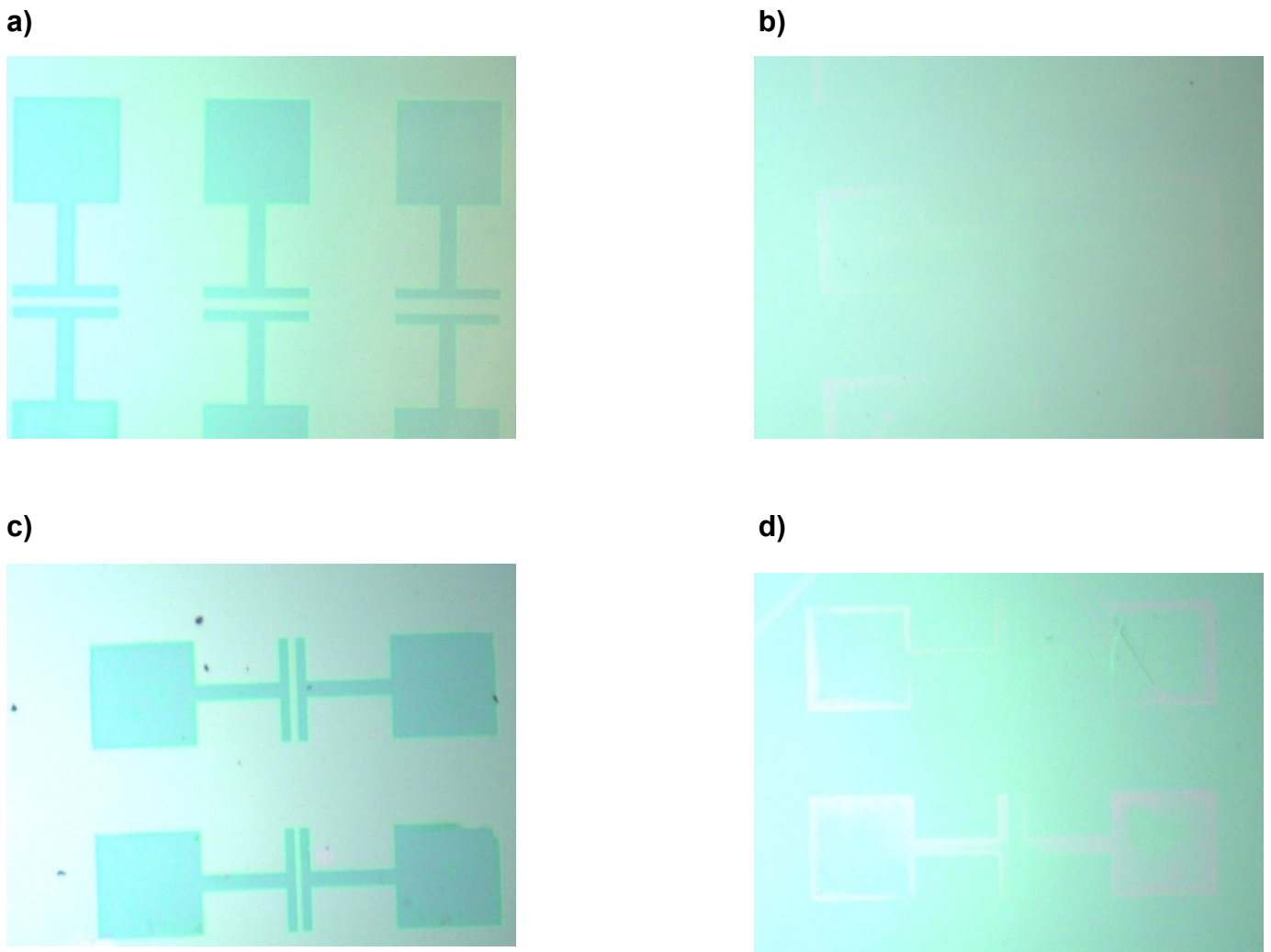


*Figure 3.30: (a) Ti pads on 1 ML MoS<sub>2</sub> before laser processing. (b) Same region of Fig. a after a 50 mJ/cm<sup>2</sup> laser pulse. (c) Ti pads on 2/3 ML MoS<sub>2</sub> before laser processing. (d) Same region of Fig. c after a 50 mJ/cm<sup>2</sup> laser pulse.*

The laser pulse removed the Ti pads and the MoS<sub>2</sub> near the edges of the contacts. On the contrary, no removal of Ti and MoS<sub>2</sub> was observed on a continuous layer of Ti/MoS<sub>2</sub> after PLA at 50 mJ/cm<sup>2</sup>. This result could be attributed to damage caused by sputtering on the MoS<sub>2</sub> near the device's edge, making it more susceptible to removal by the laser pulse. It is

possible that the Ti overlay near the edges is removed along with the semiconductor film. Consequently, the Ti near the edges may pull the more distant Ti along with it. This hypothesis might explain why a small Ti deposit, such as the one forming the FET, is removed while larger deposits remain unaffected.



## CHAPTER 4: CONCLUSIONS AND PERSPECTIVES

This thesis outlines a comprehensive study of the fabrication process of a backgated Field Effect Transistor (FET) on a MoS<sub>2</sub>/SiO<sub>2</sub>/Si substrate, reporting a critical, in-depth analysis of the potential issues that may arise during the fabrication process and proposing some technical solution.

First, an appropriate geometry was chosen for the drain and source electrodes using AutoCAD as the designing tool. Then, the study of different solvents on the MoS<sub>2</sub> was carried out. Acetone and Isopropanol were found to be the solvents that leave the MoS<sub>2</sub> film unaltered. Next, the optimal soft baking temperature of the lift-off resist and liftoff temperature were determined to be both 160 °C. These parameters are strictly related to the dissolution mechanism of the resist polymer. In particular, it is necessary to avoid the cracking of the polymer and the subsequent eruption of small blocks of polymer into the solvents that might lead to a delamination of the MoS<sub>2</sub> film. Once these parameters were identified, the optimal energy density of the UV source used to irradiate the resist was determined to be 125 mJ/cm<sup>2</sup> along with the appropriate developing time of 90 seconds. An energy density below 200 mJ/cm<sup>2</sup> ensures a reduced proximity effect thus a more accurate reproduction of the AutoCAD design pattern. Finally, FET devices were fabricated by sputtering a Ti/Au layer on a physical mask patterned using the parameters reported above and electrical measurements were carried out at the probe station however, no relevant currents were found. An attempt to measure currents on devices fabricated using shadow masks yielded the same result. This, along with Raman spectra acquired on the MoS<sub>2</sub> film after the device fabrication suggest that metal sputtering introduce damage in the crystalline structure that severely degrade its electrical properties and might suggest the need for metal deposition techniques like e-beam or thermal evaporation. Another approach relies on the thermal treatment of the damage introduced during the sputtering at the metal-TMD interface, therefore Pulsed Laser Annealing (PLA) was investigated as a potential solution. The laser conditions that leave the Ti/MoS<sub>2</sub> contact were determined by studying the morphology via Atomic Force Microscopy (AFM). In particular, an energy threshold of 100 mJ/cm<sup>2</sup> leaves a 6 nm thick Ti layer deposited on 1 monolayer (ML) MoS<sub>2</sub> unaltered, regardless of the number of pulses. Instead, 70 mJ/cm<sup>2</sup> and 1 impulse or 60 mJ/cm<sup>2</sup> and 2

impulses are the stability ranges for Ti contacts with 2/3 ML thick MoS<sub>2</sub>. This might be explained by the breaking of the weak Van der Waals bonds between the MoS<sub>2</sub> sheets that affects the 2/3 ML thick samples. Finally, PLA performed on patterned Ti contacts led to the removal of the metal. This suggests that sputtering damage on the MoS<sub>2</sub> near the device's edge makes it more vulnerable to laser pulse removal. This may cause the Ti overlay near the edges to be removed along with the semiconductor film, potentially leading to the removal of distant Ti as well.

In summary, this thesis focused on investigating the key steps in fabricating FET devices, aiming to address critical challenges reported in the literature. These include preventing film delamination during the lithography process and enhancing device performance through optimized contact deposition. By fine-tuning photolithography parameters, consistent reproducibility in device fabrication was achieved. Additionally, PLA was applied to the MoS<sub>2</sub> film, revealing an ED window where no modifications occur. This finding paves the way for processing Ti/MoS<sub>2</sub> contacts to reduce contact resistance without damaging the semiconductor film. The results and considerations reported in this thesis could be used as a starting point to improve devices performance. Prospective works might investigate the use of other metal deposition that introduce less damage, such as e-beam and thermal evaporation, and then PLA can be studied as a possible method to improve these contacts. Finally, deposition of physical masks via photolithography might be followed by a selective etching of the underlying MoS<sub>2</sub>. This would allow the fabrication of lateral metal-TMD interfaces that present an improved contact resistance.

## BIBLIOGRAPHY

- Algara-Siller, G., Kurasch, S., Sedighi, M., Lehtinen, O., & Kaiser, U. (2013). The pristine atomic structure of MoS<sub>2</sub> monolayer protected from electron radiation damage by graphene. *Applied Physics Letters*, 103(20), 203107.
- Allen, M. J., Tung, V. C., & Kaner, R. B. (2010). Honeycomb carbon: a review of graphene. *Chemical reviews*, 110(1), 132-145.
- Acar, M., & Gür, E. (2021). Sputtered 2D transition metal dichalcogenides: from growth to device applications. *Turkish Journal of Physics*, 45(3), 131-147.
- Alrefae, M. A., Kumar, A., Pandita, P., Candadai, A., Billionis, I., & Fisher, T. S. (2017). Process optimization of graphene growth in a roll-to-roll plasma CVD system. *Aip Advances*, 7(11), 115102.
- Baker, M. A., Gilmore, R., Lenardi, C., & Gissler, W. (1999). XPS investigation of preferential sputtering of S from MoS<sub>2</sub> and determination of MoS<sub>x</sub> stoichiometry from Mo and S peak positions. *Applied surface science*, 150(1-4), 255-262.
- Beth A. Miller-Chou, Jack L. Koenig. (2003). A review of polymer dissolution. *Progress in Polymer Science*, 28 (8), 1223-1270,
- Bräuer, G., Szyszka, B., Vergöhl, M., & Bandorf, R. (2010). Magnetron sputtering–Milestones of 30 years. *Vacuum*, 84(12), 1354-1359.
- Cadot, S., Renault, O., Frégnaux, M., Rouchon, D., Nolot, E., Szeto, K., ... & Quadrelli, E. A. (2017). A novel 2-step ALD route to ultra-thin MoS<sub>2</sub> films on SiO<sub>2</sub> through a surface organometallic intermediate. *Nanoscale*, 9(2), 538-546.

Cai, Z., Liu, B., Zou, X., & Cheng, H. M. (2018). Chemical vapor deposition growth and applications of two-dimensional materials and their heterostructures. *Chemical reviews*, 118(13), 6091-6133.

Chang, H. Y., Yogeesh, M. N., Ghosh, R., Rai, A., Sanne, A., Yang, S., ... & Akinwande, D. (2016). Large-area monolayer MoS<sub>2</sub> for flexible low-power RF nanoelectronics in the GHz regime. *Advanced Materials*, 28(9), 1818-1823.

Chang, K. P., Wang, J. C., Chen, C. H., Li, L. J., & Lai, C. S. (2016, October). Monolayer MoS<sub>2</sub> for nonvolatile memory applications. In *2016 13th IEEE International Conference on Solid-State and Integrated Circuit Technology (ICSICT)* (pp. 489-491). IEEE.

Chhowalla, M., Jena, D., & Zhang, H. (2016). Two-dimensional semiconductors for transistors. *Nature Reviews Materials*, 1(11), 1-15.

Choi, W., Choudhary, N., Han, G. H., Park, J., Akinwande, D., & Lee, Y. H. (2017). Recent development of two-dimensional transition metal dichalcogenides and their applications. *Materials Today*, 20(3), 116-130.

Choudhury, T. H., Zhang, X., Al Balushi, Z. Y., Chubarov, M., & Redwing, J. M. (2020). Epitaxial growth of two-dimensional layered transition metal dichalcogenides. *Annual Review of Materials Research*, 50, 155-177.

Das, S., Robinson, J. A., Dubey, M., Terrones, H., & Terrones, M. (2015). Beyond graphene: progress in novel two-dimensional materials and van der Waals solids. *Annual Review of Materials Research*, 1-27.

English, C. D., Shine, G., Dorgan, V. E., Saraswat, K. C., & Pop, E. (2016). Improved contacts to MoS<sub>2</sub> transistors by ultra-high vacuum metal deposition. *Nano letters*, 16(6), 3824-3830.

Fang, H., Tosun, M., Seol, G., Chang, T. C., Takeji, K., Guo, J., & Javey, A. (2013). Degenerate n-doping of few-layer transition metal dichalcogenides by potassium. *Nano letters*, 13(5), 1991-1995.

Ferain, I., Colinge, C. A., & Colinge, J. P. (2011). Multigate transistors as the future of classical metal–oxide–semiconductor field-effect transistors. *Nature*, 479(7373), 310-316.

Ghatak, S., Pal, A. N., & Ghosh, A. (2011). Nature of electronic states in atomically thin MoS<sub>2</sub> field-effect transistors. *ACS nano*, 5(10), 7707-7712.

- Hernandez Ruiz, K., Wang, Z., Ciprian, M., Zhu, M., Tu, R., Zhang, L., ... & Jiang, W. (2022). Chemical vapor deposition mediated phase engineering for 2D transition metal dichalcogenides: Strategies and applications. *Small Science*, 2(1), 2100047.
- Hoang Huy, V. P., Ahn, Y. N., & Hur, J. (2021). Recent Advances in Transition Metal Dichalcogenide Cathode Materials for Aqueous Rechargeable Multivalent Metal-Ion Batteries. *Nanomaterials*, 11(6), 1517.
- Huang, J. H., Chen, H. H., Liu, P. S., Lu, L. S., Wu, C. T., Chou, C. T., ... & Hou, T. H. (2016). Large-area few-layer MoS<sub>2</sub> deposited by sputtering. *Materials Research Express*, 3(6), 065007.
- Huo, N., Yang, Y., Wu, Y. N., Zhang, X. G., Pantelides, S. T., & Konstantatos, G. (2018). High carrier mobility in monolayer CVD-grown MoS<sub>2</sub> through phonon suppression. *Nanoscale*, 10(31), 15071-15077.
- Jang, H. Y., Nam, J. H., Yoon, J., Kim, Y., Park, W., & Cho, B. (2020). One-step H<sub>2</sub>S reactive sputtering for 2D MoS<sub>2</sub>/Si heterojunction photodetector. *Nanotechnology*, 31(22), 225205.
- Jeong, J., Yoon, J. S., Lee, S., & Baek, R. H. (2020). Comprehensive analysis of source and drain recess depth variations on silicon nanosheet FETs for sub 5-nm node SoC application. *IEEE Access*, 8, 35873-35881.
- Ji, Q., Zhang, Y., Zhang, Y., & Liu, Z. (2015). Chemical vapour deposition of group-VIB metal dichalcogenide monolayers: engineered substrates from amorphous to single crystalline. *Chemical Society Reviews*, 44(9), 2587-2602.
- Joung, D., Park, H., Mun, J., Park, J., Kang, S. W., & Kim, T. (2017). Fabrication of two-dimensional MoS<sub>2</sub> films-based field effect transistor for high mobility electronic device application. *Applied Science and Convergence Technology*, 26(5), 110-113.
- Kaasbjerg, K., Thygesen, K. S., & Jacobsen, K. W. (2012). Phonon-limited mobility in n-type single-layer MoS<sub>2</sub> from first principles. *Physical Review B*, 85(11), 115317.
- Kang, D. H., Kim, M. S., Shim, J., Jeon, J., Park, H. Y., Jung, W. S., ... & Park, J. H. (2015). High-performance transition metal dichalcogenide photodetectors enhanced by self-assembled monolayer doping. *Advanced Functional Materials*, 25(27), 4219-4227.
- Kang, J., Liu, W., & Banerjee, K. (2014). High-performance MoS<sub>2</sub> transistors with low-resistance molybdenum contacts. *Applied Physics Letters*, 104(9), 093106.

Kaindl, R., Bayer, B. C., Resel, R., Müller, T., Skakalova, V., Habler, G., ... & Waldhauser, W. (2017). Growth, structure and stability of sputter-deposited MoS<sub>2</sub> thin films. *Beilstein journal of nanotechnology*, 8(1), 1115-1126.

Kim, B. H., Gu, H. H., & Yoon, Y. J. (2018). Large-area and low-temperature synthesis of few-layered WS<sub>2</sub> films for photodetectors. *2D Materials*, 5(4), 045030.

Kim, K. H., Kim, K. S., Ji, Y. J., Moon, I., Heo, K., Kang, D. H., ... & Yeom, G. Y. (2020). Effect of large work function modulation of MoS<sub>2</sub> by controllable chlorine doping using a remote plasma. *Journal of Materials Chemistry C*, 8(5), 1846-1851.

Klots, A. R., Newaz, A. K. M., Wang, B., Prasai, D., Krzyzanowska, H., Lin, J., ... & Bolotin, K. I. (2014). Probing excitonic states in suspended two-dimensional semiconductors by photocurrent spectroscopy. *Scientific reports*, 4(1), 1-7.

Komsa, H. P., Kotakoski, J., Kurasch, S., Lehtinen, O., Kaiser, U., & Krasheninnikov, A. V. (2012). Two-dimensional transition metal dichalcogenides under electron irradiation: defect production and doping. *Physical review letters*, 109(3), 035503.

Kozhakhmetov, A., Torsi, R., Chen, C. Y., & Robinson, J. A. (2020). Scalable low-temperature synthesis of two-dimensional materials beyond graphene. *Journal of Physics: Materials*, 4(1), 012001.

Kirstin Schauble, Dante Zakhidov, Eilam Yalon, Sanchit Deshmukh, Ryan W. Grady, Kayla A. Cooley, Connor J. McClellan, Sam Vaziri, Donata Passarello, Suzanne E. Mohney, Michael F. Toney, A. K. Sood, Alberto Salleo, and Eric Pop. (2020). Uncovering the Effects of Metal Contacts on Monolayer MoS<sub>2</sub>. *ACS Nano*, 14 (11), 14798-14808

Kwon, H., Garg, S., Park, J. H., Jeong, Y., Yu, S., Kim, S. M., ... & Im, S. (2019). Monolayer MoS<sub>2</sub> field-effect transistors patterned by photolithography for active matrix pixels in organic light-emitting diodes. *npj 2D Materials and Applications*, 3(1), 1-9.

Kumar, A., & Ahluwalia, P. K. (2013). Semiconductor to metal transition in bilayer transition metals dichalcogenides MX<sub>2</sub> (M= Mo, W; X= S, Se, Te). *Modelling and Simulation in Materials Science and Engineering*, 21(6), 065015.

Kumar, S., Sharma, A., Tomar, M., & Gupta, V. (2021). Realization of low-power and high mobility thin film transistors based on MoS<sub>2</sub> layers grown by PLD technique. *Materials Science and Engineering: B*, 266, 115047.

- Lai, Z., He, Q., Tran, T. H., Repaka, D. V., Zhou, D. D., Sun, Y., ... & Zhang, H. (2021). *Metastable 1T'-phase group VIB transition metal dichalcogenide crystals*. *Nature Materials*, 20(8), 1113-1120.
- Lee, Y., Lee, J., Bark, H., Oh, I. K., Ryu, G. H., Lee, Z., ... & Lee, C. (2014). *Synthesis of wafer-scale uniform molybdenum disulfide films with control over the layer number using a gas phase sulfur precursor*. *Nanoscale*, 6(5), 2821-2826.
- Lezama, I. G., Arora, A., Ubaldini, A., Barreteau, C., Giannini, E., Potemski, M., & Morpurgo, A. F. (2015). *Indirect-to-direct band gap crossover in few-layer MoTe<sub>2</sub>*. *Nano letters*, 15(4), 2336-2342.
- Li, J., & Östling, M. (2015). *Scalable fabrication of 2D semiconducting crystals for future electronics*. *Electronics*, 4(4), 1033-1061.
- Li, M., Esseni, D., Snider, G., Jena, D., & Grace Xing, H. (2014). *Single particle transport in two-dimensional heterojunction interlayer tunneling field effect transistor*. *Journal of Applied Physics*, 115(7), 074508.
- Li, S. L., Miyazaki, H., Song, H., Kuramochi, H., Nakaharai, S., & Tsukagoshi, K. (2012). *Quantitative Raman spectrum and reliable thickness identification for atomic layers on insulating substrates*. *ACS nano*, 6(8), 7381-7388.
- Li, S. L., Wakabayashi, K., Xu, Y., Nakaharai, S., Komatsu, K., Li, W. W., ... & Tsukagoshi, K. (2013). *Thickness-dependent interfacial coulomb scattering in atomically thin field-effect transistors*. *Nano letters*, 13(8), 3546-3552.
- Miika Mattinen, Jeff J. P. M. Schulpen, Rebecca A. Dawley, Farzan Gity, Marcel A. Verheijen, Wilhelmus M. M. Kessels, and Ageeth A. Bol. (2023). *Toolbox of Advanced Atomic Layer Deposition Processes for Tailoring Large-Area MoS<sub>2</sub> Thin Films at 150 °C*. *ACS Applied Materials & Interfaces*, 15 (29).
- Mak, K. F., Lee, C., Hone, J., Shan, J., & Heinz, T. F. (2010). *Atomically thin MoS<sub>2</sub>: a new direct-gap semiconductor*. *Physical review letters*, 105(13), 136805.
- Mignuzzi, S., Pollard, A. J., Bonini, N., Brennan, B., Gilmore, I. S., Pimenta, M. A., ... & Roy, D. (2015). *Effect of disorder on Raman scattering of single-layer Mo S<sub>2</sub>*. *Physical Review B*, 91(19), 195411.

Mironov, V. L. (2004). *Fundamentals of scanning probe microscopy: Textbook for senior students of higher educational institutions*. Institute for Physics of Microstructures of the Russian Academy of Sciences, Nizhny Novgorod, 110.

Musil, J. (1998). *Recent advances in magnetron sputtering technology*. *Surface and Coatings Technology*, 100, 280-286.

Nassiri Nazif, K., Daus, A., Hong, J., Lee, N., Vaziri, S., Kumar, A., ... & Saraswat, K. C. (2021). *High-specific-power flexible transition metal dichalcogenide solar cells*. *Nature Communications*, 12(1), 1-9.

Novoselov, K. S., Jiang, D., Schedin, F., Booth, T. J., Khotkevich, V. V., Morozov, S. V., & Geim, A. K. (2005). *Two-dimensional atomic crystals*. *Proceedings of the National Academy of Sciences*, 102(30), 10451-10453.

Pang, Y., Yang, Z., Yang, Y., & Ren, T. L. (2020). *Wearable electronics based on 2D materials for human physiological information detection*. *Small*, 16(15), 1901124.

Pawbake, A. S., Pawar, M. S., Jadkar, S. R., & Late, D. J. (2016). *Large area chemical vapor deposition of monolayer transition metal dichalcogenides and their temperature dependent Raman spectroscopy studies*. *Nanoscale*, 8(5), 3008-3018.

Pimpin, A., & Srituravanich, W. (2012). *Review on micro-and nanolithography techniques and their applications*. *Engineering Journal*, 16(1), 37-56.

Qian, Q., Lei, J., Wei, J., Zhang, Z., Tang, G., Zhong, K., ... & Chen, K. J. (2019). *2D materials as semiconducting gate for field-effect transistors with inherent over-voltage protection and boosted ON-current*. *npj 2D Materials and Applications*, 3(1), 1-9.

Radisavljevic, B., Radenovic, A., Brivio, J., Giacometti, V., & Kis, A. (2011). *Single-layer MoS<sub>2</sub> transistors*. *Nature nanotechnology*, 6(3), 147-150.

Radisavljevic, B., & Kis, A. (2013). *Mobility engineering and a metal–insulator transition in monolayer MoS<sub>2</sub>*. *Nature materials*, 12(9), 815-820.

Rohaizad, N., Mayorga-Martinez, C. C., Fojtů, M., Latiff, N. M., & Pumera, M. (2021). *Two-dimensional materials in biomedical, biosensing and sensing applications*. *Chemical Society Reviews*, 50(1), 619-657.

Saha, J. K., & Dutta, A. (2021). *A review of graphene: material synthesis from biomass sources*. *Waste and Biomass Valorization*, 1-45.



- Samadi, M., Sarikhani, N., Zirak, M., Zhang, H., Zhang, H. L., & Moshfegh, A. Z. (2018). Group 6 transition metal dichalcogenide nanomaterials: synthesis, applications and future perspectives. *Nanoscale Horizons*, 3(2), 90-204.
- Samassekou, H., Alkabsh, A., Wasala, M., Eaton, M., Walber, A., Walker, A., ... & Mazumdar, D. (2017). Viable route towards large-area 2D MoS<sub>2</sub> using magnetron sputtering. *2D Materials*, 4(2), 021002.
- Samy, O., Zeng, S., Birowosuto, M. D., & El Moutaouakil, A. (2021). A Review on MoS<sub>2</sub> properties, synthesis, sensing applications and challenges. *Crystals*, 11(4), 355.
- Schmidt, H., Giustiniano, F., & Eda, G. (2015). Electronic transport properties of transition metal dichalcogenide field-effect devices: surface and interface effects. *Chemical Society Reviews*, 44(21), 7715-7736.
- Schwierz, F., Pezoldt, J., & Granzner, R. (2015). Two-dimensional materials and their prospects in transistor electronics. *Nanoscale*, 7(18), 8261-8283.
- Sharma, A., Mahlouji, R., Wu, L., Verheijen, M. A., Vandalon, V., Balasubramanyam, S., ... & Bol, A. A. (2020). Large area, patterned growth of 2D MoS<sub>2</sub> and lateral MoS<sub>2</sub>-WS<sub>2</sub> heterostructures for nano-and opto-electronic applications. *Nanotechnology*, 31(25), 255603.
- Song, I., Park, C., & Choi, H. C. (2015). Synthesis and properties of molybdenum disulphide: from bulk to atomic layers. *Rsc Advances*, 5(10), 7495-7514.
- Splendiani, A., Sun, L., Zhang, Y., Li, T., Kim, J., Chim, C. Y., ... & Wang, F. (2010). Emerging photoluminescence in monolayer MoS<sub>2</sub>. *Nano letters*, 10(4), 1271-1275.
- Tan, L. K., Liu, B., Teng, J. H., Guo, S., Low, H. Y., & Loh, K. P. (2014). Atomic layer deposition of a MoS<sub>2</sub> film. *Nanoscale*, 6(18), 10584-10588.
- Thompson, S., Anand, N., Armstrong, M., Auth, C., Arcot, B., Alavi, M., ... & Bohr, M. (2002, December). A 90 nm logic technology featuring 50 nm strained silicon channel transistors, 7 layers of Cu interconnects, low k ILD, and 1/spl mu/m/sup 2/SRAM cell. In *Digest. International Electron Devices Meeting*, (pp. 61-64). IEEE.
- Tonndorf, P., Schmidt, R., Schneider, R., Kern, J., Buscema, M., Steele, G. A., ... & Bratschitsch, R. (2015). Single-photon emission from localized excitons in an atomically thin semiconductor. *Optica*, 2(4), 347-352.

- Usui, T., Donnelly, C. A., Logar, M., Sinclair, R., Schoonman, J., & Prinz, F. B. (2013). Approaching the limits of dielectric breakdown for SiO<sub>2</sub> films deposited by plasma-enhanced atomic layer deposition. *Acta materialia*, 61(20), 7660-7670.
- Vazirisereshk, M. R., Martini, A., Strubbe, D. A., & Baykara, M. Z. (2019). Solid lubrication with MoS<sub>2</sub>: a review. *Lubricants*, 7(7), 57.
- Voiry, D., Mohite, A., & Chhowalla, M. (2015). Phase engineering of transition metal dichalcogenides. *Chemical Society Reviews*, 44(9), 2702-2712.
- Wang, F., Wang, Z., Wang, Q., Wang, F., Yin, L., Xu, K., ... & He, J. (2015). Synthesis, properties and applications of 2D non-graphene materials. *Nanotechnology*, 26(29), 292001.
- Wang, F., Wang, Z., Jiang, C., Yin, L., Cheng, R., Zhan, X., ... & He, J. (2017). Progress on electronic and optoelectronic devices of 2D layered semiconducting materials. *Small*, 13(35), 1604298.
- Wang, L., Li, Y., Zhao, L., Qi, Z., Gou, J., Zhang, S., & Zhang, J. Z. (2020). Recent advances in ultrathin two-dimensional materials and biomedical applications for reactive oxygen species generation and scavenging. *Nanoscale*, 12(38), 19516-19535.
- Wang, R., Yu, Y., Zhou, S., Li, H., Wong, H., Luo, Z., ... & Zhai, T. (2018). Strategies on phase control in transition metal dichalcogenides. *Advanced Functional Materials*, 28(47), 1802473.
- Wang, Q. H., Kalantar-Zadeh, K., Kis, A., Coleman, J. N., & Strano, M. S. (2012). Electronics and optoelectronics of two-dimensional transition metal dichalcogenides. *Nature nanotechnology*, 7(11), 699-712.
- Withers, F., Pozo-Zamudio, D., Mishchenko, A., Rooney, A. P., Gholinia, A., Watanabe, K., ... & Novoselov, K. S. (2015). Light-emitting diodes by band-structure engineering in van der Waals heterostructures. *Nature materials*, 14(3), 301-306.
- Wu, C. R., Chang, X. R., Wu, C. H., & Lin, S. Y. (2017). The growth mechanism of transition metal dichalcogenides by using sulfurization of pre-deposited transition metals and the 2D crystal hetero-structure establishment. *Scientific Reports*, 7(1), 1-8.

- Wuenschell, J. K., Payton, A. B., Lince, J. R., & Helvajian, H. (2020). Laser processing of thin film sputtered MoS<sub>2</sub>: Thinning, oxidation, and crystallization. *Journal of Applied Physics*, 127(14), 145305.
- Xu, K., Wang, Y., Zhao, Y., & Chai, Y. (2017). Modulation doping of transition metal dichalcogenide/oxide heterostructures. *Journal of Materials Chemistry C*, 5(2), 376-381.
- Yang, H., Kim, S. W., Chhowalla, M., & Lee, Y. H. (2017). Structural and quantum-state phase transitions in van der Waals layered materials. *Nature Physics*, 13(10), 931-937.
- Ye, M., Winslow, D., Zhang, D., Pandey, R., & Yap, Y. K. (2015, March). Recent advancement on the optical properties of two-dimensional molybdenum disulfide (MoS<sub>2</sub>) thin films. In *Photonics* (Vol. 2, No. 1, pp. 288-307). MDPI.
- Yogeesh, M., Chang, H. Y., Li, W., Rahimi, S., Rai, A., Sanne, A., ... & Akinwande, D. (2016, June). Towards wafer scale monolayer MoS<sub>2</sub> based flexible low-power RF electronics for IoT systems. In *2016 74th Annual Device Research Conference (DRC)* (pp. 1-2). IEEE.
- Yoo, H., Heo, K., Ansari, M. H. R., & Cho, S. (2021). Recent Advances in Electrical Doping of 2D Semiconductor Materials: Methods, Analyses, and Applications. *Nanomaterials*, 11(4), 832.
- Yu, H., Cui, X., Xu, X., & Yao, W. (2015). Valley excitons in two-dimensional semiconductors. *National Science Review*, 2(1), 57-70.
- Yue, Y., Jiang, C., Han, Y., Wang, M., Ren, J., & Wu, Y. (2020). Magnetic anisotropies of Mn-, Fe-, and Co-doped monolayer MoS<sub>2</sub>. *Journal of Magnetism and Magnetic Materials*, 496, 165929.
- Zavabeti, A., Jannat, A., Zhong, L., Haidry, A. A., Yao, Z., & Ou, J. Z. (2020). Two-dimensional materials in large-areas: synthesis, properties and applications. *Nano-Micro Letters*, 12(1), 1-34.
- Zhang, C., Chen, Y., Johnson, A., Li, M. Y., Li, L. J., Mende, P. C., ... & Shih, C. K. (2015). Probing critical point energies of transition metal dichalcogenides: surprising indirect gap of single layer WSe<sub>2</sub>. *Nano letters*, 15(10), 6494-6500.
- Zhang, G., Liu, H., Qu, J., & Li, J. (2016). Two-dimensional layered MoS<sub>2</sub>: rational design, properties and electrochemical applications. *Energy & Environmental Science*, 9(4), 1190-1209.

Zhang, Y., Yao, Y., Sendeku, M. G., Yin, L., Zhan, X., Wang, F., ... & He, J. (2019). *Recent progress in CVD growth of 2D transition metal dichalcogenides and related heterostructures. Advanced materials*, 31(41), 1901694.

Zhang, X. (2019). *Metalorganic Chemical Vapor Deposition of Two-Dimensional Layered Chalcogenides. The Pennsylvania State University*.

Zhao, W., Ribeiro, R. M., Toh, M., Carvalho, A., Kloc, C., Castro Neto, A. H., & Eda, G. (2013). *Origin of indirect optical transitions in few-layer MoS<sub>2</sub>, WS<sub>2</sub>, and WSe<sub>2</sub>. Nano letters*, 13(11), 5627-5634.

Zheng, X., Calò, A., Albisetti, E., Liu, X., Alharbi, A. S. M., Arefe, G., ... & Riedo, E. (2019). *Patterning metal contacts on monolayer MoS<sub>2</sub> with vanishing Schottky barriers using thermal nanolithography. Nature Electronics*, 2(1), 17-25.